Effect of Composition and Microstructure on the Oxidation and Corrosion Performance of Ni-Based Superalloys

MALLIKARJUNA HEGGADADEVANAPURA THAMMAIAH

A thesis submitted to

the Faculty of Graduate Studies

in partial fulfillment of the requirements for the degree of

Doctor of Philosophy

Department of Mechanical Engineering

The University of Manitoba

Winnipeg, Manitoba, Canada

September 2019

Acknowledgements

I would like to acknowledge the people who have assisted me throughout my Ph.D. studies at the University of Manitoba and without whom this work would not have been possible.

At first, I would like to express all my earnest acknowledgements to my academic supervisors, Dr. William Caley and Dr. Norman Richards. For all the valuable guidance, timely suggestions, scientific discussions and support during the entire project. It is my honour and privilege to conduct my Ph.D. research with such wise and philosophical friends. Their patience and encouragement during my hard times are gratefully acknowledged.

I would also like to thank my other committee members Dr. Olanrewaju Akanbi Ojo and Dr. Derek Oliver for the several helpful inputs and encouragement at various stages of this research.

Many people from the staff at the University of Manitoba contributed to this work, by technical advice and sharing their experience:

Dr. Khan for his help with transmission electron microscopy (TEM) analysis and Dr. Sidhu for sharing her knowledge on scanning electron microscopy (SEM) in Manitoba Institute for Materials (MIM). Sincere appreciation is extended to Mike Boskwick and Trevor Smith for their technical assistance. I acknowledge the financial support provided by the University of Manitoba and NSERC in the form of graduate fellowship and scholarship.

I would like to acknowledge Dr. James Smialek (NASA-GRC) for facilitating access to the COSP computer program. Also, the authors would like to thank Matthew Harding, Dalhousie University for XRD support.

Finally, I would like to dedicate this work to my parents and brother for their remote everlasting love and understanding throughout my academic Long March. Special thanks go to my beloved wife, Priyadarshini, for giving me endless support and countless strength.

Abstract

The present study reports the findings of the oxidation behaviour of three Ni-based superalloys IN738LC, Rene 80 and N5. The study was performed using a discontinuous thermogravimetric method, which permits mass changes to be measured under cyclic conditions. Oxidation behaviour was described by sample weight and thickness change, spallation, optical microscope, X-ray diffraction and electron microscope analysis. The cyclic oxidation resistance of single crystal alloy N5 was found to be better than that of polycrystalline IN738LC and directionally solidified Rene 80. The projected lifetime of alloys was determined by COSP-Monte Carlo model and the results revealed that the N5 oxidation rate is two orders magnitude lower than that of IN738LC and Rene 80. The chromia scale that formed on both IN738LC and Rene 80 was found to be less protective than the alumina scale that formed on N5. Additionally, the presence of higher amounts of Ti in both the alloys increased the growth rate of the chromia scale followed by scale spallation.

Conversely, the N5 exhibited slow growth rate and less spallation. Although both IN738LC and Rene 80 showed scale spallation, the rate of scale spallation was more severe in Rene 80 after 600 cycles due to the combined effects of high Ti and formation of volatile Mo-rich oxides. The scale spallation in N5 was due to two main reasons, first, void formation because of less adherent Ta_2O_5 and second, the formation of Ta-Hf-oxy carbides, which generate a high shear strain at the matrix oxide and oxy-carbide interface. However, the scale spallation was minimal compared to the other two alloys.

A typical industrial heat-treatment often leads to the formation of multiple size ranges of γ' precipitates during the continuous cooling process. The morphology, distribution and composition of these γ′ precipitates influence the mechanical properties of superalloys. In this part

of the research, IN738LC was cooled at different cooling rates to study the morphology and composition of the γ' precipitates. The results showed that the smaller precipitates obtained by a rapid water quench were spherical, whereas, slower cooled specimens exhibited larger cuboidal shape γ' precipitates. The Al content was higher in γ' precipitates formed from the water quench, whereas the Al was found to decrease in the larger precipitates.

To assess the effect of γ' intermetallic size on the oxidation resistance of IN738LC, coupons (four sizes γ'; monomodal distribution) were subjected to isothermal and cyclic oxidation between 750-950ºC for 150 h/cycles. Parabolic oxidation was found in all cases; based on rate constants, samples with the largest starting γ' were the most oxidation-resistant. Activation energies calculated from precipitate free zone (PFZ) thickness measurements were higher for samples with larger γ' (324 kJ/mole vs 279 kJ/mole). Decreasing the γ' precipitate size increases the oxidation rate of IN738LC. Sub-surface γ' precipitate dissolution was found to be γ' precipitate-size dependent. The interdiffusion coefficient for Al across the PFZ was found to decrease with increasing γ' size.

The influence of γ' size and composition on the corrosion behaviour of IN738LC superalloy was also investigated while maintaining a monomodal microstructure. Experimental results showed a negative influence on the corrosion resistance of IN738LC with increasing rate of cooling, which is attributable to an increase in volume fraction and Al content of the γ' precipitates. Corrosion current density was found to be higher for a specimen with smaller γ' precipitates compared to specimens with larger precipitates. These results serve to further support the concept that oxidation resistance is indeed dependant on γ' intermetallic size whereby smaller precipitates exhibit a higher oxidation rate.

Table of Contents

List of Figures

List of Tables

List of Acronyms

TBC = Thermal Barrier Coatings

TGO = Thermally Grown Oxide

CTE = Coefficient of Thermal Expansion

PSD = Precipitate Size Distribution

PFZ = Precipitate Free Zone

MC = Metal Carbide

FCC = Face Centred Cubic

HRTEM = High-Resolution Transmission Electron Microscopy

DS = Directionally Solidified

TCP = Topologically Close-Packed

PBR = Pilling-Bedworth Ratio

HCP = Hexagonal Close Packed

COSP = Cyclic Oxidation Spallation Program

DISCOM = Deterministic Interfacial Cyclic oxidation Spallation Model

XRF = X-ray Fluorescence

EDM-WC = Electrical Discharge Machining-Wire Cutting

AC = Air-Cooling

FC = Furnace Cooling

RT = Room Temperature

XRD = X-ray Diffractometer

SEM = Scanning Electron Microscopy

EDS = Energy Dispersive X-ray Spectroscopy

SE = Secondary Electron

WD = Working Distance

BSE = Backscattered Electron

TEM = Transmission Electron Microscopy

EBSD = Electron Backscattered Diffraction

IOZ = Internal Oxidation Zone

Chapter 1 Introduction

Aerospace gas turbine engine components are continuously exposed to aggressive environments at elevated temperatures and therefore the choice of the materials used in the engines is of prime interest in the field of materials science to increase stability under these conditions [1]–[3]. These components become oxidized when they are exposed to high-temperature exhaust gasses (temperature range from 650°C to 1100°C) and at a low partial pressure [4], P_{O_2}. Hence, the oxidation and/or corrosion resistance at high-temperature plays an important role in the material selection.

Thermal barrier coatings (TBC) have been used as a barrier to reduce the possible occurrence of bare material oxidation at elevated temperatures above 800°C [5]. Recently, studies on TBC-coated materials have revealed the interfacial delamination of a TBC layer from the substrate, resulting in severe bare material oxidation [6]. Two main reasons for TBC delamination are, first, significant interdiffusion of elements between the bond coat and substrate and second, the presence of residual stresses due to thermally grown oxide (TGO) formation [5]. In such cases, the oxidation resistance of the substrate material is very important. The Ni-based superalloys are one of a family of materials that is suited for this type of condition due to high temperature microstructural stability [7]–[10].

Over the past 60 years, there have been significant developments in Ni-based superalloys to increase their strength and resistance to oxidation [1], [2]. Ni-based superalloys are designed in such a way that they readily oxidize when exposed to an isothermal oxidizing environment to form a protective oxide layer(s) on the surface [3], [11], [12]. The alloy degradation resistance depends upon the sustainability of the oxide layer at high temperatures. The oxide scale should be

thermodynamically stable, dense and continuous, adherent and should exhibit slow growth rate. These alloys depend mainly on alloying elements such as Al, Ta and Ti along with Cr to increase the service life during oxidation by forming thermodynamically stable oxides [3], [13].

This protective oxide scale has a limited period of oxidation resistance and eventually, it will spall off [14]; thermal cyclic conditions will accelerate this scale spallation process. In addition to growth stresses, thermal cycling induces thermal stresses due to oxide scale having a lower coefficient of thermal expansion (CTE) than that of the alloy [3], [15]. Thus, the oxide scale breakdown is a combination of the thermal stresses during thermal cyclic conditions and poor adherence of the oxide scale. Therefore, the alloy should ideally possess an ability to rejuvenate a protective layer even after spallation.

Unfortunately, many of the previous studies that focused on the isothermal and cyclic oxidation of Ni-based superalloys have not completely addressed the effect of alloying elements and microstructure. Hence, there is a need to carry out a detailed study on high-temperature oxidation behaviour of these alloys.

Additionally, a typical industrial heat-treatment for superalloys often leads to the formation of multiple size ranges of γ' precipitates during continuous cooling from solutionizing temperature. The morphology, distribution and composition of these γ′ precipitates influence the mechanical properties of the materials; therefore, a study of the thermodynamic and kinetic factors affecting the evolution of these precipitates is vital for the fundamental understanding of the underlying phase transformations that occur.

Apart from high-temperature mechanical properties, corrosion behaviour near ambient temperature is another important property that can affect the service life and durability of aerospace engine parts during downtime. High aluminum containing alloys are more susceptible to pitting

corrosion due to the intermetallics formed during material processing [16], [17]. The corrosion rate of a high Al containing alloy depends on composition and morphology [18]. It should be noted that most of the reported works on γ′ precipitation have focused on bimodal precipitation during various cooling rates, whereas little work has been done to understand the monomodal precipitation and their corrosion and oxidation properties under continuous cooling rates. One of the major problems during oxidation is the dissolution of the γ' phase in the subsurface zone of the alloy, which eventually decreases the creep strength [19]–[21]. Generally, high oxidation-resistant superalloys may be placed in a phase dissolution category [22]–[24]. The high-temperature oxidation of these alloys involves external Cr_2O_3 scale formation with a branched Al_2O_3 internal subscale [25], [26]. When the Al concentration in the subsurface matrix reaches a minimum, the γ' - Ni_3Al phase acts as an Al reservoir for further growth of Al_2O_3 scales and thus some of the γ' - Ni_3Al intermetallics are solutionized [27].

Previous studies on the formation and size of γ' precipitates at different cooling rates reported that the precipitates that formed during rapid quench were small with high Al concentration relative to the larger precipitates that were formed during slow cooling [28]–[31]. The compositional changes in γ and γ' phases of Ni-based superalloys have also been investigated by some researchers on an atomic scale using an atom probe [32]–[34]. According to Chen et al. [32], the γ' composition is dependent on the precipitate-size in RR1000 alloy and the Al content of secondary γ' precipitates was found to be greater than that of primary γ' precipitates in a bimodal precipitate size distribution (PSD). However, in the same work, it was also reported that the monomodal precipitates formed by rapid quenching did not reveal any compositional difference.

Studies by Edmond et al. [35], [36] on oxidation of Ni-based superalloys revealed that the formation of a precipitate free zone (PFZ) is due to the preferential oxidation of γ' particles at a

low partial pressure of oxygen. The authors also stated that the oxygen diffusion path was always through the γ channels [35], [36], as the dissociation partial pressure of oxygen required to oxidize the matrix (2.5×10^{-25}) is much higher compared to the precipitates (8.1×10^{-36}). In contrast, Ding et al. [37] stated that the oxygen diffusion path is more inclined to the γ'/γ interface compared to that of γ channels. However, the rate of phase transition (γ' to γ) in the subscale region considering the precipitate sizes during oxidation has not specifically been addressed in the literature.

The present study had multiple objectives. The first goal was to study the cyclic oxidation behavior of three Ni-based superalloys, namely, IN738LC, Rene 80 and N5. The alloys differ from each other in both composition and microstructure. The purpose of this study was to critically examine the effects of microstructure and alloying elements such as, Ti, Ta, Al, Cr and Mo on the oxidation resistance and scale spallation behaviour of the three alloys under cyclic conditions. The second goal was to study the monomodal γ′ precipitation and their morphological evolution during different cooling rate conditions. This work was extended to observe the size-dependent composition variation from different cooling rates and their effect on corrosion behaviour while maintaining the monomodal PSD. The third goal was to investigate the influence of precipitate size on the oxidation behaviour and the PFZ thickness of IN738LC.

To understand the effect of precipitate size on oxidation mechanism in detail, the results of the third objective were compared with the standard aged alloy (bi-modal γ' PSD) oxidation test results. This study has a significant value for turbine blades, where the high-temperature mechanical properties of the thin aerofoils depend on the γ' precipitates. Specifically, for the material to excel in high-temperature conditions, it should possess a high volume fraction of γ' precipitates, which are coherently-embedded within the γ matrix [38], [39]. Hence, the

optimisation of the precipitate size and volume fraction is essential and involves careful control of cooling rates.

The unique contribution of the research is the development of a direct relationship between the oxidation resistance and γ' intermetallic size to enable optimization of superalloy resistance by means of microstructure modification.

Chapter 2 Literature Review

2.1. Physical metallurgy of Ni-based superalloys

The most widely used among the families of superalloys are Ni-based. This is a unique class of alloys, which exhibits excellent high-temperature mechanical properties such as resistance to thermal creep deformation, resistance to fatigue, good surface stability/dimensionality as well as corrosion/oxidation resistance [1].

The chemical composition of these alloys establishes the phases present. Hence, the desired structure and properties for specific applications can be achieved through proper selection of chemical composition [9], [40]. The properties that can be controlled include mechanical strength, density, thermal expansion, thermal conductivity and surface stability [9]. The critical properties required in gas turbine engines include low density, low thermal expansion, high thermal conductivity as well as high and reliable tensile, creep, rupture and thermo-mechanical fatigue resistance [9], [41]. Other properties include the ability to withstand aggressive operating atmospheres in terms of oxidation and corrosion resistance.

Over 40-50% of an aircraft engine weight is comprised of Ni-based superalloys [42]. There has been a significant increase in the turbine inlet gas temperature of gas turbines from 700°C to about 1100°C with the development of modern single crystal Ni-based superalloys. This temperature increase has led to an increase in the efficiency of the turbine engines [43].

The phases present in Ni-base superalloys are [9], [12]:

- Gamma matrix (γ): An FCC Ni-based continuous phase with solid solution strengthening alloying elements.

- Gamma Prime (γ'): These are ordered FCC precipitates, which have a structure based on $Ni_3(Al,Ti)$. The γ' precipitates are usually coherent with the γ phase.

- Carbides: Carbides are formed when carbon combines with reactive and refractory elements such as Hf, Ti and Ta to form MC carbides. These later decompose to form secondary carbides such as $M_{23}C_6$ and M_6C, during heat treatment and service.

2.2. Strengthening mechanism of Ni-based superalloys

The two major phases that determine the properties of Ni-based superalloys are the γ matrix and the γ' precipitates.

2.2.1. Gamma phase (γ)

Solid solution strengthening of the γ-matrix can primarily be achieved by additions of elements such as Al, Ta, Co, Fe, Ti, Mo and W [9]. These elements are added to the Ni matrix (γ) without phase instability due to the presence of an incompletely filled third electron shell of Ni atoms [9]. Alloying additions can also be used to control the lattice parameter of the γ matrix, thus providing the lattice mismatch between γ and γ', as well as improving the hot corrosion and oxidation resistance [1], [9].

The solid solution strengthening elements differ from the atomic diameter of Ni by 1-13% and in terms of electron hole number by 1-17%. Thus, the solid solution strengthening effect can be related to local lattice distortion as a result of atomic diameter oversize [9]. Fleischer [44] proposed that strengthening of the γ matrix can result from a local increase in elastic modulus of the lattice due to alloying. This is a result of extra work required to force a dislocation through regions of higher strength than the surrounding matrix. Internal strains generated by inserting

solute atoms in an elastic matrix as well as the difference in elastic modulus can be responsible for solid solution strengthening of the matrix [44].

Alloying element additions can also increase the strength of the γ matrix by lowering the stacking-fault energy, which makes cross-slip more difficult. High temperature, slow-diffusing elements such as W and Mo are rated as the most potent solid solution strengtheners, while Fe, Ti, Co and V are weak solid-solution strengtheners [9]. Aluminium is rated as a potent solid-solution strengthener but also a good precipitation strengthener for Ni_3Al [45], [46].

Surface stability of Ni-based superalloys can also be achieved through alloying additions to the γ-matrix, especially with addition of Cr and Al. Chromium additions in particular improve the hot corrosion of turbine components [43]. Addition of aluminium provides higher temperature oxidation resistance than Cr due to formation of a protective, slow-growing and continuous α-Al_2O_3 scale [47].

2.2.2. Gamma prime phase (γ')

Gamma prime (*γ'*) is a very important intermetallic phase in the form of A_3B, which is a secondary strengthening phase in Ni-based superalloys [9]. In the ordered, cuboidal FCC A_3B intermetallic compounds, the relatively electronegative element Ni occupies the 'A' sites and more electropositive elements such as Al and Ti occupy the 'B' sites [9].

A high Ni content in the matrix favours the formation of γ' precipitates, which requires a small change in size as a result of a Ni atom being incompressible due to its 3d electron state [9]. Homogeneous nucleation of precipitates with low interfacial energy and excellent long-term stability is possible due to the compatibility of the γ' FCC crystal structure and lattice constant with the γ matrix [48]. The ordering temperature of Ni_3Al (γ') depends strongly upon the degree of

stoichiometry and concentrations of impurities, and is approximately equivalent to its melting temperature of about 1375°C [12]. The high temperature mechanical properties of Ni-based superalloys are limited to about 1100°C-1150°C due to the melting temperature of Ni matrix and γ' phases [9].

Alloying additions can be used to strengthen the γ' phase, prevent excessive coarsening and alter its lattice parameters [43], [49], [50]. Slow diffusing alloying elements, such as, Co, Nb or Mo retard the coarsening rate of the γ' phase. Thus, a fine γ' phase structure is maintained, even after prolonged exposure at higher temperatures. The strength of the alloy and its creep properties can also be altered by changing the lattice parameters of the precipitates, which affects the lattice strains induced by precipitation [9].

2.3. The relationship between γ and γ'

The creep properties and strength of the alloy at high temperatures come from the lower lattice misfit between the γ and γ' phases, while the strength at a lower temperature is due to the high lattice misfit. Further, the γ/γ' interface remains coherent and the interfacial energy remains low, provided that the lattice misfit between the γ and γ' phases is not too large [12].

The high-temperature properties of the superalloys are found to depend on the coherent interface between the γ and γ' [48]. This is due to the magnitude and sign of the lattice misfit between γ and γ', which results in the formation of high coherency stresses [51]–[53]. Also, a positive lattice misfit indicates that the lattice parameter of the γ' ($a_{\gamma'}$) is larger than that of the matrix (a_{γ}), and vice versa [48].

The coherency between the γ and γ' phases is determined by a number of facts such as atomic arrangement, lattice parameters and orientation of the two phases [52]. In order to form

coherent interfaces, the two phases must have similar crystal structures and lattice parameters. However, coarsening of the γ' precipitates leads to both loss of coherency and increases lattice misfit [1]. Generally, the finer precipitates are found to exhibit a uniformly dispersed network of coherent interfaces to reduce the interfacial energies [9], [54]. In addition, smaller particles can remain strained-coherent, whereas larger particles, even with the same structure, become semi-coherent.

2.4. Precipitation mechanism

The γ' precipitate formation is a mechanism which involves solute diffusion; it falls under a diffusional transformation category [55]. The precipitation generally follows either a classical nucleation event followed by a growth mechanism or by spinodal decomposition. First, in the nucleation and growth case, the formation of a nucleus of different phases with equilibrium composition reduces the total free energy of the system. The change in free energy of a system, ΔG due to the formation of a spherical nucleus is given by:

$$\Delta G = -\left(\frac{4}{3}\right) \cdot \pi \cdot R^3 \cdot \Delta G_v + 4 \cdot \pi \cdot R^2 \cdot \gamma \qquad (1)$$

where R is the radius of the nucleus, ΔG_v is the change in free energy per unit volume and γ is the interfacial energy between the parent phase and the nucleus. If the parent phase is more stable than the nucleus ($\Delta G_v > 0$), then both the volume free energy and surface energy are positive, and therefore, the total free energy of the system continues to increase with increase in the large compositional fluctuation. On the other hand, if the parent phase is metastable relative to the nucleus ($\Delta G_v < 0$) and the volume free energy is negative, small concentration fluctuations will

increase the total free energy due to the contribution of the new surface created during nucleus formation [56]. A schematic illustration of the concentration fluctuation size dependence of free energy using classical nucleation theory is shown in Figure 2-1 [56], [57].

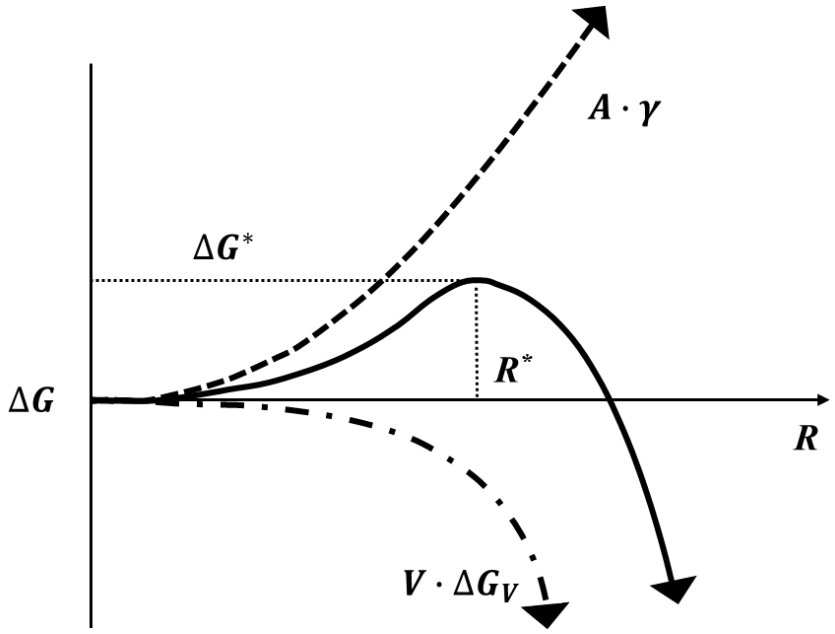

Figure 2-1. Schematic illustration of concentration fluctuation size dependence of free energy (Reproduced with permission from Prentice-Hall, Inc.) [56], [57].

For the second phase to precipitate inside the parent phase, the concentration fluctuation size should be greater than the critical radius (r^*) of the fluctuation (maximum excess free energy). If fluctuation size surpasses the r^*, ΔG of the system will decrease. On the other hand, if the fluctuation size is less than the r^*, their free energy decreases resulting in dissolution of embryo in the parent phase. The critical radius, r^* and the activation barrier, ΔG^* for the nucleation process are given by:

$$r^* = \frac{2 \cdot \gamma}{(\Delta g_c + \Delta g_s)} \tag{2}$$

and

$$\Delta G^* = \frac{16 \cdot \pi \cdot \gamma^3}{3(\Delta g_c + \Delta g_s)^2} \quad (3)$$

respectively, where Δg_c and Δg_s are the chemical energy and strain energy respectively. However, for homogeneous nucleation to occur, there has to be larger undercooling, i.e., below the equilibrium melting temperature (T_m). For undercooling ΔT, the volume free energy (ΔG_v) is given by [57]:

$$\Delta G_v = \frac{\Delta H_m \Delta T}{T_m} \quad (4)$$

where ΔH_m is the latent heat of melting per unit volume and $\Delta T = (T_m - T)$ is the undercooling temperature.

Therefore:

$$\Delta G^* = \left(\frac{16 \cdot \pi \cdot \gamma^3}{3(\Delta H_m)^2}\right) \cdot \left(\frac{1}{(\Delta T)^2}\right) \quad (5)$$

Equation (5) suggests that an increase in undercooling decreases the size of the precipitate (R^*) and the total free energy of the system ΔG^*.

The concentration fluctuation of radius r^* can be explained by the Arrhenius equation. Therefore, the rate of homogeneous nucleation is given by:

$$N_{Hom} = f_0 \cdot C_0 \cdot \exp\left(-{\Delta G^*}/{k \cdot T}\right) \cdot \exp\left(-{\Delta G_m}/{k \cdot T}\right) \quad (6)$$

Where f_0 is a function that depends on the vibration frequency of an atom, C_0 is the number of atoms in nuclei per unit volume, k is the Boltzmann constant, T is the absolute temperature and ΔG_m is the activation energy required for the migration of atoms across an interface. When the nucleus size is small, it contributes minimal strain energy during the nucleation process; therefore, precipitates will take a spherical form to reduce the interfacial energy. However, increasing strain energy will transform the precipitate morphology from spherical to other shapes.

The other form of precipitation mechanism is spinodal decomposition, where there is no thermodynamic barrier for nucleation and the nucleation occurs solely by diffusion [56]. The spinodal decomposition process can occur for an alloy composition where the free energy curve has a negative curvature [57], i.e.,

$$\frac{d^2G}{dx^2} < 0 \quad (7)$$

The locus of the spinodal (S_1 and S_2) where the ${d^2G}/{dx^2} = 0$ is called the spinodal point [56], [57].

The spinodal phase separation or nucleation is a low-temperature process [57]. According to Cahn [58], there is constant concentration fluctuation throughout the matrix inside the two-phase field of the phase diagram, which increases in amplitude over a time resulting in phase decomposition. As explained before, the classical nucleation theory suggests that for a nucleus to grow greater than the critical size nuclei have to overcome some activation energy barrier and then

it will have a sharp interface between the nucleus and the parent phase. However, Cahn's theory assumes no critical size and/or a sharp interface.

2.5. Effect of cooling rate on γ' precipitation

Since the diffusivity is temperature dependent, the segregation of alloying elements highly depends on the cooling rate and hence knowledge of the dependence of composition on cooling rate for γ and γ′ is essential. The γ' precipitate size, distribution and their morphology depend highly on both heat treatment and processing conditions. Since the high-temperature mechanical properties of superalloys depend on the above-mentioned microstructures and a small variation in these microstructures affects the mechanical properties, it is essential to study the effect of cooling rate on the evolution of microstructure.

A change in microstructure as a result of different cooling rates has been studied a number of times [31], [59]–[61]. It has been found that materials quenched from the solutionizing temperature (i.e., from single γ phase) using high cooling rates will produce a mono-modal γ' precipitate size distribution [62]. Since the growth of the precipitate is limited at the faster cooling rate, these precipitates retain their spherical morphology. In contrast, the slow-cooled materials exhibit a wide range of γ' precipitate size and morphology.

Although there has been extensive research done on the γ' precipitate size distribution using high-resolution transmission electron microscopy (HRTEM) [63]–[67], the multiple nucleation events and their mechanism of formation still needs to be addressed. There has been significant work done on the segregation of alloying elements between the ordered γ' precipitate and the disordered γ phase resulting in multiple precipitate size distribution.

Some research results also showed an increase in volume fraction of larger γ′ precipitates with a decrease in cooling rate [68]. Research has also revealed that the relationship between the precipitate size and cooling rate follows a power law, although this is only valid for larger γ′ precipitates [69]. Tian [70] revealed that the size of a γ′ precipitate is inversely proportional to the cooling rate and an increase in cooling rate will change the morphology from a flower-like structure to spherical. There is a strong relationship between the cooling rate and the mechanical properties since cooling rate changes the precipitate size distribution. Some experimental results have also shown that an increase in cooling rate increases the hardness and tensile properties [71].

The dependence of microstructure and composition of γ and γ′ phases on cooling rate using directionally solidified CM247DS Ni-based superalloy was studied by Babu et al. [61]. The results revealed that the spherical morphology of γ′ precipitates was found in water-quenched samples, whereas slowly cooled specimens exhibited a bimodal precipitate distribution with larger cuboidal/irregular to smaller spherical precipitates. It was also found that an increase in cooling rate decreases the size of the larger γ′ precipitates and increases the number density of the γ′ precipitates. It was observed that there was no compositional change in the larger precipitates; however, a higher Al concentration was noted for smaller precipitates. Chen [32] has also reported that cooling rate affects the γ' precipitate size and composition in Ni-based superalloy RR1100. The study revealed that the fastest cooling rate with the fine-scale tertiary γ' precipitates had non-equilibrium compositions, whereas, the secondary γ' precipitates were found to have local equilibrium compositions [32].

Similar results were also reported by Michell and Preuss [72]. They studied the effect of cooling rate on the lattice mismatch between the γ and γ' phase in UDIMET720 alloy and concluded that the compositional variation in the γ' is the main reason for the lattice mismatch.

The γ' precipitates were extracted from the matrix and examined under synchrotron x-ray diffraction. It was found that the γ' produced from the fastest cooling rate had higher Al content than tantalum (Ta), whereas the larger γ' from slow cooling rate had higher Ta. The phase transformation from γ to γ' during different cooling rates for Ni-based superalloys, AM1 and CMSX-2 was studied by Grosdidier [73]; he showed that an increase in cooling rate decreases the phase transition temperature and the morphology of the γ' changed from large cuboidal/irregular shape to spherical.

All these studies suggest that the increase in cooling rate will change the γ' precipitate morphology from larger cuboidal to spherical and the γ' precipitate size distribution will change from multimodal to monomodal. In addition, varying the cooling rate will change the precipitation mechanism. Therefore, understanding the influence of cooling rate on the precipitation mechanism is of prime importance for prediction of high-temperature mechanical properties.

2.6. Multimodal precipitation during continuous cooling

The multi-modal γ' precipitation mechanism during continuous slow cooling is a complex process since it involves multiple nucleation bursts at various temperatures. The composition-dependent γ' precipitate size variation in a multimodal system has been studied by Srinivasan [74] using atom probe tomography. The study also reported that the interface width between γ - γ' varies with respect to the precipitate size. The larger cuboidal/irregular γ' precipitates (primary) were reported to consist of sharp interfaces, whereas, the spherical or secondary precipitates consisted of diffused interfaces. Although several studies have been done on the multimodal precipitation mechanism, no clear explanation has been given for multiple nucleation events through experiments [75]–[78]

In recent years, phase field modelling has gaining significant attention over atom probe tomography to simulate microstructural evolution i.e., γ' precipitation in Ni-based superalloys. Several compositional results have been published by Seidman [79] stating that the interface between γ and γ' is diffusive. Since the phase field models consist of diffusion interfaces built into them, they can predict microstructures close to those found by experiment. Phase field modelling has certain limitations. For example, it can be used under isothermal conditions by considering only the long-range order parameter. Since the thermodynamic force for nucleation varies constantly during continuous cooling tests, this method is not feasible. Some researchers incorporated this limitation and developed a new phase field model to predict precipitate size distribution during continuous cooling [80]. However, the new model failed to determine the inter-precipitate distance.

Wen [31] has explained the bimodal precipitate size distribution using phase field modelling under continuous cooling using three different cooling rate conditions. Wen [31] also reported that the diffusion rate can be controlled through the cooling rate. A slow cooling rate will produce larger precipitates due to the small diffusion coefficient; thus, microstructural evolution during this condition is similar to that of the isothermal condition. If the cooling rate is very high, the diffusion distance for alloying elements will decrease and hence the nucleation will terminate. However, an intermediate cooling rate produces bimodal precipitation due to the impingement with the first nucleation at a higher temperature and thus supersaturation between the adjacent precipitates will increase on further cooling. This increases the driving forces for the second nucleation to occur.

Similar results have also been reported by Furrer [81] on U720LI alloy during different cooling rate experiments. A multimodal γ' precipitate size distribution was reported to depend on

temperature and the variation in the composition of the matrix. The initial nucleation kinetics during supersolvus heat treatment is controlled by the supersaturated matrix phase. Subsequent nucleation, i.e., the formation of secondary precipitates is controlled by many factors, such as initial nucleation, diffusion kinetics of the initial nucleation, cooling rate and matrix composition.

2.7. Coarsening of γ' precipitation

Many researchers have studied the coarsening of γ′ precipitates since the mechanical properties depend on γ' precipitate size and their morphology. The morphology of these precipitates will affect the lattice parameter and therefore this change is very important. For example, a change in morphology from spherical to cuboidal with increasing ageing time has been studied by Ricks [48]. The author revealed that a γ′ precipitate particle nucleates as a sphere at high temperature to minimize interfacial energy since the contribution due to strain energy resulting from lattice misfit is low [48]. As a particle grows, the strain energy increases significantly, thus lowering the interfacial energy by changing the shape from spherical to cuboidal.

After a critical nucleus size has been reached, the precipitate growth is termed Oswald ripening [82]. According to this, the driving force for precipitate growth is the interfacial energy between precipitate and matrix. Lifshitz and Slyozov [83] and Wagner [84] (LSW model) proposed a diffusion-controlled precipitate growth process. This model assumed that the diffusion field of adjacent precipitates does not overlap. Also, the model neglected the strain effect. Hence, discrepancies exist between experiment and model. Ardell [34] later modified the LSW model by including the misfit between the matrix and precipitate and found that the matrix reaches equilibrium concentration with an increase in coarsening rate of precipitates.

2.8. Effect of alloying elements

In order to produce the desired structure and properties that will promote higher temperature mechanical strength and excellent environmental resistance, the chemical composition must be carefully controlled. Increasing the amount of gamma prime (γ')-forming elements, such as Al and Ti, as well as adding refractory elements can be used to modify the chemical composition [85], [86]. In single crystal alloys, there is also a significant replacement of Ti with Ta which strengthens the γ' and also raises the solidus temperature [87].

The microstructure of superalloys with different phases is influenced by the number of alloying elements present in the matrix [13]. The behaviour of alloying elements depends on their position in the periodic table. The atomic radii of chromium, cobalt, ruthenium, rhenium, tungsten, iron and molybdenum are close to the atomic radius of nickel and therefore take part in the stabilization of the γ phase. The γ' phase is stabilized by the larger atomic radii elements such as aluminum, niobium, tantalum and titanium. The other class of alloying elements like boron, carbon and zirconium acts as grain boundary strengtheners in the γ phase [1]. Aluminium and chromium are also necessary to improve the surface stability through the formation of Cr_2O_3 and Al_2O_3 respectively.

The Cr content in most Ni-based superalloys has been reduced from 20 wt. % over the years to about 5 wt. %. This is to achieve high solubility of Al and Ti [86]. At temperatures below 950°C, Cr has been found to be effective in increasing corrosion resistance [86], [88]. A Cr_2O_3 scale also provides good oxidation and hot corrosion resistance before the formation of volatile CrO_3 at temperatures above 950°C [89], [90]. Excessive amounts of Cr and heavy metals, such as Mo and W, promote the formation of topologically close-packed (TCP) phases. These phases

usually occur with highly embrittling platelet morphology [87]. Hence, overall amounts of Cr, Mo, and W must be well controlled.

The presence of Al in the first generation Ni-based superalloys strengthens the matrix to a certain extent by promoting the formation of γ' and supports the formation of stable Al_2O_3 scale. The formation of an alumina scale provides excellent oxidation resistance at elevated temperatures above 950°C where chromia formation does not provide resistance to oxidation [9]. Addition of Zr, Hf and Cr helps to improve the adhesion of Al_2O_3 scale to the alloy surface and thus reduce spallation. Other alloying elements in the first generation Ni-based superalloys included Ti, Co, V, Nb, Mo, W, and Ta.

Rhenium additions of about 3 at. % to the second generation Ni-based superalloys were found to increase creep strength at higher temperatures [91]. However, higher Re contents of about 6 at. % in the third generation Ni-based superalloys resulted in precipitation of topologically close-packed (TCP) phases after long-term high-temperature exposure [92]–[94]. This has a disastrous effect on the alloy high-temperature creep strength. Addition of Ru to a third generation Ni-base superalloy with high Re contents was found to reduce the TCP precipitation rate substantially. Also, increases the solubility limits of solid-solution strengthening elements in the matrix, particularly for Re and W. Table 2-1 lists the effects of some major alloying elements in Ni-base superalloys [95].

Table 2-1. Effects of major alloying elements in Ni-based superalloys [95].

Elements	Effects
Chromium	Improves oxidation and corrosion resistance, promotes TCP phases, carbide former ($M_{23}C_6$ and M_7C_3)
Aluminium	Increases the γ' volume fraction, improves oxidation resistance
Titanium	Promotes the formation of γ', forms TiC
Molybdenum	Solid solution strengthener, carbide former (M_6C and MC), increases alloy density, promotes TCP phases
Cobalt	May raise or lower solvus, raises the γ' solvus temperature
Tantalum	Strong solid solution strengthener, carbide (MC) and γ' former
Niobium	Strong γ and γ' strengthener, NbC former, promotes δ phases
Tungsten	Strong solid solution strengthener, promotes TCP phases
Ruthenium	Solid solution strengthener.
Rhenium	Retards coarsening; increases misfit between the γ and γ'
Boron; Zirconium	Improves creep strength and ductility, inhibits carbide coarsening, boron when present in large amount forms borides
Carbon	Promotes the formation of various carbides
Silicon	Promotes the formation of protective silica scale
Rare earth elements, Zr & Hf	Improves adhesion of protective scales

2.9. Development of Ni-base superalloys

Over the past 50 years, there have been dramatic improvements in casting techniques. These developments allowed industries to produce components for the Ni-based superalloys with the addition of lower amounts of oxide-forming elements such as Al and Cr. Development of advanced processing technologies such as vacuum casting, directional solidification and development of single crystal alloys as well as improved chemical composition through alloying have resulted in gradual increase in service temperatures and improved mechanical properties of Ni-based superalloys [1]. There were considerable improvements in grain boundary creep strength of directionally solidified alloys due to the elimination of transverse grain boundaries [96]. Single crystal alloys, which are a modification of directionally solidified alloys, possess improved creep resistance and higher melting temperature [97]. This is as a result of the total elimination of grain boundaries and thus, a premature failure that would have occurred when grain boundaries are present in the alloy is prevented. Most modern high-temperature components, such as high-pressure turbine blades, are produced as single crystal alloys [97]. Therefore, in developing new materials for higher temperature applications, proper consideration must be given to the processing techniques.

2.10. Oxidation of metals

Oxidation is an electrochemical process where oxygen ions and metal ions interact to produce a new substance called oxides. The oxides formed on the surface of metals may be a single layer or multiple layers consisting of different compositions; this depends on the oxidizing atmosphere and

temperature [98]. The oxidation of metals depends on two major factors, namely thermodynamics and kinetics. Thermodynamics shows the possibility of an oxidation reaction occurring depending on Gibbs free energy. On the other hand, kinetics reveals how fast the reaction will occur when the oxidation is possible. Since kinetics will determine the extent of metal consumption, it is often considered to be more important than thermodynamics [3]. Oxidation of pure metals provides a fundamental knowledge of a more complicated process associated with the oxidation of alloys.

2.10.1. Thermodynamics of oxidation

During oxidation, initially, oxygen adsorbs on the surface of a metallic substrate and as the reaction proceeds, either a film of oxide will form on the surface or separate oxide islands nucleate on the surface of the substrate. Depending on growth kinetics of the oxide scale, the scale may or may not protect the metal beneath[99]. Oxidation seems to be a simple electrochemical process, but the reaction path and the behaviour involve a large number of phenomena, which are influenced by many different factors [100], [101]

The formation of an oxide is described by the reaction [3],

$$xM(s) + \left(\frac{y}{2}\right) O_2(g) \rightarrow M_x O_y \quad (8)$$

Where M is the metal and subscripts x and y are the stoichiometric constants.

Most metals tend to oxidize to some extent when they are exposed to an oxidizing environment. Whether this process is likely to occur, is defined by the change in Gibbs free energy connected with the formation of the oxide from the reactants (ΔG) [3].

$$\Delta G = \Delta G^0 + R \cdot T \cdot \ln\left[\frac{a_{M_xO_y}}{a_{M_x} \cdot P_{O_2}{}^{y/2}}\right] \quad (9)$$

where a is the chemical activity of a component, P_{O_2} is the oxygen partial pressure, T the absolute temperature and R the universal gas constant.

If $K = \frac{a_{M_xO_y}}{a_{M_x} \cdot PO_2{}^{y/2}}$, at equilibrium when ΔG = 0, then the above equation becomes:

$$\Delta G^0 = -R \cdot T \cdot \ln[K] \quad (10)$$

Where K is the equilibrium constant. Taking logarithms, Equation 10 becomes:

$$K = e^{\left[\frac{-\Delta G^0}{R \cdot T}\right]} \quad (11)$$

The minimum partial pressure of oxygen required to form a metal oxide can be obtained from Equation 11:

$$P_{O_2}{}^{y/2} = e^{\left[\frac{-\Delta G^0}{R \cdot T}\right]} \cdot \frac{a_{M_xO_y}}{a_{M_x}} \quad (12)$$

The equilibrium dissociation pressure of M_xO_y is $P_{O_2}{}^{y/2}$. The ambient oxygen must exceed the equilibrium dissociation pressure, $P_{O_2}{}^{y/2}$ before a metal oxide will form.

However, once an oxide layer M_xO_y has developed on the metal surface, it acts as a barrier between the metal/alloy and oxygen. For the reaction to proceed further, it was reported that one or both reactants must penetrate the oxide layer, i.e. either the metal ions must migrate through the oxide scale to react at the oxide-gas interface or oxygen must be transported to the oxide scale-

metal/alloy interface and react there [3]. The reaction mechanism depends on the slowest step of the process. This may include one of several stages such as transportation of metal or oxygen ions through the oxide layer, mass or electron transport across one of the interfaces or electron-transfer processes associated with the chemisorption step [102]. Hence, the kinetics of the system, rather than the thermodynamics of the reaction, controls the oxidation rate [103].

2.11. Oxidation kinetics

2.11.1. Kinetics law

Generally, kinetics are used to estimate the rate of an oxidation process, although equilibrium thermodynamics may explain which oxidation process is likely to occur. This is not sufficient for complete understanding of an oxidation process. There are many factors which determine oxidation kinetics such as temperature, oxygen partial pressure, metal pre-treatment and oxidation duration. The oxidation rate is highly dependent on the method of heating, be it isothermal oxidation or cyclic oxidation. The isothermal oxidation method is used to characterize the oxide scale growth as a function of exposure duration at constant temperature, whereas cyclic-oxidation involves rapid heating and cooling.

The kinetics of oxidation of metal and alloys generally follows several reaction rates. Most reactions follow a parabolic rate, some reactions follow a linear rate and some other reaction kinetics may include logarithmic rates [3], [104], [105].

2.11.1.1. Linear oxidation rate

It has been reported that if the metal surface is not protected by a barrier of oxide, the oxidation rate usually remains constant with time, and one of the steps in the oxidation reaction is rate controlling rather than a migration process being rate controlling [3]. This situation is to be expected if the Pilling-Bedworth ratio (PBR) is less than 1, if the oxide is volatile, if the scale spalls off or cracks due to internal stresses or if a porous, unprotective oxide forms on the surface metals. During linear oxidation, the oxidation of a metal proceeds at a constant rate and follows the linear rate law as follows [3], [104], [106]:

$$x = k_1 . t + C \tag{13}$$

Where x is the mass or thickness formed, t is the time of oxidation and k_1 is the linear rate constant. The oxidation never slows down; after long times at elevated temperatures, the metal will be completely destroyed.

2.11.1.2. Logarithmic oxidation rate

At low temperatures when only a thin oxide film of oxide has formed, the oxidation is usually observed to follow logarithmic kinetics. The migration process across the film is rate controlling, with the driving force being electric fields across the film. The logarithmic equation is [107]–[109].

$$x = k_e \log(at + 1) \tag{14}$$

Where k_e and a are constants.

2.11.1.3. Parabolic oxidation rate

When an oxide scale forms on the metal surface, the oxidation reaction is controlled by the diffusion of ions through the oxide scale, which is in turn controlled by the chemical potential gradient as a driving force. As the thickness of the oxide scale increases, the rate of oxidation decreases with increasing time due to the increasing diffusion distance for ions. The oxidation rate is, thus, directly proportional to the thickness of the oxide scale [104], [105]

$$X^2 = k_p \cdot t \tag{15}$$

Where, X is the oxide scale thickness (μm^2), t is the exposure time (s), and k_p is the parabolic rate constant ($\mu m^2/s$); when $t = 0$, $X=0$.

Another form of the parabolic rate equation is given by the weight gain, W (g/cm^2) [3], [106]:

$$\Delta W^2 = k_p \, . \, t + C \tag{16}$$

The parabolic oxidation rate increases exponentially with temperature, following the Arrhenius equation [110]:

$$k_p = k_o \, . \exp\left(\frac{-Q}{RT}\right) \tag{17}$$

Where k_o is a constant that is a function of the oxide composition and the gas pressure. For cation-deficient or cation-excess oxides where the diffusion of cations is much greater than the diffusion of anions, the activation energy for oxide growth is the same as the activation energy for diffusion of cations in the oxide. For anion-deficient oxides, where the diffusion of anions is much greater than the diffusion of cations, the activation energy for oxide growth is the same as that for anionic diffusion, verifying that ionic diffusion is the rate controlling process [107].

2.12. Wagner's theory of oxidation

When most materials are exposed to an elevated temperature under an oxidizing environment, they will first exhibit a thin single layer of oxide scale on the surface. However, subsequent oxide growth requires migration of either metal ions (cations) or oxygen ions (anions) through the oxide scale [111]. The diffusion mechanism and the defects present in the oxide scale control the migration of cations and anions through oxide scale. Generally, the transport of ionic species through an oxide scale follows solid-state diffusion mechanism and the kinetics are often parabolic in nature. The diffusion distance will increase if the oxide scale is thicker compared to that of a thinner scale. Beyond some thickness of the layer, diffusion will control both overall rate of reaction and the rate of oxide scale thickening. Wagner's model makes the following assumptions [107], [112], [113]:

- The oxide scale is compact and perfectly adherent.
- Migration of ionic species or electrons through the oxide scale is the rate controlling process.
- There is a thermodynamic equilibrium between both metal/scale and scale/gas interfaces.
- Solubility of oxygen in the metal may be neglected.

Since both metal/scale and scale/gas interfaces are in equilibrium, concentration gradient of both metal and oxygen ions occurs across the oxide resulting in the transportation of both metal and oxygen ions through the oxide scale in opposite directions. The migration of these ions will create an electric field as the ions are charged. The net result of the transportation of cations, anions and electrons will form electroneutrality in the oxide scale [105], [112]. Figure 2-2 illustrates that

the transfer rates of cations, anions and electron holes are in balance so that no net charge transfer occurs across an oxide scale [3], [107], [114].

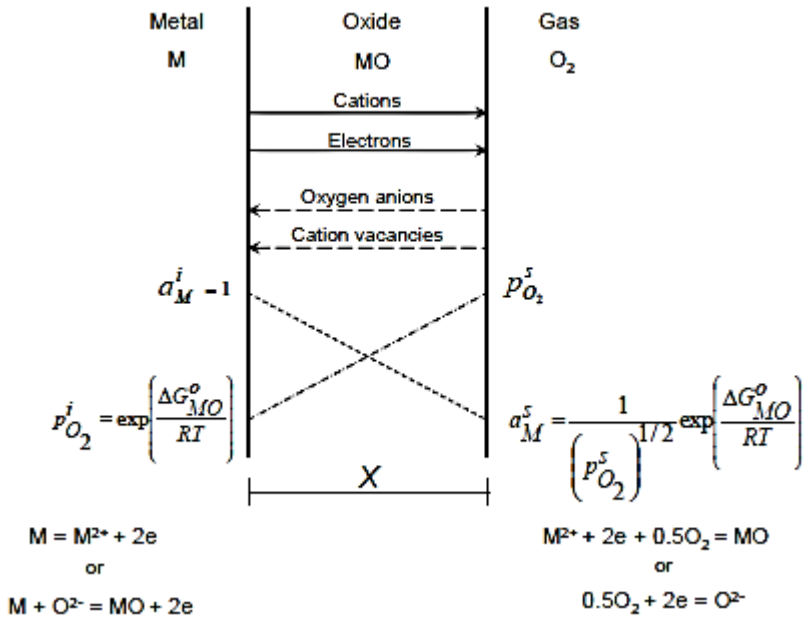

Figure 2-2. Schematic diagram of oxide scale formation according to Wagner's oxidation model (Reproduced with permission from Cambridge University Press) [3], [107], [114].

There are only a few oxides which strictly follow Wagner's oxidation model [113]. In the present work, these are NiO and CoO. The reasons for deviation from Wagner's model are the basic assumptions. First, the model assumes that the oxide scale is compact and adherent, which is not followed by many oxides. Second, an oxide is more or less stoichiometric, which is again rarely observed. Third, a degree of solid solubility between the oxides may exist. Further, the migration of ionic species in many oxides is partially accomplished by grain boundary diffusion.

2.13. Defects and oxide scales

According to Wagner's theory of oxidation [111], the oxides that form on the surface of metals often contain impurity cations that are soluble in the oxide. These impurities alter the defect concentration of the oxide scale, subsequently affecting the oxide growth rate. Whether oxide growth increases or decreases depends on the relative valences of the cations and the type of oxide.

2.13.1. Doping of oxides

Most oxides are either *p*- or *n*-type semiconducting depending on whether the oxide exhibits excess vacancies or is deficient in vacancies [114]. The oxidation rate in a *p*-type semiconducting oxide is controlled by cation diffusion through cation vacancies [114]. If the number of cation vacancies decreases, the oxidation resistance increases. For example, in a Ni system, the cation vacancies are present due to a small fraction of Ni ions that exhibit higher valency than the normal valence, contributing more than normal share of electrons to the oxygen ions and thus allowing a small fraction of cations to be absent from the structure. Further, if a few cations with a higher valence are substituted for the regular cations in an oxide, the vacancy concentration increases. For example, if a small amount of Al is added to a Ni system and then the system is oxidized to form NiO with a few substitutional Al^{3+} ions, the oxidation resistance decreases compared to pure NiO due to an increase in vacancy concentration [114], [115].

The *n*-type semiconducting oxides behave opposite to the *p*-type oxides [113], [114]. Here the diffusion mechanism is anionic through anion vacancies and these vacancies exist because some cation vacancies have fewer than normal vacancies and therefore contribute fewer electrons to oxygen than required by stoichiometry. The addition of low-valent cations replaces the regular

high-valent cations resulting in an increased oxidation rate. On the other hand, the substation of higher-valent cations to the normal-valent cations reduces the oxidation rate by reducing the anion vacancy concentration.

2.13.2. Point defects

A point defect in a crystal is an entity that causes an interruption in the lattice periodicity. This can occur due to removal of an atom from its regular site in the crystal structure [116]. Various kinds of point defects can be formed; these may be intrinsic or extrinsic, substitutional or interstitial [117]. For instance, Schottky and Frenkel defects are referred to as intrinsic defects since their numbers are controlled by intrinsic properties of the structure, related to the size of the interatomic forces, whereas, the presence of impurities or variation in oxidation rate are considered as extrinsic defects, which can vary from one crystal to another [116]. The Schottky defects occur where a vacant anionic site in a structure is balanced by a vacant cationic site to main maintain electrical neutrality. On the other hand, a Frenkel defect is when an atom moves from its site, leaving a vacancy and is placed in an alternative interstitial site, which is normally unoccupied. Both Schottky and Frenkel defects leaves the overall charge balance and the stoichiometry unaffected [118].

2.13.3. Line and planar defects

The mechanism of diffusion along line and planar defects is generally more rapid compared to that of point or lattice defects. The diffusion along line and surface defects requires lower activation energy than lattice diffusion, typically 50% to 70% of the activation energy of lattice diffusion [119]. Dislocations are considered to be the only line defects in crystalline materials; grain

boundaries, internal and external surfaces can be considered as planar defects. Both line and planar defects are termed as high diffusivity paths. This type of diffusion is also called short-circuit diffusion [120], [121]

Since the activation energy for grain boundary diffusion is always less than the activation energy for lattice diffusion (from 20 to 30% smaller), grain boundary diffusion is greater than lattice diffusion [109]. Typically, grain boundary diffusion in metals is four to six orders of magnitude faster than lattice diffusion [122]. The difference between grain boundary and lattice diffusion may be due to two major reasons. First, if the diffusion length is the same in both grain (lattice) and grain boundary, there is not much difference in the diffusion rates. Second, if the grains are relatively bigger than the grain boundary, this means that the diffusion length in grains is much longer than grain boundary.

However, the temperature will change the diffusion mechanism in the material. At lower temperature, the diffusion process is controlled by grain boundary diffusion and at high temperature both lattice and grain boundary diffusion are equal [123], [124]. The transformation temperature will depend on the relative area of the grain boundary. The nature of a grain boundary depends on the orientation of two adjacent grains. In these cases, only the effective overall diffusion coefficient is measured, not lattice and grain boundary diffusion separately [124].

2.14. Mechanical properties of oxides

2.14.1. Stresses in an oxide scale

Most commercial alloys rely on the formation and maintenance of an oxide layer to sustain mechanical integrity at high temperatures. This oxide acts as a barrier between the substrate and the oxidizing environment, which increases the oxidation resistance at elevated temperature [125], [126]. However, these protective oxide layers are susceptible to failure by the presence of

mechanical stresses at the scale/alloy interface [127]. There are various sources of stresses in an oxide scale such as stresses resulting from oxide growth, thermally induced stresses resulting from temperature change and finally, external stresses due to deformation at a scale/alloy interface [3], [128]. In order to ensure maintenance of the protective capacity of the oxide scale it is necessary to understand the proposed mechanisms of development of both the growth and thermal stresses.

2.14.1.1. Growth stress

Pilling and Bedworth first proposed the mechanisms of development of growth stresses in an oxide scale [3]. This model includes the specific volume differences between the oxide scale and the substrate. The model considers only the transition from the substrate to the oxide phase when only oxygen ions are diffusing. The magnitude and the sign of the stress in the oxide scale depend on the Pilling-Bedworth Ratio (PBR), which is defined as the ratio of volume/metal ion in the oxide to the volume per metal ion in metal [3]. The PBR for some oxides and metals are given in Table 2-2 [88], [127], [129], [130].

Table 2-2. Some typical Pilling-Bedworth ratio values [88], [127], [129], [130].

Oxide/Metal	NiO/Ni	FeO/Fe	CoO/Co	Cr_2O_3/Cr	Al_2O_3/Al	TiO_2/Ti	SiO_2/Si
PBR	1.65	1.68	1.86	2.07	1.28	1.73	2.15

When the PBR is greater than unity, the oxide is expected to be in compression and the oxide will be in tension when the PBR is less than unity [3], [131]. The PBR of oxides of most metals and alloys is greater than unity as shown in Table 1 and thus they form in compression. However, the growth stresses can be neglected if the oxide scale grows by outward diffusion of metal ions

because the oxide grows freely on the scale surface. The disadvantage of using PBR is that it predicts unrealistically large stress and strains [3]. Also, there is no relation between the PBR values and the magnitude of stress developed in the oxide scale, indicating other factors also play a major role.

The thickness of an oxide scale plays an important role in development of stresses in the oxide scale. According to the PBR, epitaxial oxide scale is one of the major stress development factors. However, the stresses that develop tend to limit the epitaxy to about 50 nm of oxide scale thickness due to the mismatch between the oxide crystal and the metal crystal [107]. The growth of the thicker scale will negate the effect of epitaxy stresses.

Most of the metal oxides are polycrystalline and these generate stresses along their grain boundaries because of short-circuit diffusion, which may lead to oxide formation at the grain boundaries thereby increasing the compressive stresses. In addition, the presence of second phases that may oxidize at a different rate can create stresses within an oxide.

A composition variation within a scale due to deviation from stoichiometry can also create the stresses in the oxides. Further, compositional variation in the bulk material will result in selective oxidation. If the diffusion of a reactive element within the bulk material is too slow to maintain the critical composition at the metal/scale interface, stress develops at the interface.

According to Bernstein [21], the PBR model was primarily based on the volume difference between the metal and the oxide; this difference produces a strain within the oxide scale, which generates stress in the oxide and the metal. Bernstein [21] modified the PBR model by applying a strain factor to limit the theoretical strength to match exact oxide scale stress.

Because neither the PBR nor the Bernstein [21] model can correctly predict stresses in a complex alloy/oxide system, these models are not generally useful. Further, under service conditions the majority of stresses are generated by both growth and thermal cycling. However, neither of these models takes into account the latter.

2.14.1.2. Thermal stresses

Thermal stresses are generated during cooling from the oxidation temperature due to the differences between coefficients of thermal expansion (CTE) of the substrate and oxide scale. A fundamental understanding of CTE mismatch during thermal cycling is essential. Additionally, a metal and oxide system undergoes temperature changes, which gives rise to phase transformations resulting in changes in internal stresses in both metal and oxide phases [3], [7]. In most cases, the thermal expansion of the oxide is less than that of the metal; therefore, compressive stress develops in the oxide during cooing. Multilayered scales will develop additional stresses at the oxide/oxide interface.

2.15. Breakaway oxidation due to depletion of alloying elements

Breakaway oxidation is often associated with stress-induced oxide cracking [14], [132]. These works reported that parabolic oxidation behaviour is often interrupted by periodic cracking of a protective scale resulting in a sudden increase in rate when oxygen can react directly with the bare metal surface. As the oxide scale begins to cover the metal surface again, parabolic oxidation resumes. The period between successive parabolic steps is sometimes uniform because when the oxide scale growth reaches a critical scale thickness, a crack will initiate. The overall oxidation of the metal then approximates a slow linear process [3].

Occasionally, a metal oxidizes parabolically until the scale cracks or spalls off and from that time on, the oxidation is linear [3]. The oxide, initially protective, completely loses its protective properties once the spallation begins. This is termed as breakaway oxidation and commonly occurs if many cracks form continuously and extend quickly through the oxide. The spallation is the common mechanism if the alloy cannot maintain critical concentration of scale-forming element at the scale/alloy interface, which results in exposing base metal surface. Breakaway oxidation will leave bare metal continually exposed, unlike paralinear oxidation in which an inner protective layer always remains [133], [134]. It can also occur due to selective oxidation in multicomponent systems [135], [136].

2.16. Void formation

When metals/alloys are exposed to an oxidizing environment, they will form a stable oxide scale depending on their composition, which inhibits further oxidation of the alloy. However, interdiffusion at the metal/scale interface can lead to porosity and voids/cavity. The formation of voids and subsequent void growth in the subscale region during oxidation can be explained by the following mechanisms [137]–[139],

- Vacancy injection results from the fact that diffusion of metal atoms into the scale, which is undergoing oxidation, must be counterbalanced by inward diffusion of oxygen, or the Kirkendall effect [140], [141].
- Moreover, parabolic oxide layer growth leads to a volume change between the oxide layer and the alloy, which in turn increases the tensile stresses. To accommodate this net volume change, creep cavity or voids will form beneath the oxide layer [142].

2.17. Oxidation of alloys

2.17.1. Kinetics of alloy oxidation

The oxidation resistance of a metal may be modified by adding several alloying elements, which renders it suitable for a different high-temperature application. The oxidation of an alloy is generally much more complicated than pure metal oxidation and depends on many factors such as [7], [107], [125]:

1. Each alloying element will have different affinity for oxygen reflected by their free energies of formation.
2. Multiple oxide phases may be formed.
3. A degree of solid solubility may exist between the oxides.
4. The difference in cationic mobility in oxide phases.
5. The difference in the diffusion coefficient of metals in the alloy.
6. The dissolution of oxygen into the alloy may result in internal oxidation.

2.17.1.1. Selective oxidation

Selective oxidation is generally known as preferential oxidation of solute in an alloy that forms a continuous oxide layer on the surface. The process occurs based on the thermodynamic stability of the particular oxide [3], [143].

Consider a system A-B, where A represents a more noble component than B and BOv is the oxide being formed. When the scale growth is controlled by diffusion of component B in the alloy, the scale/alloy interface can become unstable. Wagner [114] showed that a critical

concentration of B, N_B^c , at the scale/alloy interface is necessary to maintain the BOv formation, which is given by,

$$N_B^c = \frac{V_m}{32v}\left(\frac{\pi k_p}{2D}\right)^{1/2} \quad (18)$$

Where, k_p is the parabolic rate constant, D is the interdiffusion coefficient , V_m is the molar volume of the solvent alloy and v is the stoichiometric parameter in the oxide BOv.

2.17.1.2. Internal oxidation

Internal oxidation is defined as the formation of oxide precipitates within an alloy [7]. This is also called sub-scale formation and occurs when oxygen dissolves in an alloy either at the metal/oxide interface or on the bare alloy surface when the partial pressure of oxygen is lower than the dissociation pressure of the bare metal oxide. Internal oxidation results when an alloying element is selectively oxidized but cannot reach the surface quickly enough to develop an external scale. Internal oxidation in an alloy will change the mechanical properties of the alloy. For example, the subsurface depletion of alloying elements during oxidation will change the tensile stresses at the region [144], [145]. Wagner has proposed a relationship to determine the internal oxidation thickness, in which the external oxide layer and internal oxidation zone thickness are independent of solute concentration. The relation is given by [3], [7], [84], [105]:

$$\xi = \left(\frac{2N_O^s D_O t}{\nu N_B^O}\right)^{1/2} \quad (19)$$

Where ξ is the internal-oxidation zone, D_O is the diffusivity of oxygen in the alloy, N_O^s is the oxygen solubility at the surface (mole fraction), D_O is the diffusivity of the oxidant in the alloy, N_B^O is the mole fraction of solute in the alloy and t is time (s).

The basic assumption of the Wagner model [84] is that diffusion is controlled by lattice diffusion. This mechanism is only valid at high temperatures or in single crystal materials. At lower temperatures, grain boundary diffusion is more predominant because a grain boundary acts as a rapid diffusion path for the migration of both oxygen and metal ions [99], [105], [146].

2.17.1.2.1. Kinetics of internal oxidation

Like the oxidation process, which forms an external scale, internal oxidation also follows a particular kinetics law. Its growth with time is an important parameter, which can give information about the internal damage of an alloy. It is imperative to know the interdiffusion coefficients of the alloying elements to understand the mechanism of formation of a γ' precipitate free zone (PFZ), especially chromium and aluminum ($\widetilde{D_{Cr,Al}}$) since they are the main scale-forming elements [42]. During oxidation of commercial alloy systems, the depletion of alloying elements is the main problem in the subsurface zone. For instance, formation of a protective oxide scale on the surface of a binary Ni-Cr alloy during oxidation results in depletion of Cr from the subsurface zone [11]. To maintain oxidation resistance, the alloy should continuously feed Cr to the oxide scale thereby decreasing the Cr content in the subsurface zone. However, the diffusion coefficient of Cr mainly depends on the alloy composition and the concentration gradient in the elemental depleted region. A similar effect can also be seen in alloys, which have an internal Al_2O_3 formation due to selective oxidation of Al from both matrix and γ' precipitates. The concentration profile of Cr and Al will change in the subsurface zone due to continuous migration of these elements to form their

respective oxides over time. The interdiffusion coefficient of Cr and Al in the subsurface zone can then be determined by measuring their respective concentration profiles. This calculation will help to understand the scale spallation mechanism and mechanical properties.

2.17.1.3. The transition from internal to external oxidation

Wagner [81] states that the transition from internal to external oxide formation occurs when the volume fraction of the oxide reaches a critical value f*. This condition decreases the inward flux of oxygen and increases the outward flux of metal ions, which eventually form a continuous oxide layer on the alloy surface at lower solute concentrations. The criterion for the formation of an external scale is given by the equation,

$$N_{B^*}^{O} > \left[\frac{N_O^s \pi f^*}{2v}\left(\frac{V_m}{V_{ox}}\right)\left(\frac{D_O}{D_B}\right)\right]^{1/2} \quad (20)$$

Where $N_{B^*}^{O}$ is the critical mole fraction of B in the alloy, V_m is the molar volume of the alloy, V_{ox} is the molar volume of the oxide, D_0 and D_B are the diffusion coefficients of solute B and oxygen in an alloy.

2.18. Diffusion profiles and phase dissolution

Generally, high oxidation-resistant alloys are placed in a phase dissolution category [102]. For example, high-temperature oxidation-resistant Ni-base superalloys consist of a Ni-rich FCC-γ matrix with uniform distribution of γ'-Ni_3Al precipitates. At elevated temperatures, a major

contribution to the high strength comes from these γ'-Ni_3Al precipitates [12] [38] [24] [43] [53]. Typically, oxidation of chromia-forming alloys involves external Cr_2O_3 scale formation with a branched Al_2O_3 internal subscale. Thus, some of the intermetallic γ'-Ni_3Al are solutionized [103]. When the aluminum concentration in the subsurface matrix reaches a minimum, the γ'-Ni_3Al phase acts as an aluminum reservoir for further growth of an Al_2O_3 scale [27], [147].

The rate of Al_2O_3 subscale formation and the γ'-Ni_3Al precipitate dissolution also depend on the aluminum concentration in the precipitates. According to Chen [104], the γ' composition is precipitate-size dependent in an RR1000 alloy. The aluminum content of secondary γ' precipitates was found to be greater than in the primary γ' precipitates, resulting in a higher concentration gradient for smaller precipitates; thus the dissolution of finer precipitates is faster than that of the larger ones.

For most Ni-base superalloys the main strengthening precipitates are chromium-based carbides, e.g. of the type $M_{23}C_6$ [105]. During high-temperature service time, formation and growth rate of a chromia scale on the surface of the alloy results in the depletion of surface and grain boundary carbide precipitates which are rich in chromium. The dissolution of $M_{23}C_6$ helps to sustain the Cr_2O_3 scale growth.

In general, for the formation of an oxide scale BO, the concentration of B in the alloy is required to be larger than the critical concentration, N^{α}_B [3], [7]. When BO is formed as an external scale, the alloy is depleted in B, as represented in Figure 2-3, where N^{o}_B is the mole fraction of the original alloy B and N^{i}_B is the concentration of B at the oxide scale/alloy interface [17].

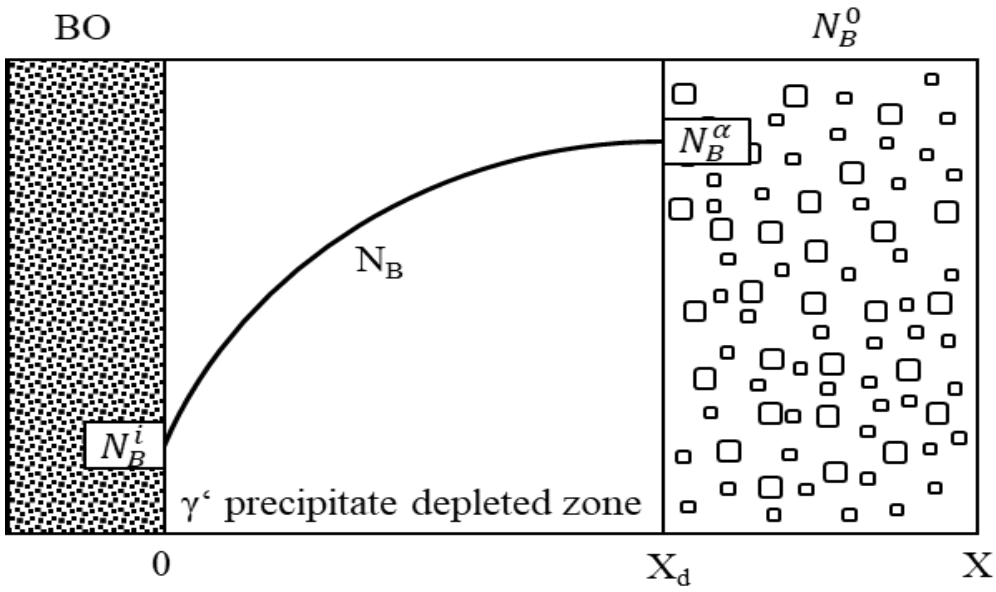

Figure 2-3. Diffusion profile in the subsurface region of two-phase alloy AB undergoing selective oxidation causing dissolution of solute-rich B-phase to form oxide scale of BO (Reproduced with permission from Elsevier.) [3], [7].

To maintain equilibrium between precipitate and the local matrix, the dissolution of the precipitate phase (B) is assumed to be fast. If the diffusion of solute element B through the precipitate-depleted subsurface alloy region is rapid enough to continue external scaling, the concentration of B at the scale/alloy interface N^i_B would be constant.

Diffusion analysis is used to describe the concentration profile of B in the precipitate depleted or precipitate free zone (PFZ) as in Figure 2-3 [106]. By equating the flux of B in alloy with oxide scale results in the expression:

$$N^o{}_B - N^i{}_B = \frac{u}{\gamma \exp(\gamma^2)} + \pi^{\frac{1}{2}} u \,.\, \mathrm{erf}(\gamma) \qquad (21)$$

Where X_d is the depth of the precipitate depleted or free zone and u and γ are functions of the rate constant k_c which are given by the following expressions,

$$u = \left(\frac{k_c}{4D}\right)^{\frac{1}{2}} \tag{22}$$

$$\gamma = \left(\frac{X_d}{4Dt}\right)^{\frac{1}{2}} \tag{23}$$

Therefore, it is very important to understand the PFZ dependence on precipitate size during oxidation.

2.19. Interdiffusion coefficient models

Diffusion is a process of transportation of a given species from high concentration to a low concentration, i.e. down a chemical potential gradient [114], [148]. The diffusion gradients established for the interdiffusion of two solids may take different forms. For example, the selective oxidation of Cr in an alloy to form an external Cr_2O_3 scale lowers its concentration within the alloy; therefore, there is a concentration gradient of Cr in the subsurface zone of an alloy. If diffusion of Cr is rapid compared to the scale-forming rate, then the change in concentration of Cr in the alloy/scale interface will be small since the change in Cr concentration is averaged over a large region. However, if the diffusion of Cr is relatively slow in the alloy due to the depletion of Cr in the subsurface zone (Figure 2-3) then the change in concentration at the alloy/scale interface is large resulting in scale spallation. Thus, to predict the useful lifetime for an alloy based on oxidation resistance, it is fair to use the oxide scale behaviour or the diffusion rate of the reactive species. For instance, during the oxidation of a high Cr-containing alloy, the Cr level at the

alloy/scale interface will be maintained due to continuous diffusion of Cr from the bulk alloy to the alloy/scale interface.

Fick's first law governs the diffusion of reactive species. The law states that the diffusion flux is directly proportional to its concentration gradient and it occurs down the gradient. For unidirectional flow, the law is given by [20], [149]:

$$J = -D \cdot \frac{dN}{dx} \tag{24}$$

Where D is diffusivity (cm^2/s), J is the molar flux in the x-direction ($mol.cm^2/s$), x is the distance in cm and N is the molar concentration ($mol./cm^3$). The interdiffusion molar flux for an i^{th} element in a multicomponent system can be written as:

$$\widetilde{J_i} = -\sum_{j=1}^{n-1} \widetilde{D_{ij}^n} \frac{\partial N_j}{\partial x} \tag{25}$$

where $\widetilde{J_i}$ is the interdiffusion flux of element i, $\widetilde{D}$ is the interdiffusion coefficient and is a function of composition. The term n is the dependent variable, such that (n-1) interdiffusion coefficients are required to determine the molar flux in a multicomponent system and $\frac{\partial N_j}{\partial x}$ is the concentration gradient of the j-component. In the case of diffusivity as a function of concentration, Fick's second law applies, which is given by [150]:

$$\frac{\partial N}{\partial x} = \frac{\partial}{\partial x}\left(D \frac{\partial N}{\partial x}\right) \tag{26}$$

Boltzmann followed by Matano developed an equation to account for the variation of the diffusion coefficient as a function of composition. This is a graphical method as shown in Figure 2-4, which relates the form of diffusion profile with concentration-dependent interdiffusion coefficient, $\widetilde{D}(c)$ [151], [152].

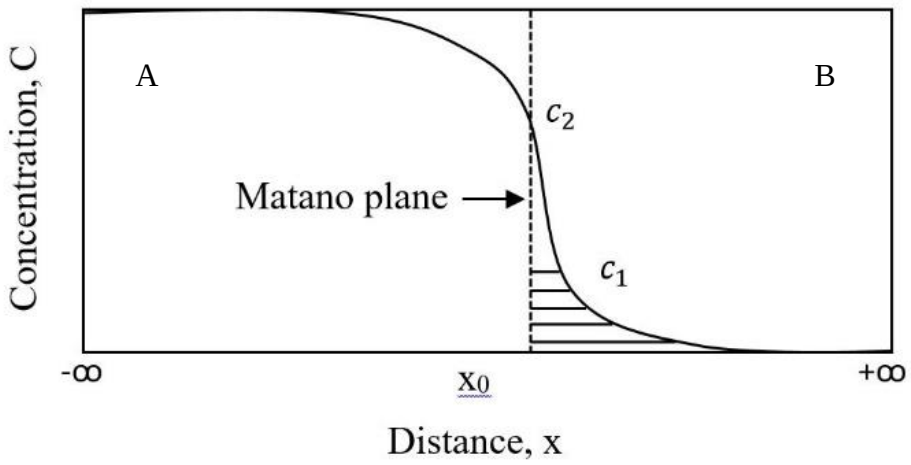

Figure 2-4. Illustration of a concentration profile for reactive species in an infinite solid-solid diffusion couple (Reproduced with permission from Elsevier) [151], [152].

The Boltzmann-Matano analysis to determine the interdiffusivity is given by [152],

$$\widetilde{D} = -\frac{1}{2 \cdot t} \cdot \frac{dx}{dc} \cdot \int_{c_1}^{c_2} x \cdot dc \tag{27}$$

Equation (27) can be used to determine the interdiffusion coefficient, $\widetilde{D}(c)$ by graphical construction. The derivative in equation (27) is calculated from the concentration profile at time t and the integration is performed on the inverse of concentration, C. The boundary condition, $\int_{c_1}^{c_2} x \cdot dc = 0$ determines the position of the original Matano interface where x= 0. The Matano interface is defined as the cross section through which there have been equal total fluxes of the reactive species of A and B [141], [153].

2.20. Effect of alloying elements on oxidation of superalloys

The roles of the alloying elements used to promote oxidation resistance in superalloys are summarized below.

Chromium: Addition of chromium is an excellent choice for high-temperature alloys (below 950°C) by virtue of formation of a natural protective layer of chromium oxide (Cr_2O_3) which adheres to a surface. The critical chromium concentration to form a protective Cr_2O_3 oxide layer is 15% or 20-25% depending on the application requirements [57] [65]. The addition of chromium is also found to be beneficial for hot corrosion resistance in high-temperature alloys [66]. However, chromia is not effective at temperatures above 1000°C due to its volatility above that temperature [11].

Aluminum: It is one of the best solid solution strengthening elements. Aluminum also offers excellent oxidation resistance by forming a continuous Al_2O_3 layer, which is thermodynamically stable at temperatures well above 1000°C [154].

Titanium: The addition of a small quantity of titanium (≤1 wt. %) to precipitation hardenable alloys increases the volume fraction of secondary strengthening phases such as γ' in Ni-base

superalloys [155]. However, the presence of titanium greater than 1 wt. % has been found to be detrimental to the oxidation resistance of chromia-forming alloys [13], [142], [156]. TiO_2 is thermodynamically more stable than Cr_2O_3 and thus TiO_2 may form below an external scale of Cr_2O_3 as an internal oxide. In Cr-rich alloys, the Ti tends to oxidize at both the gas/scale interface and metal/scale interfaces. According to Yang [71], the addition of 1% of Ti to a Ni-base superalloy increases the oxidation resistance; however, the same alloy with 3% Ti increases the oxidation rate at 1000°C. An oxide growth rate generates growth stresses resulting in a decrease in the adherence of the oxide layer thus being detrimental to the high-temperature oxidation resistance.

Cobalt: The oxidation resistance of cobalt is similar to that of nickel. At high-temperatures the oxidation rate of cobalt increases, forming a porous non-protective oxide layer. The oxidation rate of unalloyed cobalt in air is reported to be 25 times that of nickel [72]. Cobalt is also used to reduce the amount of solid solution strengthening elements.

Niobium: The addition of niobium will stabilize any grain boundary carbide precipitates [157]. The presence of Nb may also decrease the intergranular oxidation rate [158]. Niobium substitutes for Al in γ' as does Ti [73].

Rhenium: The addition of Re to a Ni-base superalloy increases the oxidation resistance at high temperatures by lowering the subsurface Al depletion in γ'. Czech [78] stated that rhenium acts a diffusion barrier inhibiting the inward and outward diffusion of alloying elements. Liu's [79] experiments on Ni-base superalloys DD32 and DD32M also agree with Czech.

Molybdenum and tantalum: Molybdenum is not the best material regarding oxidation as it begins to oxidise in air at 300°C and above 500°C, oxidation becomes more rapid [90], [159]. At 1200°C,

the oxidation rate is very rapid and catastrophic [159]. The oxidation of Mo below 500°C follows a parabolic rate law, which suggests a protective scale at low temperature. The oxidation of Mo exhibits a two-step process; initially, MoO_2 is formed at the metal/oxide interface region and later MoO_3 is formed. MoO_3 is volatile above 500°C, and the rate of evaporation increases significantly at 600°C [160].

Tantalum is one of the most corrosion-resistant metals and oxidizes to form a thin and continuous surface film of Ta_2O_5. The electrochemical reaction between Ta and oxygen starts above 300°C and becomes rapid above 600°C. Koftad [130] has done extensive research on oxidation of Ta over the temperature range 300°C to 1300°C. The Ta_2O_5 scale formed is not adherent and if the oxidation temperature is increased to 1000˚C, oxygen diffuses into the bulk of the material causing embrittlement [7]. It has been reported that replacing Ti with Ta increases the oxidation resistance considerably [71]. However, increasing the Ta concentration by 1% to 3% has been reported to make the formation of Al_2O_3 less favourable [142].

Zirconium and hafnium: Additions of zirconium and hafnium can significantly improve the mechanical properties such as thermal creep deformation resistance. The diffusion rates and carbide agglomeration along a grain boundary can be decreased in the presence of these elements. Hafnium contributes to the formation of γ-γ' eutectic phases at the grain boundaries [1]. These elements are oxygen getters and help in the formation of healing layers of alumina and chromia [161], [162].

2.21. Pettit's oxidation groups

Giggins and Pettit [126] summarized the three major oxidation modes in Ni-Cr-Al ternary alloys at 1000°C. For the initial stage of oxidation, an outer layer of NiO is formed together with subscale

precipitates of Cr_2O_3, Al_2O_3 and $Ni(Cr, Al)_2O_4$. This type of oxidation is termed as "Group I" oxidation mode or NiO formers. The "Group II" oxidation mode can be seen in alloys with higher Cr content and less Al such as Ni-20Cr-2Al. Here, an outer Cr_2O_3 layer is formed and the oxidation rate is controlled by the migration of ions across the Cr_2O_3 scale. Finally, for alloys with higher Al content such as Ni-20Cr-4Al, the "Group III" oxidation mode was observed. Here, Al_2O_3 forms as a continuous external scale, which controls the rate of oxidation. The ionic transport in Group III alloys is much slower than for those in Group I and Group II. The schematic diagram of oxide scale development on Ni-Cr-Al alloys as a function of time at 1000ºC is shown in Figure 2-5 [15] [65].

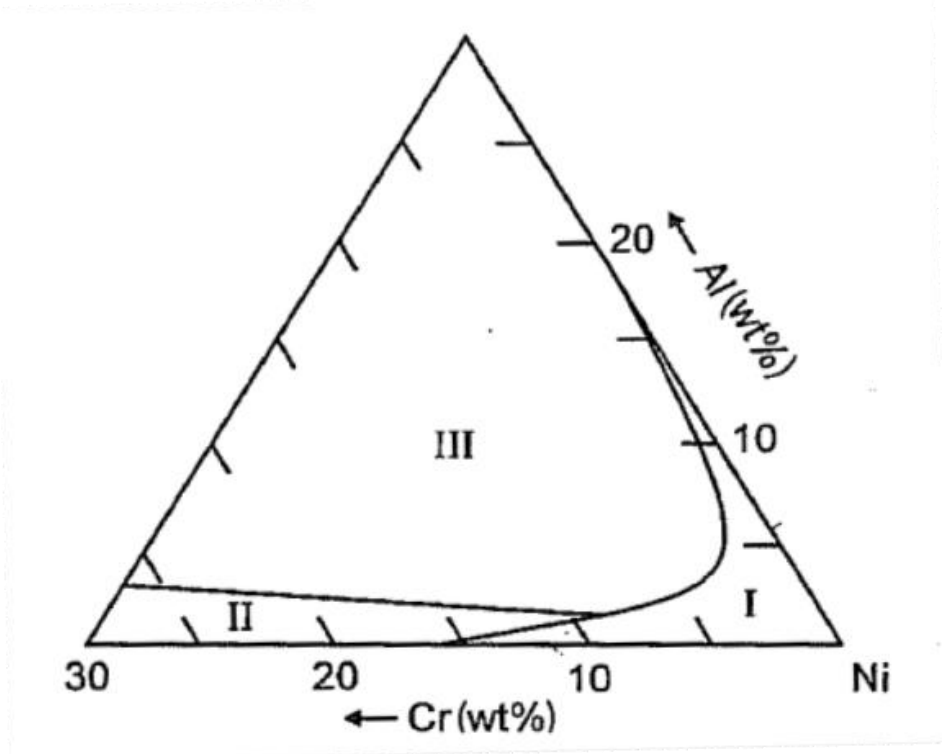

Figure 2-5. Effect of composition on oxidation of Ni-Cr-Al ternary alloys (Reproduced with permission from Cambridge University Press) [15] [65].

2.22. Characteristics of oxides

2.22.1. Chromium oxide

Both chromium and aluminum oxides have the corundum crystal structure and are assumed to be hexagonal close packed (HCP), where each Cr atom (octahedral sites) is surrounded by 6 oxygen atoms [163]. Cr_2O_3 provides significant resistance to both corrosion and oxidation even at elevated temperatures [100]. The oxide acts as an intrinsic semiconductor above 1250°C [164] and shows both p-type and n-type semiconducting behaviour depending on the temperature. Lillerud and Koftad [163] reported the temperature-dependent defect type variation in Cr_2O_3. In most cases, Cr_2O_3 exhibits p- or n-type ionic defects (doping defects) at lower temperatures, whereas, when it exposed to temperatures above 1000°C, an equal amount of holes and electrons will form, which also depends on partial pressure of oxygen at that temperature [115]. Greskovitch [165], reported that since Cr_2O_3 is cation-deficit it deviates from stoichiometry at 1100°C due to an increase in activity of $(O_2)^{1/8}, a_{(O_2)^{1/8}}$. Also, at a low partial pressure of oxygen, Cr shows the ionic defects to be at interstitial positions [165].

A tracer diffusion experiment conducted by Atkinson and Taylor [156] stated that the diffusion of Cr in Cr_2O_3 occurs by a cation-vacancy migration process, which depended on the defect structure. Similarly, Mitchell [166] concluded that the growth of Cr_2O_3 occurs due to outward diffusion of Cr. In contrast, Barnes [167] and Lees and Calvert [168] have concluded that the growth of Cr_2O_3 at elevated temperatures is also possible by other anionic migration mechanisms apart from lattice diffusion. Grain boundary diffusion is one such mechanism where rapid migration of cation and anion will take place, which significantly increases the growth rate of a chromia scale at elevated temperatures [156], [169], [170]. The microstructure of metal or

alloy also plays an important role in determining the rate of oxidation. As grain size decreases, the number of grain boundaries increases, therefore the rate of oxidation increases.

The oxidation resistance and scale adherence of chromia-forming metals are also influenced by the presence of other reactive elements such as Y, Hf, Zr, Si, Ce and La [171]–[173]. However, chromia scale performance is limited to temperatures below 900°C as the chromia scale changes from Cr_2O_3 to the volatile species CrO_3 above that temperature, which decreases the scale thickness and increases the migration of metal ions through the scale [174]. The deterioration will increase significantly at temperatures above 1000°C. Hence, an alumina scale is preferable at these temperatures, as Al_2O_3 is thermodynamically more stable and does not form any significant volatile matter at these temperatures [3], [7].

2.22.2. Aluminum oxide

Aluminum oxide exhibits a similar structure (corundum) as chromium oxide, where aluminum atoms occupy octahedral sites. The formation of continuous Al_2O_3 on the surface of an alloy depends on the aluminum content in the alloy. Typically, the alloy must contain 6-12 wt.% of Al to exhibit a continuous Al_2O_3 scale [175]–[177]. However, Stott et al. [175] concluded that the presence of a third alloying element such as Cr (15-20 wt.%) in the Ni-Al system containing four weight percent aluminum enhances the development of a continuous Al_2O_3 scale. Al_2O_3 is thermodynamically more stable than Cr_2O_3 at elevated temperatures [7]. The oxide shows protective behaviour above 900˚C by forming a stable α-Al_2O_3 scale. However, at lower temperatures, transitional and metastable oxides such as γ, Δ and θ- Al_2O_3 are exhibited, which were reported to be less protective than an α-Al_2O_3 phase [178], [179].

The oxidation resistance of alumina-forming alloys at elevated temperatures is controlled by transportation of various ionic species through the α-Al_2O_3. Many researchers have reported that the thickening oxide scale occurs due to both outward diffusion of cations (Al^{3+}) and inward diffusion of anions (O^{2-}) [147], [180]–[182]. Therefore, the combined effect of low ionic defect concentration and slow migration of metal and oxygen ions through α-Al_2O_3 increases the oxidation resistance.

Paladino and Kingery [183] measured the diffusion coefficient of Al in both single crystal and polycrystalline Al_2O_3 samples at temperatures ranging from 1600-1900˚C. The results suggested that diffusion of Al in both lattice and grain boundaries occurs at a similar rate. However, the authors have also reported that the diffusion coefficient of Al^{3+} is greater than for the O^{2-} in Al_2O_3.

Generally, the Al_2O_3 scale that forms on the surface of an alloy will exhibit small and equiaxed grains near outermost scale, whereas coarser and columnar grains appear at the inner region [180]. The vacancy diffusion mechanism of O^{2-} at the scale/alloy interface resulting in an interfacial void has also been reported by several authors [182]. The reason for void formation at the scale/alloy interface has been explained by the Kirkendall effect [161], whereby diffusion of Al^{3+} to the scale/alloy interface is faster than the diffusion of O^{2-} in the opposite direction resulting in excess vacancy formation [4].

The magnitude of oxide scale protectiveness is determined by both oxidation kinetics and structural properties of oxides at elevated temperatures [9], [12]. Typically, a protective scale must be thermodynamically stable, dense, thin and most importantly, it should exhibit good adherence. However, the oxide scale will lose its adhesiveness due to growth stress and thermal stress during isothermal and cyclic exposure conditions [14], [184]. The differences in coefficients

of thermal expansion between scale and substrate during a cooling segment of thermal cycles generates shear stresses at the scale/alloy interface resulting in buckling [180], [185]. Addition of reactive and rare earth elements such as Y, Ce and Sc to chromia and alumina-forming alloys has been found to increase the adhesive property of these oxides [148], [186].

2.23. Cyclic oxidation

Isothermal oxidation tests have been used to determine the oxidation behaviour of superalloys [187]. However, this approach only assesses the mechanism of oxidation, whereas, most of the high-temperature superalloys are exposed to cyclic thermal conditions in service life. These thermal cycles induce thermal stresses in the oxide scale that forms due in part to the differences in coefficients of thermal expansion, resulting in cracking and scale spallation, thereby changing the oxidation kinetics. For example, it has been reported that the oxidation attack was more severe on Ni-based superalloys PWA1480, under cyclic conditions than under isothermal conditions [188]. Thus, an understanding and determination of the cyclic oxidation behaviour are required to appreciate the behaviour of such alloys at high-temperatures under service conditions and as a result, the cyclic oxidation test is considered to be one of the most critical testing procedures to determine the service lifetimes of these alloys.

Scale spallation is a major failure mechanism in high-temperature materials during cooling from service temperature [189]. The temperature change and the coefficient of thermal expansion mismatch between the alloy and scale impose thermal stresses; the oxides show ductile behaviour at high temperature and are brittle at lower temperatures. If there is no stress relief mechanism available, the thermally induced strain energy increases at the scale/alloy interface[14]. When the elastic energy per unit area at the scale/alloy interface crosses a critical limit, then scale spallation

occurs. The thermal stresses first initiate a crack, which gradually propagates with an increase in thermal cycles, followed by scale spallation. The repeated spallation exposes a non-protective or less protective scale resulting in a phenomenon called breakdown, which is the transition from a stable and protective scale to more rapid scale growth [148].

2.24. Oxidation modelling

As previously noted, in service life, superalloys typically undergo cyclic oxidation at high temperatures. Under these conditions, the spallation of the protective scale is a major concern and isothermal oxidation does not provide insight into this spallation behaviour [7], [14], [190]. Over the past years, a number of researchers have developed models to investigate the growth kinetics, magnitude of spallation and rejuvenation process of superalloys under cyclic conditions [191]. For example, Evans and Lobb [192] investigated the decohesion of oxide scale due to increased strain energy at the oxide-scale interface. Schutze [193] used fracture mechanics to measure the adhesion strength and concluded that the decohesion of scale occurs due to the presence of cracks at the scale-alloy interface. Similarly, Cahn [194] measured the fracture toughness or stored strain energy by injecting microcracks at the scale/alloy interface using fracture mechanics. The calculated and observed weight change of these authors were comparable.

There are four different mechanistic models to determine the factors affecting cyclic oxidation: cyclic oxidation spallation program (COSP) uniform model [195], COSP Monte Carlo model[196], deterministic interfacial cyclic oxidation spallation model (DISCOM) [197] and a statistical model developed by Monceau [198]. These models generate mass change as a function of oxidation cycle curves by quantifying the scale growth and a mass loss. The curves developed by these models are then fitted to the experimental results. Each model works on the basic principle

of oxide formation during a heating segment of a cycle at high temperature and subsequent spallation during the cooling segment. Where these models differ from each other is based on statistical calculations of scale spallation during cooling.

2.24.1. COSP-uniform model

The COSP-uniform model is the simplest model among the four and is described as follows. The oxide growth during the initial cycle is and considered to be due to an isothermal effect, where the growth rate follows a prescribed behaviour. Each cycle is a combination of heating and cooling. The specific weight of the oxide after a heating segment W_r' is determined using isothermal oxidation kinetics. The subsequent cooling step of the cycle will lead to a fraction of scale spallation. The total mass of the oxide retained on the surface (W_r) after each cycle is the starting point for the next cycle, which is shown in Figure 2-6 [196]. In this model, there are two major assumptions. First, the growth kinetics is constant and it is a function of scale thickness. Second, the amount scale spallation after each cycle depends on the amount of oxide scale present on the previous cycle.

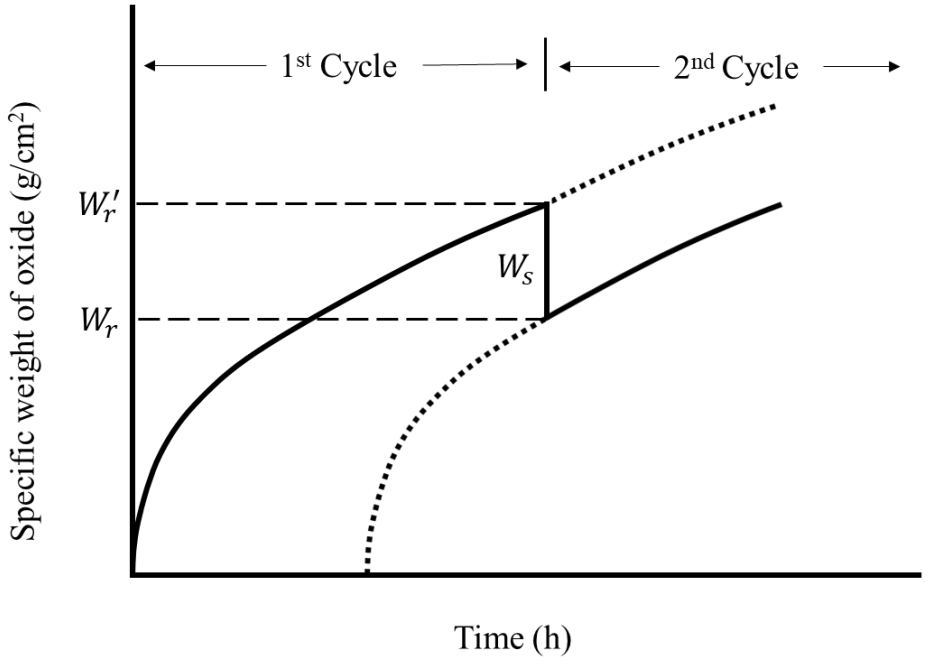

Figure 2-6. COSP-uniform layer modelled specific weight change as a function of time at oxidation temperature (Reproduced with permission from Springer) [196].

The model is described as follows. Consider a material that follows parabolic oxidation behaviour, where the rate constant is k_p. As discussed before, on the first cycle, the specific weight of the oxide can be calculated as follows,

$$\left(W'_{r,i}\right)^{\alpha} = \xi \cdot k^{1/2} \cdot \tau^{1/2} \tag{28}$$

Where τ is the time at oxidation temperature per cycle, ξ is the ratio of the mass of oxide to the mass of oxygen (stoichiometric constant), and α is a spallation exponent, assumed to be greater than zero. The subscript *i* represents the cycle number. In this model, the amount of scale spallation occurs during the cooling segment of the cycle. The portion of the scale spalled is always assumed

to be thin with uniform thickness. The scale spallation may occur at the scale/alloy interface or within the scale and this type of cohesion requires a crack within the scale or at the scale/alloy interface. The amount of oxide spalled is expressed in terms of the fraction of scale spallation (F_s), which is directly proportional to the specific weight of the oxide. The relation is given as:

$$F_s = Q_0 \cdot \left(W'_{r,i}\right)^{\alpha} \tag{29}$$

Where, Q_0 is the spall constant. Equation (29) was developed by carefully measuring the weight change during cyclic oxidation of a NiCrAlY alloy [196].

A typical weight change curve along with the effect of spall constant Q_0 is shown in Figure 2-7 [184], [196]. It can be seen that with an increase in spall constant value, the number of cycles required to cross zero weight change decreases.

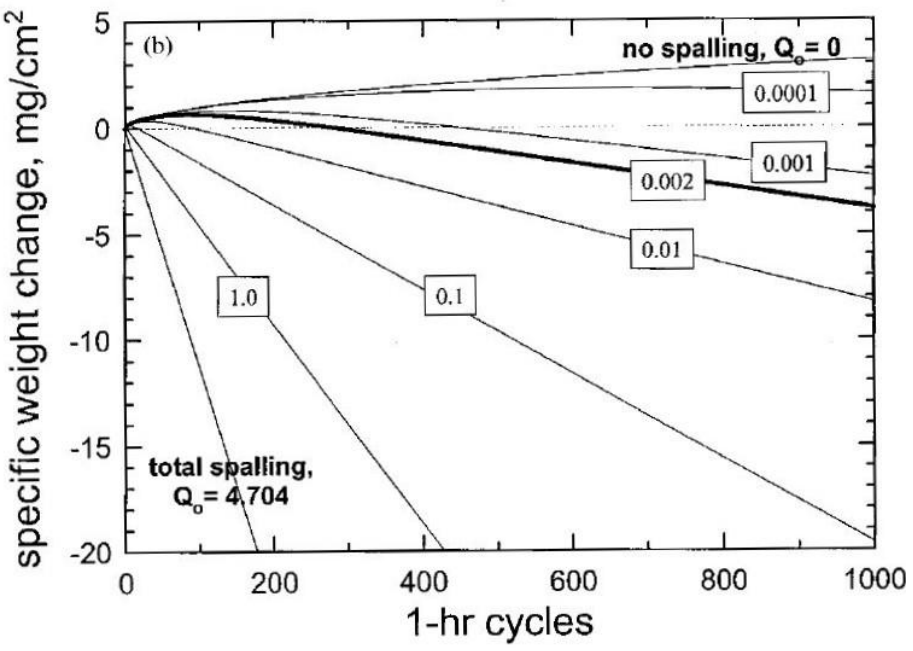

Figure 2-7. The effect of spall constant, Q_0 on standard baseline COSP model curves for parabolic growth and uniform spalling of an Al_2O_3 scale (Reproduced with permission from Springer) [184], [196].

2.24.2. COSP-Monte Carlo model

In service life at elevated temperatures, the scale spallation on the surface is more localised spallation (discreet spallation) rather than being uniform spallation on the entire surface. Hence, the COSP Monte Carlo model is more representative of the actual scale spallation in an alloy. In this model, the surface of the sample is divided into multiple segments of equal areas. The growth and the spallation in these areas are independent of each other. These discrete areas are controlled by the probabilistic manner using the Monte Carlo technique. The specific weight of the oxide is calculated similar to that of COSP-uniform layer model; however, the fraction of oxide spalled, $\overline{F_s}$ is expressed using probability, which is given by,

$$\overline{F_s} = (1 - P) \cdot F_1 + P \cdot F_2 \tag{30}$$

and,

$$\overline{F_s} = Q_0 \cdot \left(W'_{r,i}\right)^{\alpha} \tag{31}$$

To deviate completely from the uniform layer, F1 is set to zero and F2 is equal to unity. Then equation (29) reduces to:

$$P = Q_0 \cdot \left(W'_{r,i}\right)^{\alpha} \tag{32}$$

The effective time, t_{eff} in the COSP-Monte Carlo model can then be calculated using the simple equation:

$$t_{eff,i} = \tau \cdot n \quad (33)$$

where n is the number of cycles. The oxidation behaviour of the material during thermal cycling is determined by averaging the all the discreet spallation areas. This model was implemented to determine the life of simple chromia-forming (Ni-Cr-Al) and alumina-forming (Ni-Al) alloys [196]. The modelled results are fitted to the experimental data to find two major unknowns, i.e., the parabolic rate constant and the spall constant. Even though the parabolic rate constant can be obtained by a simple oxidation test for small time durations, determining the spall constant is very difficult.

2.24.3. DISCOM and statistical Monceau model

Both of these models are similar to the COSP-Monte Carlo model, which assumes parabolic growth kinetics, but a different spallation format is applied. For example, spallation is assumed to be always at interfacial locations and over a constant area fraction during each cooling step. In the DISCOM model [197], the surface is divided into equivalent segments and these segments are the inverse of the spalling area fraction. One more assumption is that the spalling will occur only for the thickest scale segment. Since the scale decohesion is occurring at the scale/alloy interface, fracture mechanics is used to address the fracture toughness or stored strain energy at the interface [197]. The Monceau model [199] is similar to the DISCOM by Smialek [197]. In this model, the surface is divided into surface segments of identical sizes, and these segments are grouped according to the oxide thickness. The oxide spallation from each thickness is kept constant

according to a constant area fraction analysis. Monceau has developed a simple statistical model to find the analytical solution for cyclic oxidation data.

In service life at elevated temperatures, the scale spallation on the surface is more localised spallation (discreet) rather than the uniform spallation on the entire surface. Hence, the COSP Monte Carlo model is more representative of the actual scale spallation in alloys. The current research was focused on the COSP-Monte Carlo model.

2.25. Corrosion and oxide scales

Oxide scales that form on a metal surface at lower temperatures are generally due to either atmospheric air or electrochemical reaction [200]. Corrosion is an electrochemical reaction between the metal and the corrosive environment with transfer of electrons from metal to the environment; therefore, a change in valence occurs from zero to a positive value. The corrosive environment may consist of liquid or gas; these environments are called electrolytes, which act similarly to a conductive solution with positive and negatively charged ions (cations and anions respectively) [201]. Corrosion is termed as being an electrochemical process due to the flow of current between anodes and cathodes. Therefore, the respective reactions are classified as being anodic and/or cathodic. For instance, if a metal M is immersed in HCl solution, this can be expressed as follows [201]:

$$M + zHCl \rightarrow MCl_2 + H_2 \quad (34)$$

In this example, metal M reacts with the acid solution to form a soluble metal chloride and hydrogen bubbles on the metal surface. This type of reaction is used to clean the surface of metals and for pickling of metals and alloys [202]. The ionic form of the reaction is [201]:

$$M + zH^+ + zCl^- \rightarrow M^{z+} + zCl^- + H_2 \quad (35)$$

By eliminating Cl^- from both the sides of the reaction, we can get anodic and cathodic reactions:

$$M \rightarrow M^{2+} + 2e^- \text{ (anodic reaction)} \quad (36)$$

$$2H^+ + 2e^- \rightarrow H_2 \text{ (cathodic reaction)} \quad (37)$$

The anodic reaction is also called oxidation in which metal valence electrons increase from 0 to +2, releasing electrons, whereas the cathodic reaction (reduction reaction), in which oxidation state of hydrogen decreases from +1 to 0, consumes electrons [201].

When a metal reacts with a corrosive environment, it produces oxide to form metal as a reaction product, for example, cations (Ni^{2+} (aq.)), anions ($HNiO_2^-$ (aq.)) and solid compounds (NiO, $Ni(OH)_2$) [201]. Since corrosion involves a chemical change of one or more reactants at the metal/non-metallic interface, it is considered to be a heterogeneous redox reaction [201].

In brief, the following features can be used to explain the characteristics of a corrosion reaction in liquids [201]:

- The metal and liquid interface will have an electrical connection.
- Migration of +ve charge from the metal surface to the electrolyte, consequently metal oxidised to a higher valency state. Because the migration of +ve charge from the electrolyte to metal surface results in a decrease in ionic species in the electrolyte, it will go to a lower valency state.
- Migration of charge always happens between metal and electrolyte.
- Both thermodynamics and the corrosion kinetics control the stability of corrosion.

2.26. Thermodynamics of corrosion

Pourbaix diagrams are derived from electrochemical measurements and thermodynamic data, which are also called potential-pH diagrams [203]. These diagrams relate electrochemical and corrosion behaviour of metals in aqueous solutions. Furthermore, they also relate stability of a metal with respect to its ions and its oxides. However, these diagrams cannot be used to determine the corrosion kinetics [204].

Only a few metals show thermodynamic stability in all corrosive media as their corrosive potential is higher than the reduction potential of their respective ionic species in the corrosive environment; these metals are called noble metals [201]. In contrast, base metals tend to corrode as they do not meet this requirement. Thermodynamics will only inform whether the reaction is possible or not using the simple electromotive force or EMF series. The EMF is the potential between metals exposed to solutions that contain 1 gm atomic weight of their respective ions [205]. For example, when chromium is immersed in an aqueous solution, the possibility of corrosion is determined by comparing the respective standard electrode and reduction potentials [205].

2.27. Kinetics of corrosion

As mentioned in the previous section, thermodynamics provides information on the possibility of reaction to take place. However, it does not indicate the rate of reaction. The rate of overall reaction is limited by the rate at which the slower of the anodic or cathodic reactions occurs. One of the two reactions is rate controlling. A knowledge of a rate-controlling reaction can often be applied to reducing the corrosion rate. Corrosion rate depends on many factors [206]. Generally, the

reaction kinetics is expressed in terms of the concentration of a reactant used to form a product over a period of time .

When the metal surface and electrolytic solution interface is electrified, the potential at the surface becomes positive as the electrons leave from the metal surface in the anodic region. The equilibrium electrode potential is considered to be zero since the rate of anodic reaction is equal to the rate of cathodic reaction.

The corrosion rate of an actively corroding metal is determined by the intersection of the kinetic curves that caharacterize the anodic and cathodic halves of the corrosion reaction. If the rates of either of these reactions can be changed such that the intersection point is at a lower current density, the corrosion rate is reduced. A schematic of the polarization curve is illustrated in Figure 2-8 [204].

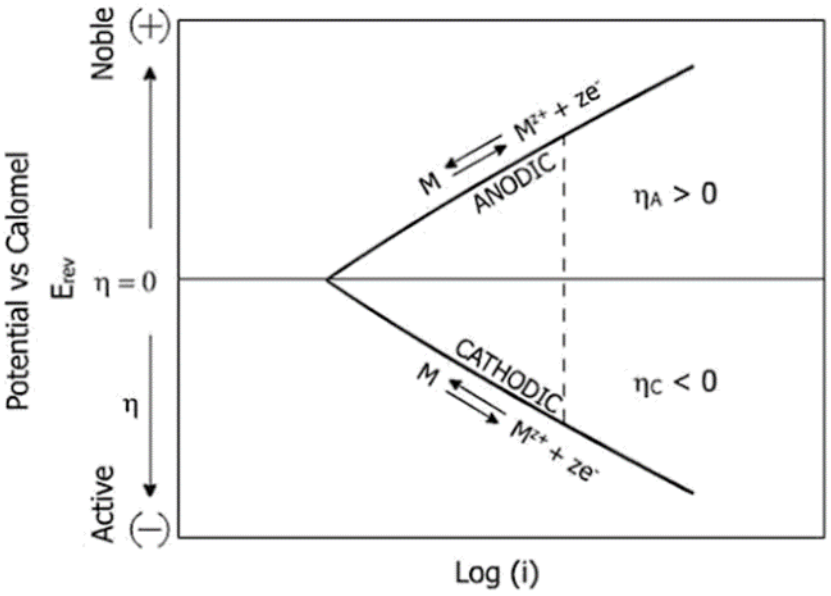

Figure 2-8. Schematic of polarization curve for anodic and cathodic reactions of a metal scale (Reproduced with permission from Elsevier Science & Technology books) [204].

The mass loss using corrosion current density can be calculated with the help of Faraday's law [207]. Here, the main assumption is that one reaction, i.e., metal oxidation, controls the process and other reactions are ignored. The equation is given by [207]:

$$m_{loss} = \left(\frac{M}{z \cdot F}\right) \cdot E_{corr} \cdot t \tag{38}$$

Where m is the metal, M is molar mass of metal and t is time.

Materials that form a protective oxide layer on the surface are corrosion-inhibited; the process being called anodic protection [208]. This type of behaviour has been studied using a three electrode cell; working electrode, auxiliary electrode and reference electrode [205]. When the potential of working electrode is controlled and shifted in the anodic direction, the current required to cause that shift will vary. This behaviour is shown schematically in Figure 2-9 [205].

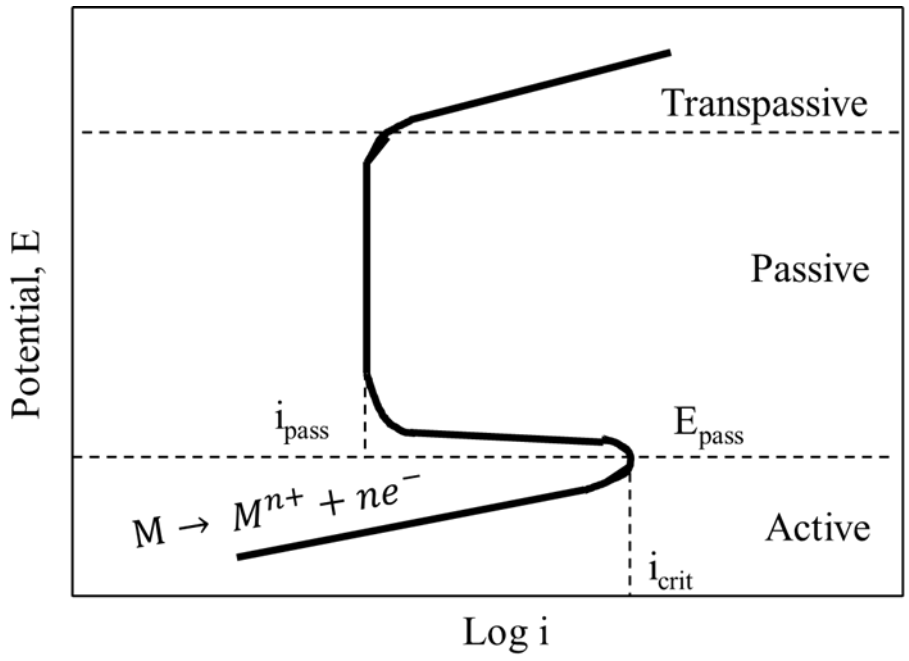

Figure 2-9. Schematic anodic polarization curve (Reproduced with permission from McGraw-Hill) [205].

2.28. Passivation

The oxidation or corrosion resistance of any metal depends on the formation of a passive layer on the surface. Passivity is defined as the loss of chemical reactivity experienced by some metals and alloys in corrosive environments [209]. Once these metals and alloys develop a passive film on the surface, they behave as noble metals. The passive film composition, morphology and mechanism of formation have been studied extensively [108], [210]. For example, a passive film that formed during an electrochemical reaction is thinner compared to that formed by oxidation at elevated temperatures [211]. The composition and thickness of the passive film depend on four major factors: temperature, time, potential and environment [212].

2.29. Passivity breakdown

Passivity breakdown is a typical phenomenon where a passive film completely deteriorates due to the formation of pitting corrosion and subsequently exposing sites to crevice corrosion and stress corrosion cracking [213], [214]. Pitting corrosion occurs randomly on a surface and is extremely localized. The stability of a passive film depends on many factors such as temperature, potential, the concentration of solution and oxide scale composition [209], [214], [215].

Over the past many years, researchers have concluded that the presence of halides in aqueous solutions influences breakdown of the passive film in metals and alloys by forming pitting corrosion [55], [216], [217]. For example, the breakdown of an Al_2O_3 layer can be aggravated with the presence of Cl^- ions [218]. Typical pitting corrosion will occur in a pH range of about 4.5-9.0 [18], [218]. Pitting corrosion exhibits self-limiting corrosion behaviour once the pit reaches a limiting depth, at which point diffusion of metal ions and oxygen ions in or out is no longer

possible. Thus, the concentration of the solution inside the pit decreases compared to that of the surrounding solution. The reaction that takes place inside the pit is known as a hydrolysis reaction (Eq. 47) and is given by [205]:

$$M^{+X} + XH_2O \rightarrow M(OH)_X + XH^+ \quad (39)$$

Where M^{+X} are the positive ions and H^+ are hydrogen ions.

2.30. Corrosion behaviour of Ni-based superalloys

Ni and its alloys generally offer very good corrosion resistant behaviour in harsh environments ranging from sub-zero to elevated temperatures [9]. Ni exhibits a passive film of NiO, which is thermodynamically stable in both moderate and neutral alkaline solutions. However, the film displays poor resistance to corrosion in acidic and strong alkaline solutions [208]. The stability of the passive film is also affected due to the formation of pitting corrosion, which occurs when the metal is polarized above the critical electrode potentials in a chloride solution [214]. Since Ni is a ductile material and acts as a hardenable matrix, it is used as a base material to create strong corrosion resistant alloys such as Ni-base alloys, which can be achieved by adding different alloying elements [1]. The principle elements used to create such alloys are chromium and aluminum [1], [9], [42].

2.31. Purpose of the current study

In summary, oxidation and corrosion resistance are of prime importance when selecting a material for high-temperature application such as aerospace gas turbine engines and nuclear power plants. A common method for improving the oxidation or corrosion resistance of Ni-based superalloys is to alter the chemical composition and microstructure, the beneficial effect of which has been a topic of study for at least 60 years [42], [219], [220]. However, no detailed study exists in the literature on the effect of the principle alloying elements on oxidation behaviour of IN738LC, N5 and Rene 80 Ni-based superalloys, despite the fact that the presence of certain alloying elements affects the oxidation resistance during exposure at high temperatures. Also, microstructure such as grain boundaries can increase the oxidation rate by acting as a rapid diffusion path for alloying elements. The effect of grain boundaries on oxidation behaviour varies from alloy to alloy, which has not been studied in detail.

Furthermore, no information is available about the effect of γ' intermetallic sizes on oxidation and corrosion behaviour, which is the major controlling factor of the oxidation rate and the subsurface degradation such as the formation of internal oxide zone and precipitate free zone. Keeping this background in view, the objectives of this study were:

1. To determine the different composition and microstructural factors affecting the oxide scale kinetics and scale spallation during cyclic oxidation at high temperature for the IN738LC (polycrystalline), N5 (single crystal) and Rene 80 (directional solidified) alloys.
2. Determine the relationship between γ' precipitate size and PFZ, oxidation and corrosion rates.

Chapter 3 Experimental Procedure

This chapter includes the composition of the as-received alloys, a brief description of the heat treatments involved, metallographic preparation of the as-received alloy samples, and isothermal and cyclic oxidation tests to understand the oxidation behaviour of candidate alloys. Further, an aqueous corrosion testing procedure is explained to understand the corrosion behaviour. Finally, this chapter discusses the different characterization techniques used analyse the microstructures of the materials at every stage.

3.1. Materials

PCC Airfoils, Inc. provided the three Ni-based superalloys used for this study; all alloys were in ingot form with dimensions of 150 mm x 64 mm x 10 mm. The chemical compositions of these alloys were analysed by NADCAP, material-testing laboratory and are summarised in Table 3-1.

Table 3-1. The measured chemical composition of the alloys studied.

Composition (wt. %)	Alloys		
	IN738LC	Rene 80	N5
C (LECO)	0.112	0.2	0.06
Cr (XRF)	16.02	14.1	7.14
Mo (XRF)	1.77	4	1.44
Ti (XRF)	3.44	5	0.02
Al (XRF)	3.4	2.9	6.14
Co (XRF)	8.47	9.5	7.44
W (XRF)	2.58	4	4.94
Zr (XRF)	0.028	-	0.02
Nb (XRF)	0.9	0.02	<0.02
Ta (XRF)	1.71	<0.02	6.41
Re (XRF)	0.02	-	2.92
Hf (XRF)	<0.02	-	0.16
Bal.	Ni	Ni	Ni

3.2. Sample preparation

3.2.1. Electrical discharge machining-wire cutting (EDM-WC)

This is a thermal mass-reducing process that uses a continuously moving wire to remove material using rapid, controlled repetitive spark discharges. A thin wire of molybdenum was used as an electrode. A dielectric fluid (water coolant) was used to flush the removed particles, regulate the discharge, and keep the wire and specimen cool. Samples were cut from the as-received ingot materials using a Hansvedt EDM machine giving a surface area of 3.72 cm^2, which is less than those recommended by TESTCORR (the European Guidelines for High-Temperature Corrosion Testing) (20 mm x 10 mm x 5 mm = 7 $cm^2 \pm 0.05$) [221]. However, the sample size is acceptable based on previous work [26], [222], [223]. The wire cutting parameters of the EDM were kept constant for all three alloys, which are summarized in Table 3-2.

Table 3-2. Summary of power parameters used in EDM-WC.

Power parameters	
Pulse	2.8 µ sec
On-time	2.5%
Peak Amps	3 A
Gap spacing	2
Servo speed	13
Cut-off	1

3.2.2. Heat treatment

The heat treatment processes are divided into conventional and continuous cooling heat-treatment based on the nature of the subsequent oxidation study.

3.2.2.1. Conventional heat treatment

To understand the effect of alloying elements and microstructures (grain boundaries and carbides) on cyclic oxidation behaviour, the as-received ingot form of IN738LC, Rene 80 and N5 Ni-based superalloys were subjected to solution treatment and ageing heat treatment. These are summarized in Table 3-3.

Table 3-3. Solution treatment and ageing heat treatment conditions used for the candidates (RT: Room temperature, AC: Air-cooling, FC: Furnace cooling).

Alloy	Solution treatment	Ageing heat treatment
IN738LC	1120°C for 2 hours and cooled to RT using AC	845°C for 24 hours and FC to RT
Rene 80	1204°C for 2 hours and cooled to RT using AC	1052°C for 4 hours and then 843°C for 16 hours followed by FC to RT
N5	1289°C for 2 hours and cooled to RT using AC	1079°C for 4 hours and then 899°C for 16 hours followed by FC to RT

3.2.2.2. Continuous cooling heat treatment

The equilibrium weight fractions of γ, γ' and liquid phase for IN738LC were obtained over the range 700°C to 1400°C using the thermodynamic simulation JMatPro^{R} version 4 software [224], which is shown in Figure 3-1. From Figure 3-1, the γ' solvus temperature for this alloy is approximately 1134°C. The standard solution heat treatment temperature for this alloy is 1120°C [225], which is below the predicted γ' solvus temperature; this temperature is termed as the partial solution treatment temperature.

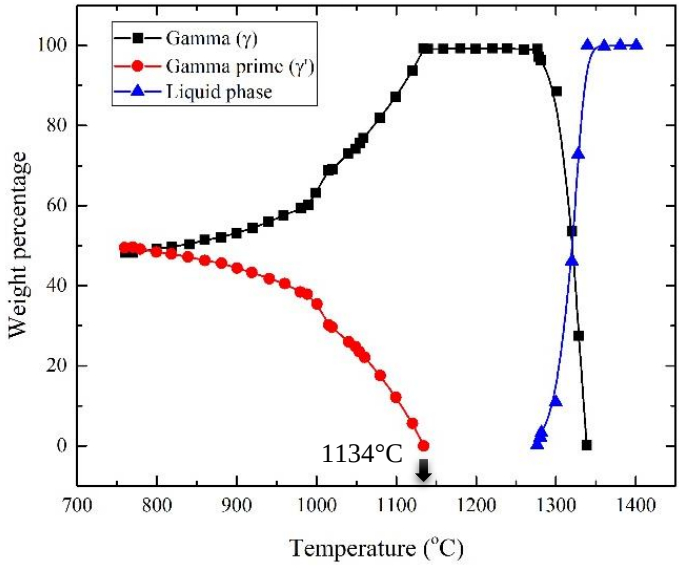

Figure 3-1. Equilibrium weight fractions of phases as a function of temperature from JMatPro.

In order to investigate the effect of γ' precipitate size on the oxidation behaviour of a Ni-based superalloy, different monomodal γ' precipitate size distributions were produced using a continuous cooling heat treatment procedure. To prove the concept of influence of γ' precipitate size on oxidation behaviour, only one alloy was selected out of the three alloys, i.e., IN738LC.

For this purpose, EDM cut blank samples were used to produce different precipitate sizes using different cooling rates. All cooling tests were performed in a Carbolite box furnace, CWF-

1300, in static air and a γ' solutionizing temperature of 1200°C was used (supersolvus temperature). Specimens were held at 1200°C for up to 10 minutes and then cooled to 800°C at different cooling rates. On reaching 800°C, specimens were rapidly quenched by immersing in water. The primary objective of this experiment was to produce a mono-modal precipitate size distribution by avoiding the second and third burst of nucleation below 800°C. Four different cooling rates were obtained (from 1200-800°C) by water quenching, air cooling and furnace programming; these gave cooling rates of 3000, 50, 5 and 2.5°C/min respectively.

3.2.3. Polishing, dimensioning and weighing

The heat-treatment conditioned samples were polished from 180- to 1200-grit on silicon carbide paper and subsequently rinsed with distilled water, de-greased and then ultrasonicated using methanol. After surface preparation, the sample dimensions (11 mm x 9 mm x 3 mm = 3.18 cm^2) were measured to a precision of ± 0.01mm using a digital vernier calliper to evaluate the surface area. Finally, the weight of each sample, as well as the weight of the glazed porcelain crucible containers, were measured using a micro-balance with an accuracy of 0.0001 mg.

3.3. Oxidation

The type of exposure at elevated temperature in ambient air was selected based on the objective of this research. First, cyclic oxidation at high-temperature was conducted to understand the effect of alloying elements, microstructure and scale spallation behaviour during thermal cycling. Second, to prove the concept that oxidation/corrosion kinetics, scale thickness and internal oxidation zone thickness depended upon γ' precipitate size, alloy IN738 was subjected to isothermal and cyclic oxidation at various temperatures as well as to aqueous corrosion.

3.3.1. Cyclic oxidation

Each cyclic oxidation test (one test for each of the three alloys studied) was conducted using an automated cyclic oxidation apparatus, which was built in-house. A schematic of the apparatus is shown in Figure 3-2. The setup consisted of a vertical alumina tubular furnace (70 mm inner dianmeter), with three stages of sample trays that could accommodate a total of 21 samples per batch (7 samples in each tray). The furnace consisted of three stages of controlled heating zones surrounded by insulation, each capable of independent operation via an external controller. The temperature at the top of the furnace remained cool (to help samples maintain close to ambient temperature when they are raised) throughout experimentation using copper coils connected to a constantly flowing and pressurized cold water supply. The trays were automatically raised and lowered using a pneumatic actuator, controlled by a timer-operated solenoid valve using an Arduino Uno controller.

Each thermal cycle consisted of (1) heating from ambient temperature to 900˚C in 1 min (2) isothermal exposure at 900˚C for 60 min and (3) cooling close to ambient temperature for 10 min. Thus, every cycle took a minimum of 70 min to complete including both heating and cooling; a total of 1000 cycles (1116 h) was used for each alloy composition. The heating and cooling rates were found to be 25˚C/s and 5˚C/s respectively. The thermal cycles used for the present work are illustrated in Figure 3-3. A series of samples of the same alloy was periodically removed one by one from the furnace at pre-defined time intervals/cycles to monitor mass change measurements and microstructural evolution. For each alloy, 21 samples were used for one batch of tests. Two tests were conducted for each alloy to check for consistency in mass change measurement and scale spallation.

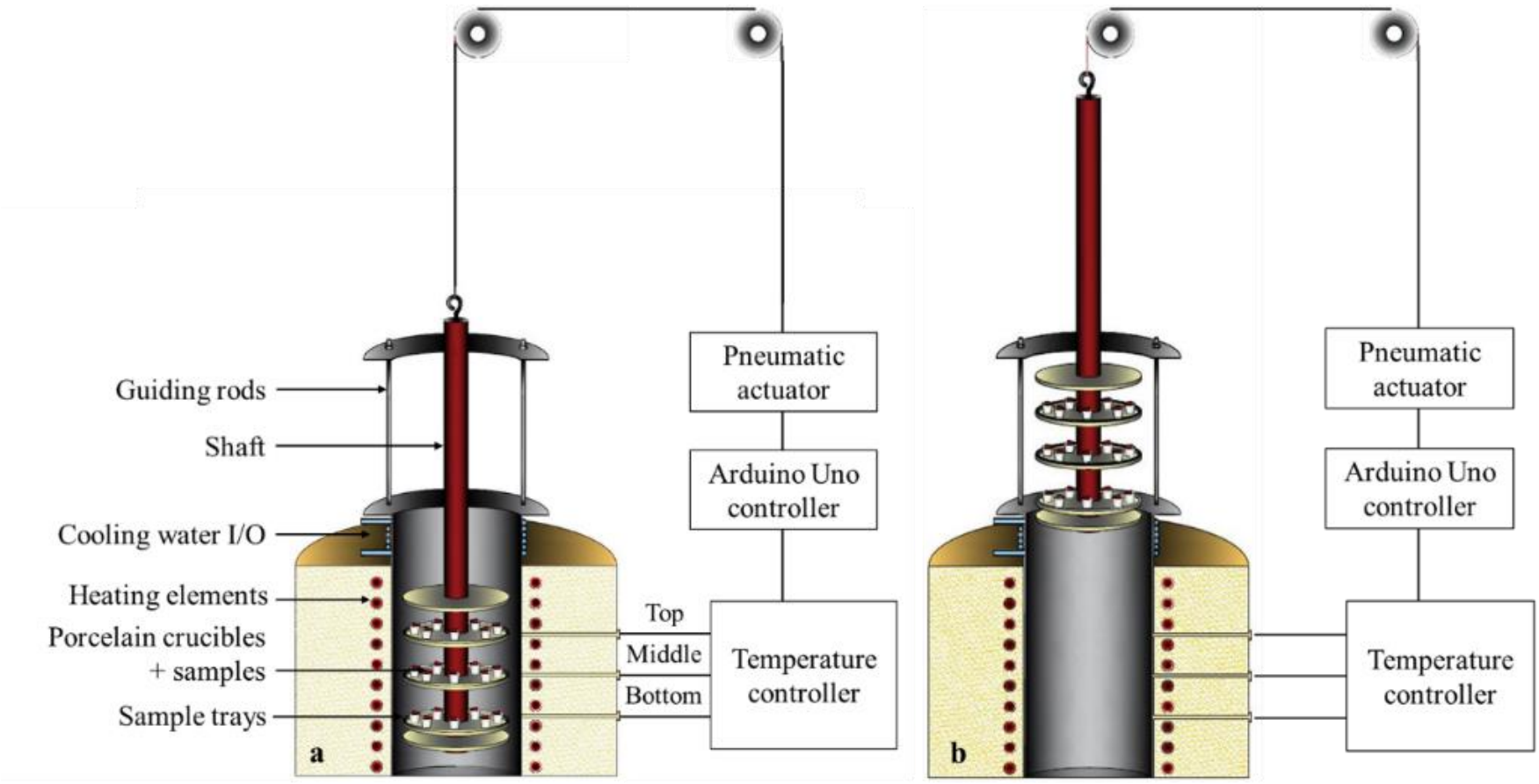

Figure 3-2. Schematic of in-house built vertical tube cyclic oxidation furnace. a) specimens at 900˚C and b) specimens at ambient temperature

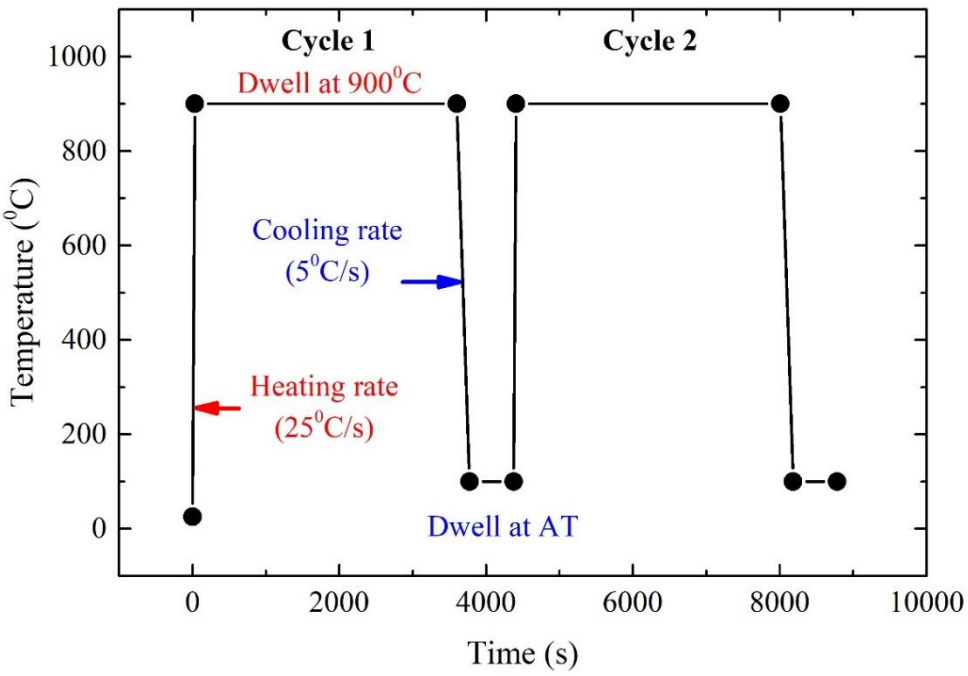

Figure 3-3. Heating and cooling rates measured using the in-house built cyclic oxidation setup.

3.3.2. Isothermal oxidation

In order to study the effect of γ' intermetallic size on isothermal oxidation behaviour, the polycrystalline IN738LC superalloy was oxidized in ambient air at 900°C for various time intervals for up to 1000h in a Carbolite high-temperature box furnace, CWF-1300 (max: 1250°C). The furnace was calibrated using an external thermocouple before the tests. The size of the hot zone was confirmed by taking calibrated temperature readings in four corners and the centre. The samples were withdrawn at different intervals of time and left to cool in laboratory air. Once cooled, each sample was weighed at least three times after the oxidation tests using an analytical balance, and the mean mass gains and standard deviations were calculated. In order to ensure the accuracy of the measurements, the balance was allowed to stabilize before taking the readings.

3.3.3. Electrochemical tests

The effect of γ' size on corrosion behaviour was also studied using aqeuous corrosion tests at room tempearture. Different γ'-sized monomodal IN738LC specimens produced from the different cooling rate experiments were mounted in bakelite and polished to 1 μm using diamond paste. These specimens were used as working electrodes with a surface area of 1 cm^2 in contact with the electrolyte. The tests were conducted in a three-electrode electrochemical cell using a saturated calomel electrode (SCE) as a reference electrode and graphite rods as the counter electrodes as shown in Figure 3-4. Electrochemical tests were conducted in different electrolytes, both acidic and chloride-containing solutions, to simulate different types of exposure conditions; the electrolytes used were 0.1M sulfuric acid (H_2SO_4), 0.5M sodium chloride (NaCl) and 0.5M hydrochloric acid (HCl).

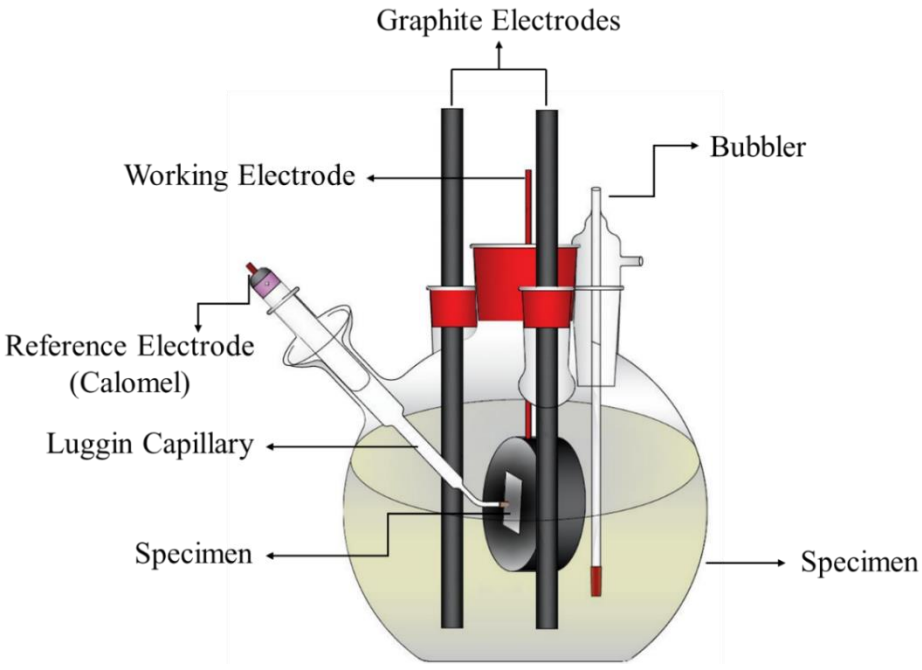

Figure 3-4. Three-electrode electrochemical cell.

During an experiment, the test specimens were subjected to potentiodynamic polarization testing scanned at a rate of 1 mV/s from -1 V to 1.5 V (SCE). A stable corrosion potential was achieved by running an open circuit potential for one hour before the electrochemical test. The polarization and current measurements were performed with a Princeton Applied Research Potentiostat and the potential and current were recorded on a VersaSat3 software. The results from these experiments were used to analyse corrosion current density (i_{corr}), corrosion potential (E_{corr}), passive current density (i_{pass}), critical current density (i_{crit}) and passivation potential range (ΔE_{pass}). All tests were conducted at room temperature. The corroded samples were examined using an optical microscope to evaluate evidence of pitting.

3.4. Microstructural Characterization

3.4.1. X-ray diffraction (XRD)

A Bruker D8 advance XRD instrument with LynxEye PSD was used to identify the oxide scale phases formed on the surface of the samples at various intervals. The analysis was done using a standard Copper K_α radiation ($\lambda = 0.15406$ nm) in the Bragg-Brentano configuration operated at 40 kV/40 mA, with a Ni-filter to suppress the spectral line K_β. The measurement at RT was conducted over the 2θ range of 20˚ - 70˚ with a scan rate of 1.5 seconds/step. The peaks in the diffraction patterns were identified by matching with known standard patterns, using JADE software basic evaluation search ad match program.

3.4.2. Cold mounting and polishing procedures

Once the surface oxide phases were determined using XRD, to retain the edge and to overcome abrasion problems the samples were mounted in cold-setting epoxy resin on the longitudinal axis. The mounts were allowed to set for 15 h and then subjected to grinding and polishing procedures. Briefly, the mounted samples were ground from 180 to 1200 grit on SiC paper and then polished with 6 μm followed by 1 μm diamond suspension on polishing cloths. In order to remove the polishing residues, samples were cleaned thoroughly in an ultrasonic bath with methanol and dried.

3.4.3. Etching for alloy microstructural characterization

In order to obtain a clear threshold between matrix, precipitates and oxide scale, etching was performed. The optimum etching solution for IN738, Rene 80 and N5 was found to be 12ml of 70% H_3PO_4 + 40ml of 70% HNO_3 + 48ml of 98% H_2SO_4.

3.4.4. Optical microscopy

Optical microscopy had limited use in this study as the oxide scale thickness was not resolvable with the maximum magnification of 1000x offered by an optical microscope. It was mainly used for general aspects of checking an oxidized surface or the quality a polish. The microscope used was a ZEISS–Aziovert 25 with a digital camera attached to it for image acquisition.

3.4.5. Scanning electron microscopy (SEM) / EDS analysis

The microstructure and morphology of the as-polished and oxidized specimens were examined with a scanning electron microscope JEOL JSM-5900LV and an in-lens detector fitted high-resolution FEI Nova Nano SEM 450 with a field emission gun at the Manitoba Institute for Materials (MIM). The images were taken in the secondary electron (SE) mode for topography and backscattered electron (BSE) for phase contrast. The working distance (WD) was between 10 - 14 mm and an accelerating voltage of 12 kV (to ensure that excessive over-voltages did not lead to charging) was used during imaging. Spot, line and overall compositional analyses were conducted with an Oxford INCA energy dispersive X-ray spectroscopy (EDS) detector attached to the JEOL-SEM and the results were averaged from at least five different readings. The accelerating voltage was increased to 20 kV during the EDS analysis in order to increase the count rate. The acquisition time for the composition analysis was fixed at 60sec and the dead time was adjusted between 20-30%. Prior to examinations, the specimens were carbon-coated to reduce the effect of charging by improving the conductivity of the oxide scale.

3.4.6. Transmission electron microscopy

To study the effect of cooling rate on the composition of γ' precipitates and to understand the subsequent effect of these on corrosion and oxidation, the samples were subjected to transmission electron microscopy (TEM) analyses. Thin transparent foils for TEM imaging were cut from the samples cooled using different cooling rates and ground to a thickness of <100 μm using standard metallographic methods. Conventional TEM samples were made from discs of 3 mm diameter punched out of 100 μm thickness sheet. These discs were subjected to dimpling on a Gatan Dimple

Grinder™ using 1 μm diamond paste to attain a dimpled region thickness of <50 μm to minimise the time required for the final stage of electron transparency. The samples were subsequently electropolished using a Tenupol twin-jet electropolisher with 10% perchloric acid in 90% methanol at -40°C and 1 V. TEM and scanning/transmission electron microscope (STEM) imaging were performed using an FEI Talos F200X at an accelerating voltage of 200kv, at MIM. A single tilt sample holder was used in this study as diffraction analyses were not required. The compositional analysis was done using a Super - X EDS system.

3.4.7. Electron backscattered diffraction (EBSD)

To study the grain orientation of all three alloys, the samples were ground to 1200 SiC grit and subsequently polished to 1 μm diamond. Finally, to develop a strain free and flat surface for EBSD measurement, samples were polished using a vibratory polisher for 48 h. These samples were ultrasonically cleaned using acetone for 15 min, then washed with ethanol and dried in flowing air. Grain orientations were characterized using a FEI Nova NanoSEM 450 equipped with Oxford EBSD system at a voltage of 20 kV. The EBSD maps were recorded with a step size of 3 μm.

Chapter 4 Results

4.1. Microstructure of the heat-treated specimens

The candidate alloys were subjected to microstructural investigation prior to cyclic oxidation to understand the effect of microstructure on their subsequent oxidation behaviour. Based on an SEM investigation, the IN738LC contained MC and $M_{23}C_6$ carbides along the grain boundaries and gamma-gamma prime (γ-γ') eutectic phases within the interdendritic regions, all within the Ni-rich gamma (γ) matrix. The IN738LC exhibited a bi-modal precipitate size distributions of primary γ' (~1μm) and secondary γ' (~150 nm). The strength of the alloy depends on the volume fraction of the precipitates (58%), precipitate size distribution and lattice mismatch between γ and γ'. The IN738LC has a serrated grain boundary structure with the sizes varying from 1-3 mm. The SEM microstructure and grain mapping of the IN738LC are shown in Figure 4-1a.

The SEM microstructure of the second generation, single crystal alloy, N5 is shown in Figure 4-1b. The alloy has a γ/γ' microstructure and contains a high volume fraction of monomodal γ' (>60 %) precipitates with the average size of 0.5 μm homogeneously distributed in the γ matrix. The N5 has a dendritic microstructure with eutectic phase. The dendritic regions were enriched in Re and W and depleted in Ta and Al. The Ta and Hf segregated to the eutectic phase as carbides.

The microstructure of the directionally-solidified (DS) Rene 80 is shown in Figure 4-1c. The alloy consists of ~ 70 % volume fraction of uniformly sized cuboidal γ' precipitates with sizes varying from 0.3-0.5 μm in an austenitic, γ matrix. The alloy contains 0.2 wt. % carbon in the form of blocky MC carbides (M = Ti, W and Mo). These carbides occur within the grains and along the grain boundaries and measure ~20 μm in size. Some of these carbides also dissociate at an ageing temperature (843°C for 16 h) to form discrete $M_{23}C_6$ (M=Cr) grain boundary carbides [226].

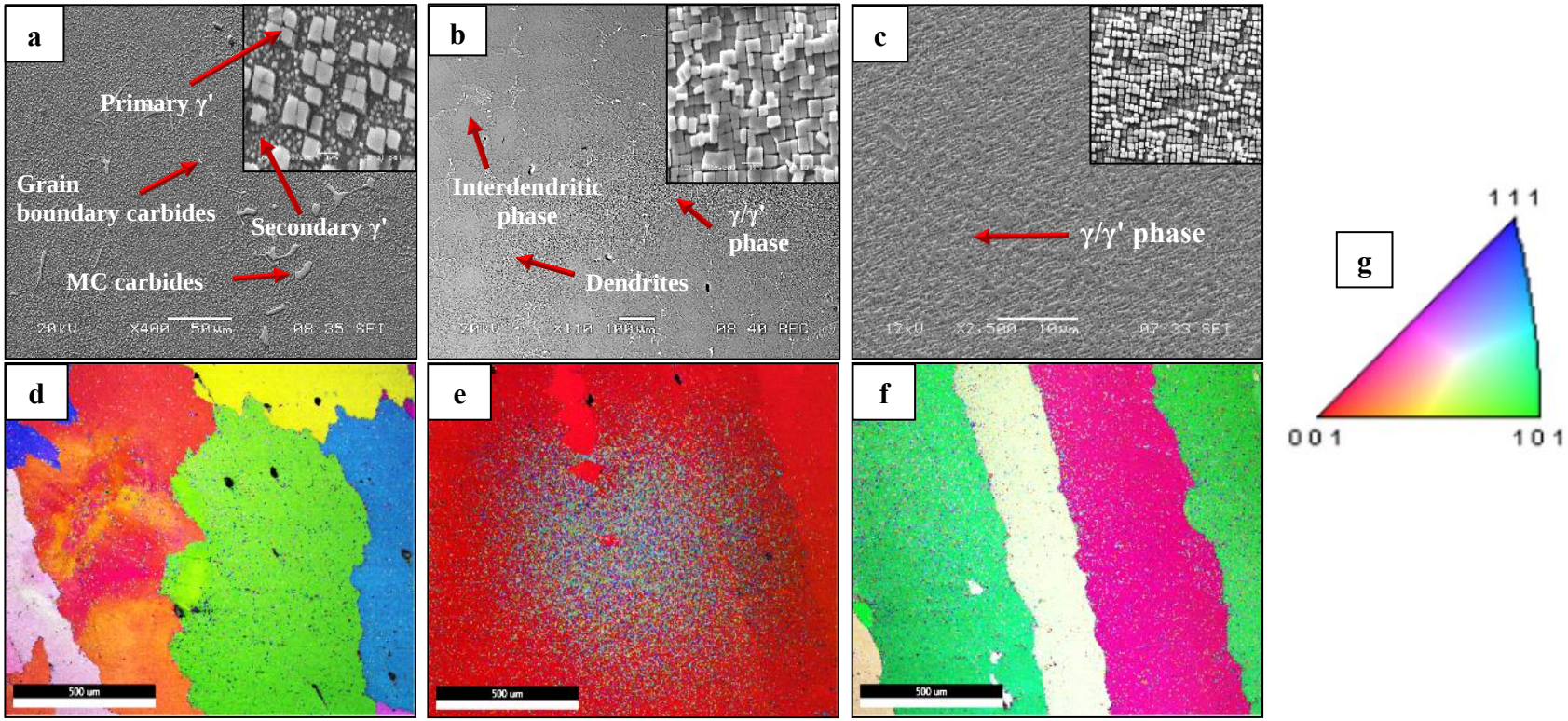

Figure 4-1. Initial SEM microstructures of all three Ni-based superalloys a) polycrystalline IN738LC, b) directionally solidified Rene 80 and c) single crystal N5 and corresponding grain mapping in d), e) and f) with planar mapping in g).

The samples were subjected to electron backscattered diffraction (EBSD) analysis to identify the crystallinity of the samples and the results are shown in Figure 4-1d, 2e and 2f for IN738LC, Rene 80 and N5 respectively. The representative planes are given to the right side of Figure 4-1g.

4.2. Kinetics of cyclic oxidation

Each of the commercial alloys studied was cyclically oxidized in air for up to 1000 cycles (1116 h) at 900°C in order to understand the effect of alloying elements and microstructure on cyclic oxidation performance. The specific mass change per unit surface area of the IN738LC, Rene 80 and N5 as a function of oxidation cycles ($\Delta W/A$ vs N) is shown in Figure 4-2. Because the experiments were duplicated, the plot represents the average of the replicate experiments. IN738LC and Rene 80 showed positive mass change for up to 300 cycles and 500 cycles respectively, followed by a linear decrease into the negative slope region. The mass loss exhibited in these alloys is believed to be due to oxide scale spallation. The Rene 80 degradation was severe, approximately ten times more mass loss after 700 cycles than that of IN738LC under the same conditions. However, the single crystal N5 maintained a positive mass change for the entire 1000 cycles and followed a general parabolic oxidation behaviour with minimum scale spallation and rejuvenation. This parabolic behaviour is more readily seen later in Figure 4-4C.

The N5 alloy exhibited a maximum mass gain of 0.42 mg cm^{-2}; this might be due to the formation of a thin and slow growing oxide scale on the surface of N5. Corresponding values for IN738 and Rene 80 prior to spallation were 1.65 mg cm^{-2} and 1.63 mg cm^{-2} respectively. To understand the effect of cyclic oxidation on all three alloys for up to 300 cycles, parabolic rate constants, k_p were calculated by plotting the square of mass change as a function of cycles

$((\Delta W/A)^2$ vs N) as shown in Figure 4-3. The calculated parabolic rate constant, k_p values for all three alloys are summarized in Table 4-1; again the parabolic nature of the plots is more readily seen in Figure 4-4C.

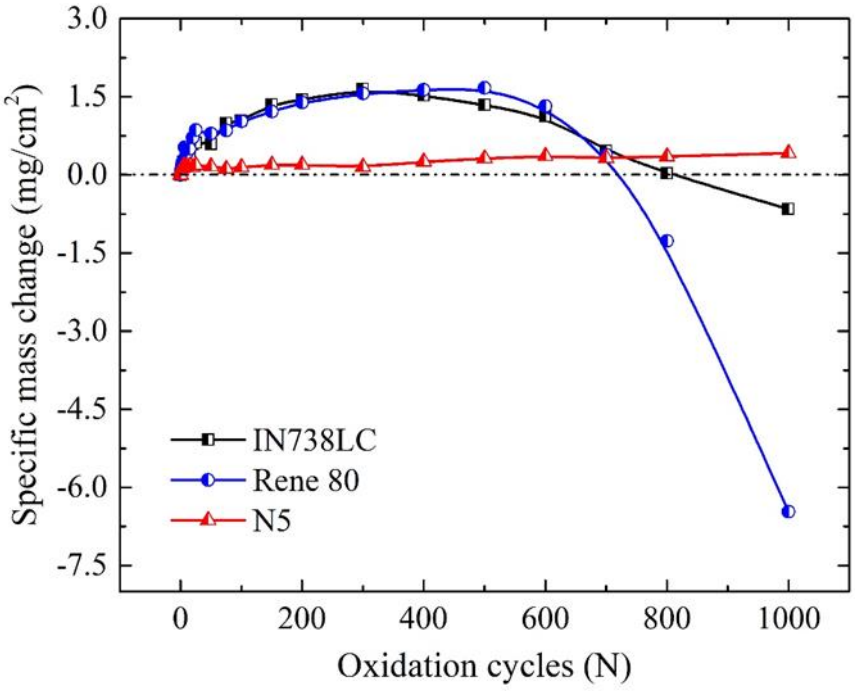

Figure 4-2. Specific mass change of IN738LC, Rene 80 and N5 as a function of oxidation cycles for up to 1000 cycles.

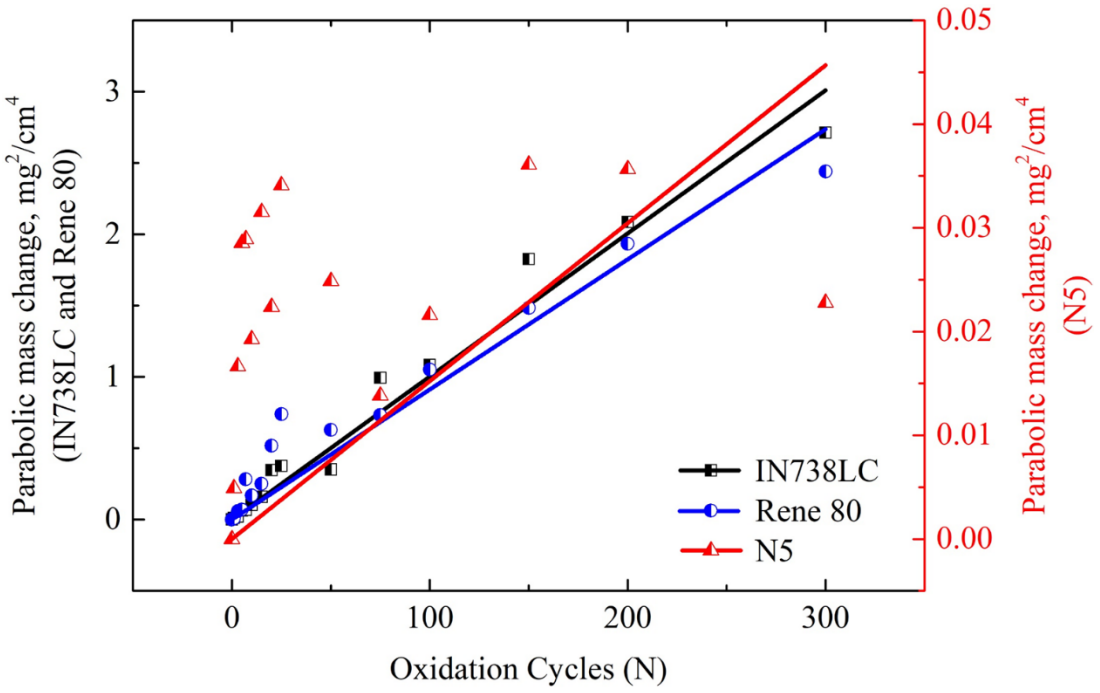

Figure 4-3. Parabolic mass change plots for the three Ni-based superalloys as a function of oxidation cycles (for the first 300 cycles).

Table 4-1. Calculated parabolic rate constants, kp for the three alloys for up to 300 cycles.

Alloy	Parabolic rate constant, k_p ($mg^2\ cm^{-4}\ s^{-1}$)
	Up to 300 cycles
IN738LC	9.71E-03
Rene 80	8.20E-03
N5	3.93E-05

4.3. COSP Modelling

To understand cyclic oxidation kinetics, the experimental cyclic oxidation results for the three alloys were compared using the cyclic oxidation spallation program (COSP) developed by NASA-[195]. The COSP-Monte Carlo model tracks the mass of oxide scale which grows and spalls in each cycle. For cyclic oxidation, a spallation constant, Q_0, of 0.000101 was determined for IN738LC and 0.00015 for N5 by matching the experimental cyclic oxidation kinetics curves with the best fitted cyclic oxidation kinetics curves obtained by COSP; this is shown in Figure 4-4. The parabolic oxide scale growth type was then used to determine the rate constant and spallation constant for both IN738LC and N5, Figure 4-4a and c respectively. However, for Rene 80, a parabolic oxide growth rate could not be fitted; hence, a power law growth type was used and the spall constant was found to be 0.0001 with the power, m of 1.35. From Figure 4-4b, it is seen that the COSP-Monte Carlo fitted kinetics curve deviated from the experimental curve for Rene 80 after 700 cycles.

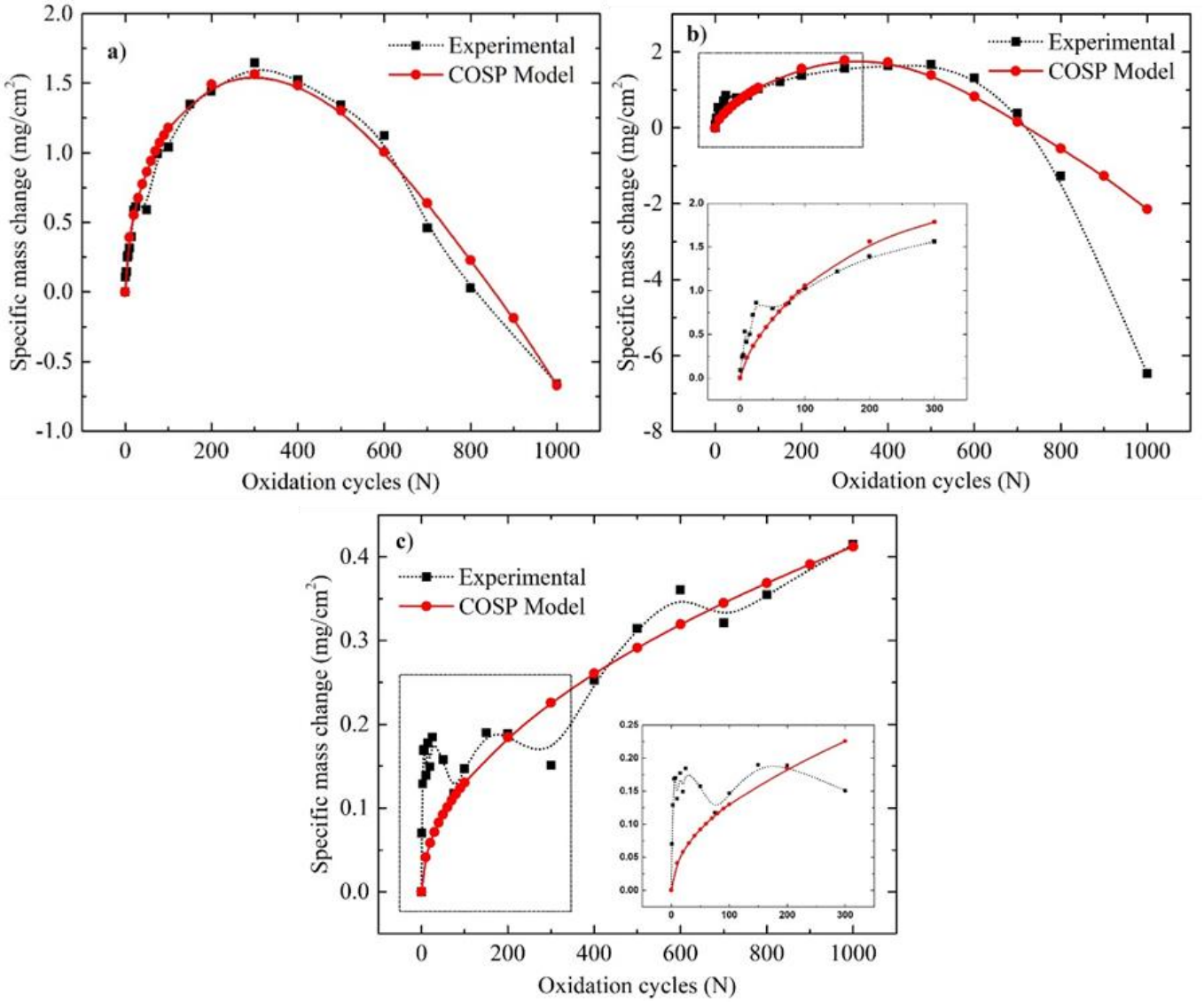

Figure 4-4. Fitting of cyclic oxidation kinetics after 1000 cycles using the COSP- Monte Carlo model a) IN738LC, b) Rene 80 and c) N5.

Although the scale spallation constant value of N5 was higher than that of IN738LC and Rene 80, the difference is considered to be negligible due to less mass change. The parabolic rate constants and the scale spallation constants for all three alloys are summarised in Table 4-2.

Table 4-2. COSP-Monte Carlo model results for IN738LC, Rene 80 and N5 after 1000 cycles.

Parameters	IN738LC	Rene 80	N5
Oxide scale	Cr_2O_3	Cr_2O_3	Al_2O_3
Stoichiometric constant	3.1666	3.1666	2.1243
Type of oxide growth	Parabolic law	Power law (m=1.35)	Parabolic law
Rate constant	$k_p=1.62x10^{-2}$ ($mg^2\ cm^{-4}\ s^{-1}$)	$k=1.12x10^{-2}$ ($mg^{1.35}\ cm^{-2.55}\ s^{-1}$)	$k_p=2.3x10^{-4}$ ($mg^2\ cm^{-4}\ s^{-1}$)
Spall constant, Q_o	0.000101	0.0001	0.00015

4.4. X-ray Diffraction

The oxides formed on the surface of the three superalloys were subjected to standard XRD to identify the oxide phases. The primary oxides formed on the surface of IN738LC at the initial stages of oxidation were Cr_2O_3, TiO_2 (rutile) and $Ni(Cr, Al)_2O_4$ spinel but no traces of NiO were found for the entire 1000 cycles. The intensities for each oxide increased with an increase in the number of oxidation cycles. Additionally, MoO_3 and $NiMoO_4$ phases were identified on the surface of Rene 80, whereas N5 showed an external Al_2O_3 layer. The XRD peaks for the alloys taken at different intervals of cyclic oxidation for up to 1000 cycles are shown in Figure 4-5 and the oxide phases determined for all three superalloys are summarized in Table 4-3. The oxide peak intensities varied for different time intervals due to scale spallation and the associated subsurface exposure. The oxide phases found also agree with those reported by other researchers on the same alloys [13], [223], [227], [228].

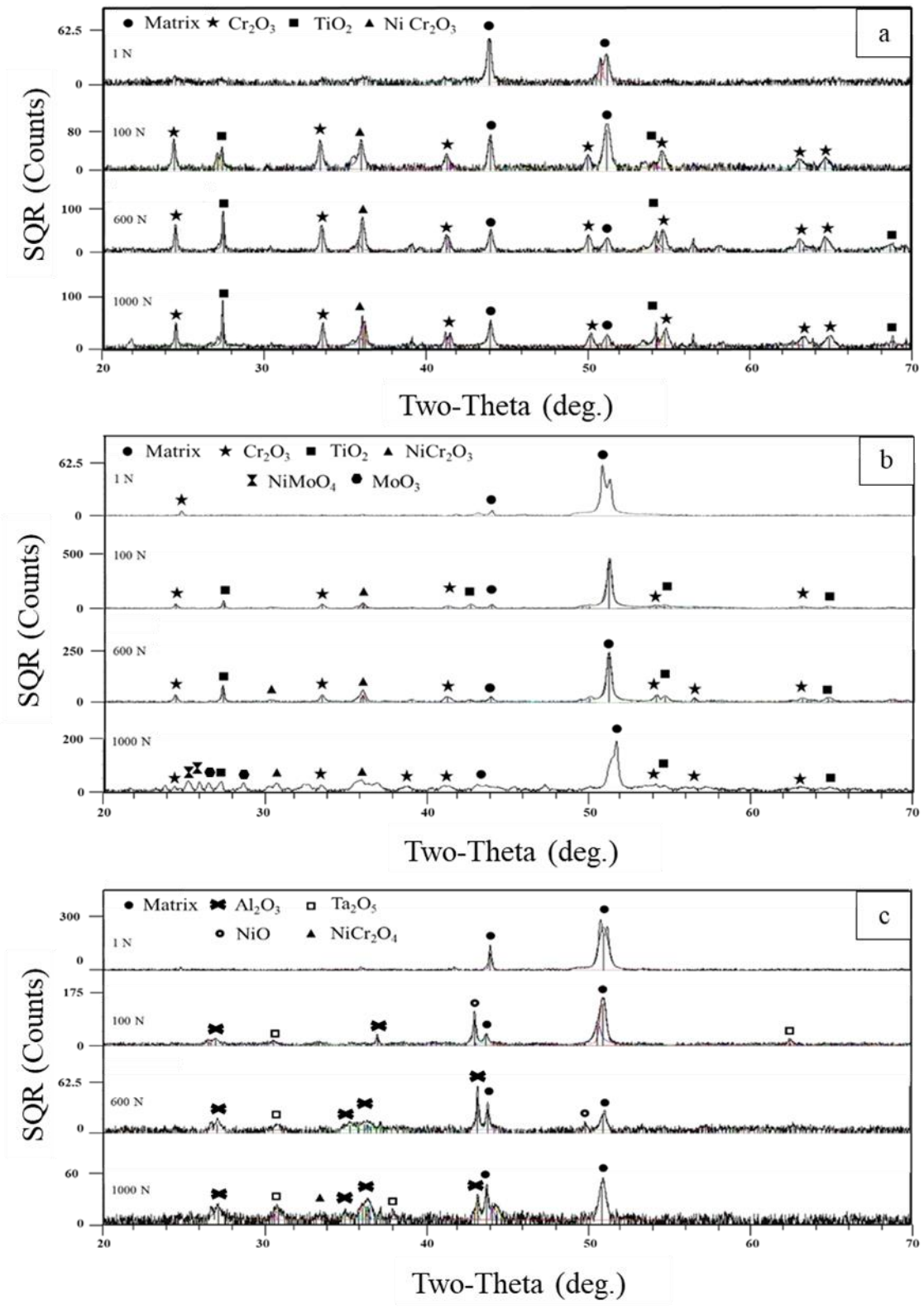

Figure 4-5. XRD spectra from the surfaces of the cyclically oxidized superalloys after 1, 100, 600 and 1000 cycles a) IN738LC, b) Rene 80 and c) N5.

Table 4-3. XRD analysis of oxide scale phases formed on IN738LC, Rene 80 and N5 from 1-1000 oxidation cycles.

Alloy	Phases identified	Alloy	Phases identified	Alloy	Phases identified
IN738LC	TiO_2 Cr_2O_3 Ni $(Cr,Al)_2O_4$ $CrTi_2O_5$	Rene 80	TiO_2 Cr_2O_3 Ni $(Cr,Al)_2O_4$ $CrTi_2O_5$ $NiMoO_4$ MoO_3	N5	NiO $Ni(Cr,Al)_2O_4$ Al_2O_3 Ta_2O_5

4.5. SEM scale morphology and characterization - surface analysis

4.5.1. Surface analysis of IN738LC

Both the oxide scale composition and morphology changed significantly with an increase in cyclic oxidation duration. The specimen exposed for one cycle exhibited a discontinuous oxide layer on the surface with three distinct regions; one with no sign of oxide formation, one showing strong peaks of Cr, Ni, O along with a detectable amount of Al, presumably corresponding to $Ni(Cr,Al)_2O_4$ spinels and finally a Cr-rich oxide layer along the grain boundaries. The longer oxidation cycles led to the formation of continuous layers of $NiCr_2O_4$, Cr_2O_3 and TiO_2 on the surface and the specimen exposed for up to seven cycles exhibited scale spallation in some areas. Similar scale morphologies and compositions during isothermal oxidation for the same alloy were also reported in an earlier work [26].

The EDS elemental mapping of the delaminated region after seven cycles as shown in Figure 4-6 indicated that the scale spallation occurred at the scale/alloy interface. The bright region (A) of the spalled area was rich in Ni, indicating substrate composition (Figure 4-6f). The darker region (B) was rich in Cr along with a measurable quantity of Ti; both elements were associated with oxygen suggesting Cr_2O_3 and TiO_2 formation. Further exposure led to the formation of multiple and non-uniform oxide layers on the surface due to scale spallation and regrowth.

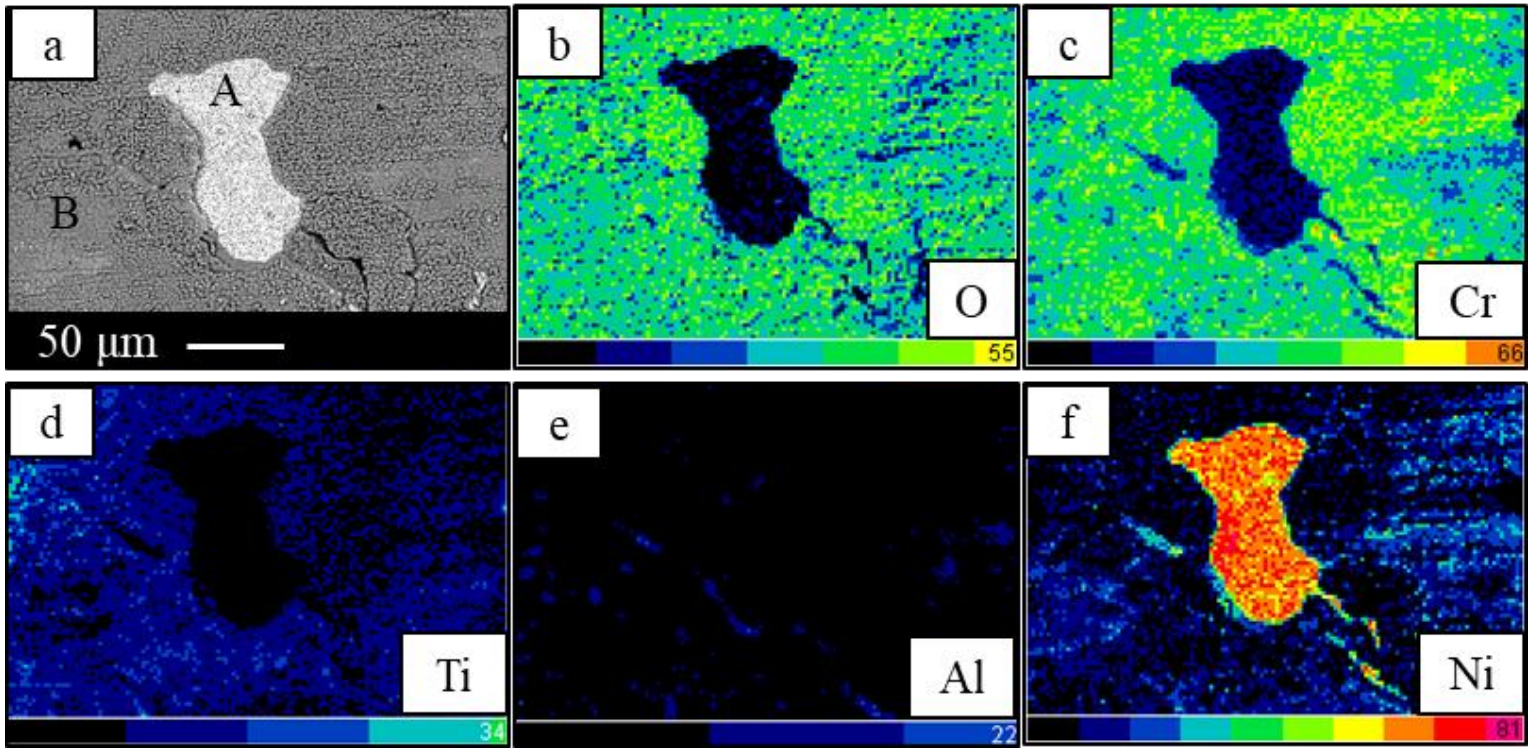

Figure 4-6. SEM elemental mapping of IN738LC scale spallation after seven cycles a) BSE image and b), c), d), e) and f) are O, Cr, Ti, Al and Ni respectively.

The SEM and BSE surface morphologies after 100 and 1000 cycles are shown in Figure 4-7. From Figure 4-7a, the topmost layer consisted of Ti-rich oxide particles and a porous $Ni(Cr,Al)_2O_4$ spinel layer. Most of the scale spallation was observed within the scale, i.e., at the spinel/TiO_2 and Cr_2O_3 interface as shown in Figure 4-7a and Figure 4-7b. The layer below the spalled scale was found to be a dense Cr_2O_3 oxide scale, which is more resistant to scale spallation compared to that of the spinel and TiO_2. From Figure 4-7b, it is seen that the scale spallation network occurred on the entire surface of the specimen as the oxidation cycles increased up to 1000 cycles. However, XRD and EDS surface analysis results did not reveal the presence of an Al_2O_3 layer up to 1000 cycles.

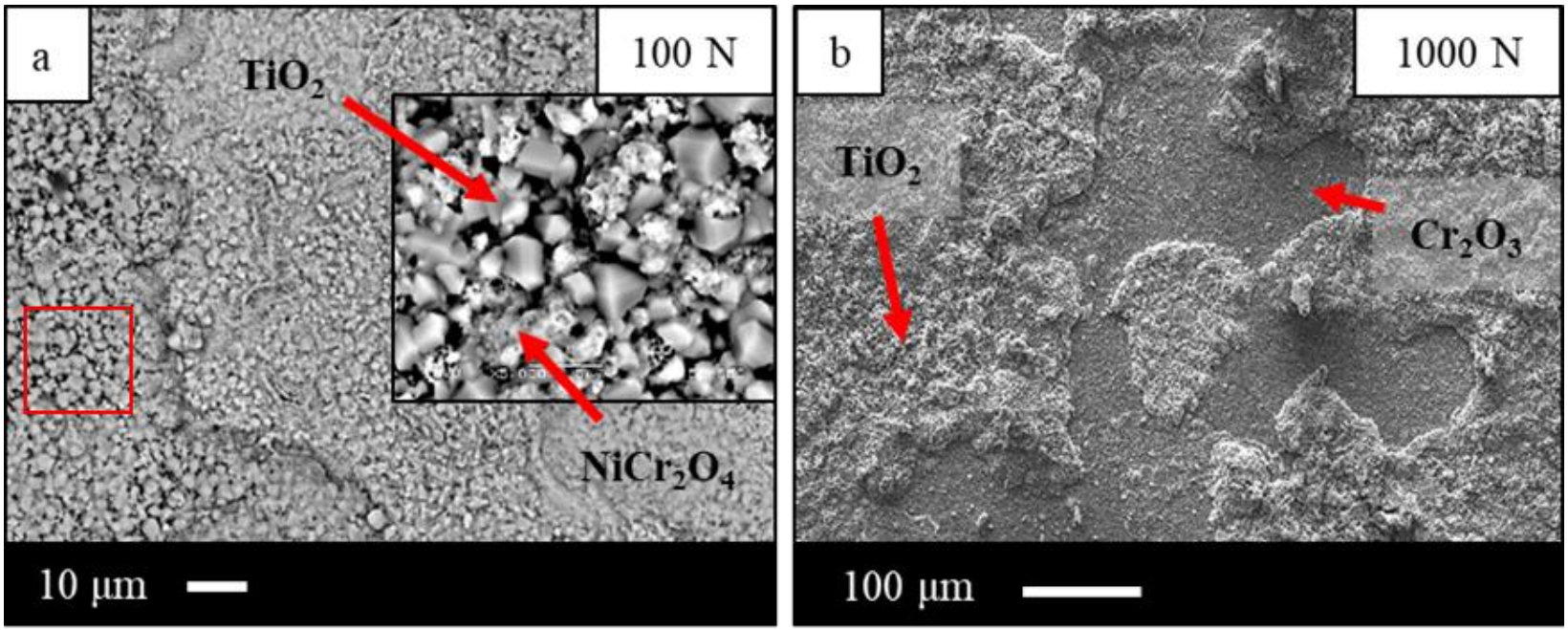

Figure 4-7. SEM- BSE surface morphologies of IN738LC showing scale spallation areas after a) 100 cycles and b) 1000 cycles.

4.5.2. Surface analysis of Rene 80

The Rene 80 samples, after one cycle, exhibited a uniform and transparent oxide layer as shown in Figure 4-8. The corresponding EDS results revealed Ti-, Cr-, Ni- and Al-rich layers associated with oxygen, which were identified as TiO_2, Cr_2O_3 and the transient oxides $NiAl_2O_4$ and $NiCr_2O_4$ from the XRD analysis (Figure 4-5). Scale spallation was also observed in several areas on the surface, exposing the substrate again to the oxidizing atmosphere as shown in Figure 4-8a. Most of this spallation was observed at the scale/alloy interface. The transverse view of a specimen surface after one cycle is shown in Figure 4-8b. Since Rene 80 is a directionally-solidified alloy consisting of columnar grains, exposure of this alloy to cyclic oxidation conditions revealed grain boundary oxidation. The grain boundary oxides were much thicker compared to that of surface oxides suggesting grain boundary oxidation was more rapid relative to that of surface oxidation. The EDS analysis of the darker islands of oxide scale along the grain boundaries in Figure 4-8 revealed Ti- and Cr-rich oxide phases.

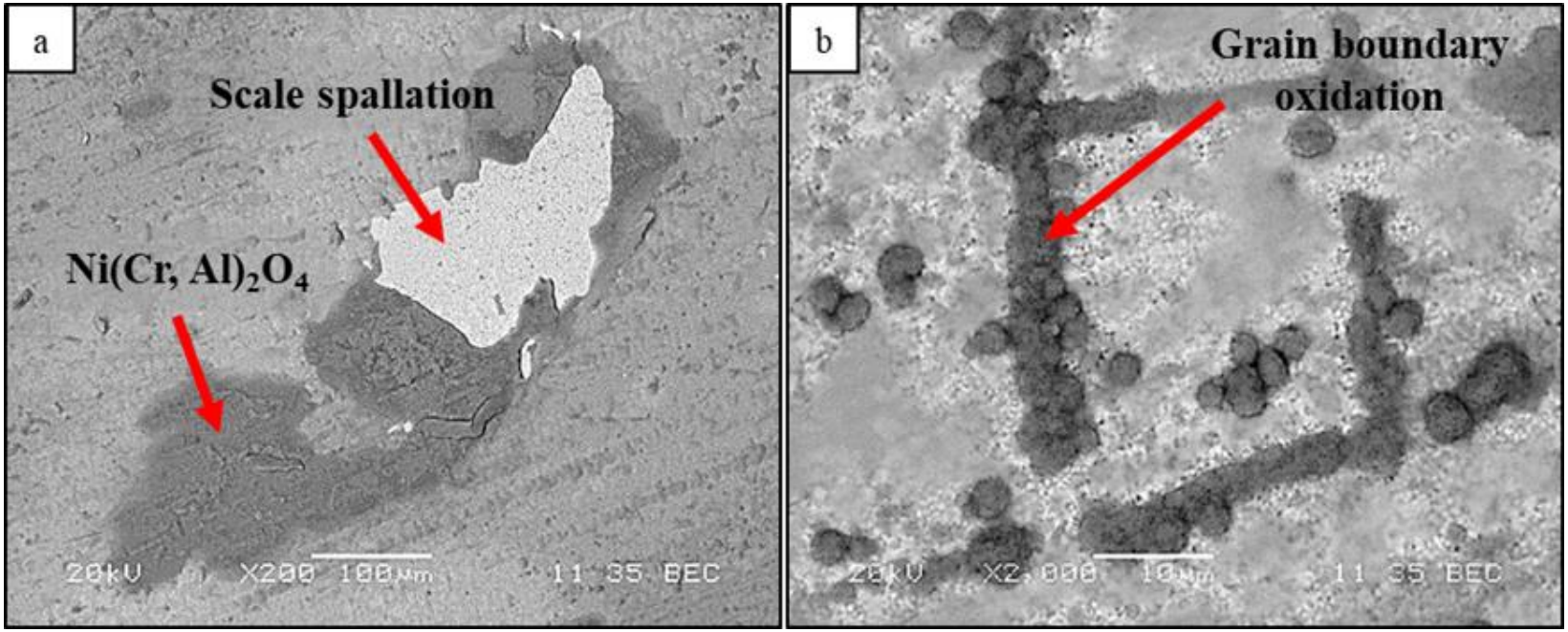

Figure 4-8. SEM- BSE surface morphologies of Rene 80 after one cycle showing a) oxide scale spallation and b) grain boundary oxidation.

Further exposure resulted in the formation of complex oxides similar to those found for IN738LC. The EDS analysis of a specimen surface after five cycles revealed the formation of a Mo-rich oxide layer between the TiO_2 and Cr_2O_3 scales as shown in Figure 4-9a. This phase was identified as MoO_3 and $NiMoO_4$ as shown in the XRD analysis of Figure 4-5b. The respective SEM-backscattered images displayed a significant amount of porosity and cracks within the scale, Figure 4-9b. An increase in oxidation cycles increased the formation of this porous Mo-rich scale on the surface.

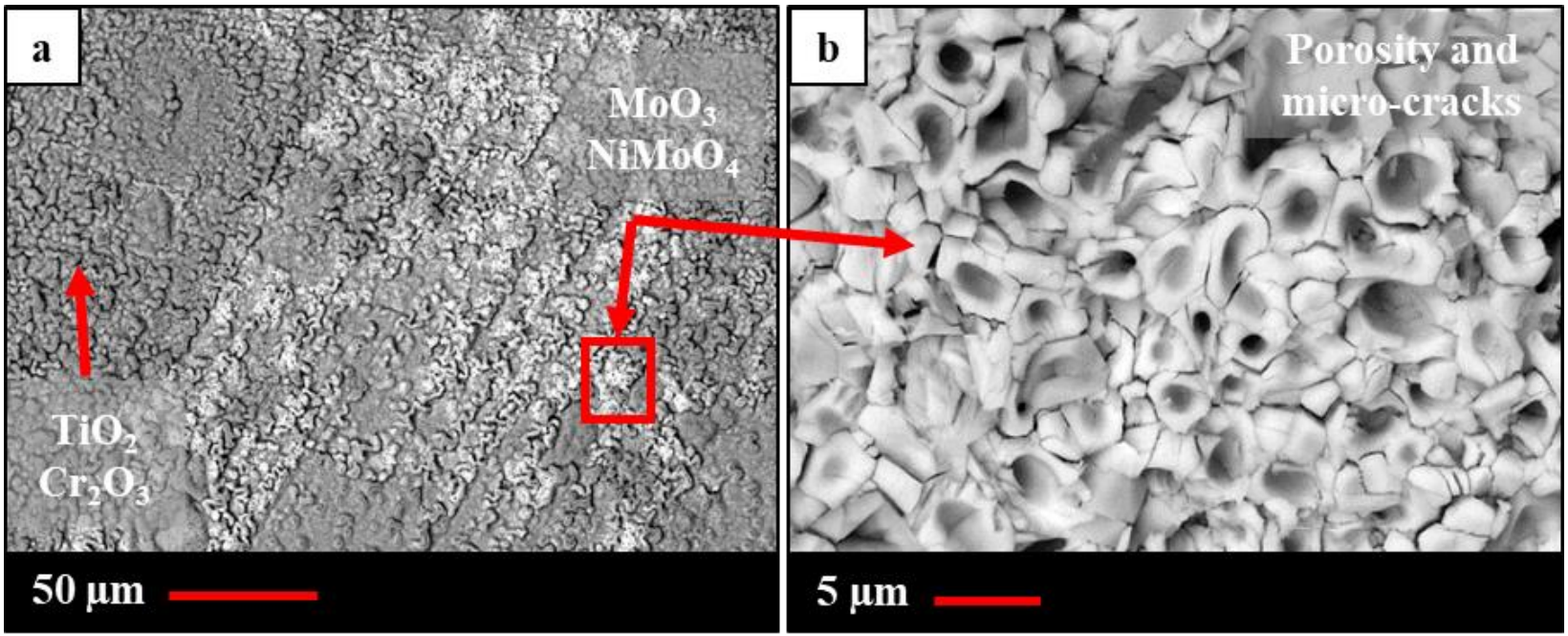

Figure 4-9. SEM- BSE surface morphologies of Rene 80 after five cycles showing a) darker region TiO_2 and Cr_2O_3 scale and Mo-rich scale (bright) and b) magnified view of Mo-rich scale.

The combination of thermal stresses, a porous oxide layer and weak adherence to the substrate led to severe scale spallation after 600 cycles as shown in Figure 4-10a. The scale spallation continued after 600 cycles and led to the significant mass loss, which was shown in the mass change as a function of oxidation cycle curve in Figure 4-4b. The coherency between spalled and oxidation kinetics can be seen by comparing Figure 4-4b and Figure 4-10. This scale spallation resulted in bare matrix material being exposed to the environment as shown in Figure 4-10b. The EDS analysis revealed that the brighter region A is substrate material with discontinuous Al_2O_3 scale; the dense and compact second layer (region B) is Cr_2O_3 and finally, the external layer on the surface of region C is TiO_2.

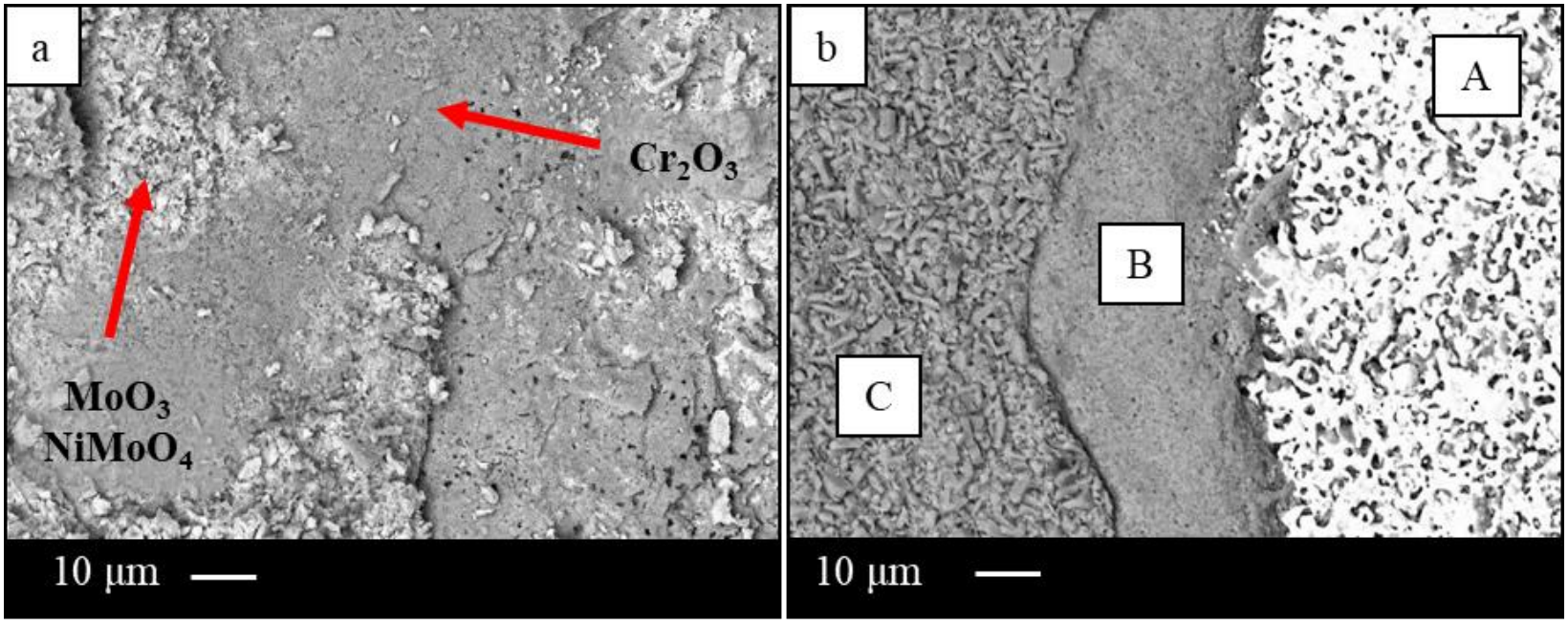

Figure 4-10. SEM- BSE surface morphologies of Rene 80, a) Sizeable Mo-rich oxide scale spallation at oxide/oxide interface after 600 cycles and b) scale spallation at oxide/oxide/substrate interfaces. Region A – substrate with a dark discontinuous network of Al_2O_3; Region B-Cr_2O_3 scale and region C-TiO_2 scale.

4.5.3. Surface analysis of N5

The corresponding microstructure for N5 after one cycle was similar to that of Rene 80 after the same duration. The EDS and XRD analyses indicated the presence of NiO and $NiAl_2O_4$; moderate scale spallation was evident following one cycle. The appearance of the sample surface after 15 cycles was similar to that oxidized after one cycle. A close observation of this sample revealed regions of both moderate and severe spallation; this is shown in Figure 4-11(bright regions).

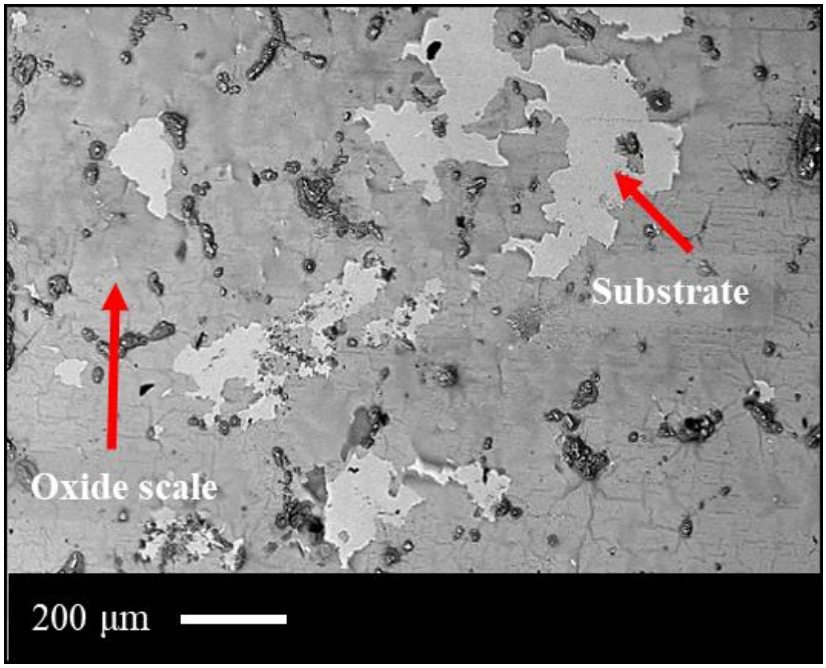

Figure 4-11. SEM- BSE surface morphology of N5 showing scale spallation regions after 15 cycles.

Eutectic regions that were present on the surface were covered predominantly with the oxides of Ta and Hf, imparting a somewhat uneven surface morphology. Since the majority of the surface is not covered with eutectic, Al-rich oxides were identified in both dendritic and interdendritic regions as shown in Figure 4-12a; with further increase in cycles, the majority of the surface was covered by a mixture of Al, Ni and Cr also with a detectable amount of Ta. There was also a subsequent increase in the thickness of the external Al_2O_3 scale. These Al_2O_3 ridges form during early cycles (up to 15 cycles) and will crack and spall off from the surface of the alloy as shown in Figure 4-12a; compositionally the ridges are rich in Ni and Al, suggesting Al_2O_3 and $NiAl_2O_4$. A significant amount of scale spallation was observed in the eutectic region, i.e., around the oxides of TaC and HfC as shown in Figure 4-12b. The oxide scale spallation observed in N5 occurred at the scale/alloy interface due to the presence of a thin and non-adherent $NiAl_2O_4$ scale.

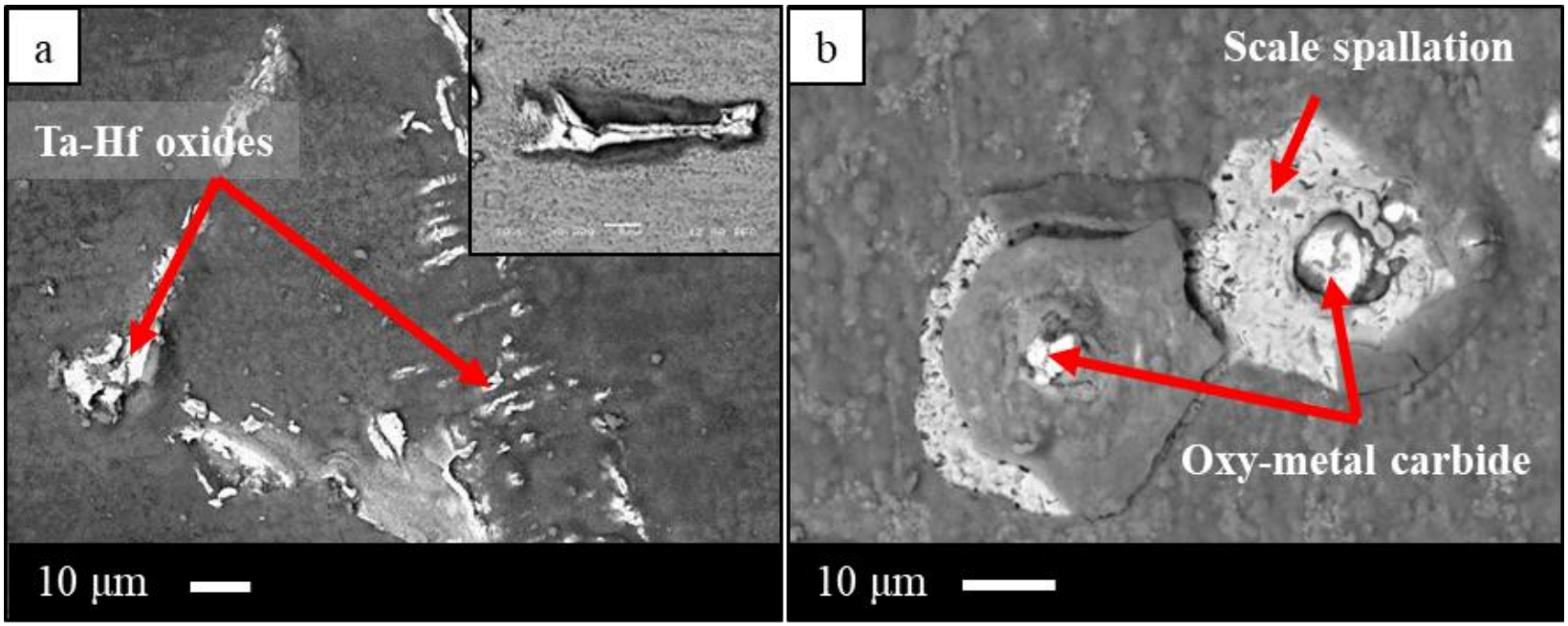

Figure 4-12. SEM backscattered surface morphology of N5 a) oxidation of eutectic region after 15 cycles and b) scale spallation around the oxy-metal carbides in the eutectic region after 50 cycles.

4.6. SEM scale morphology and characterization - cross-sectional analysis

4.6.1. Cross-sectional analysis of IN738LC

The SEM cross-sectional microstructural observations of the oxide layers formed on IN738LC after 1, 100 and 1000 cycles are displayed in Figure 4-13. From Figure 4-13, the alloy showed the formation of both an external oxide scale and internal oxidation attack. The primary external oxide scale after one cycle (Figure 4-13a) was not thick enough to resolve. However, the later cycles suggested the presence of oxides Cr_2O_3, TiO_2, $Ni(Cr, Al)_2O_4$ (Figure 4-13b) and discontinuous finger-like structures of Al_2O_3. The wrinkling and rumpling features of chromia scale extended up to 100 cycles as shown in Figure 4-13b. This type of feature was generally observed in the Al_2O_3 scale, when the scale is relatively thin, typically about 0.5-1.5 μm [185], [229]. Further increase in oxidation cycles initiated cracks in the oxide scale, which later propagated resulting in scale delamination. The adherent part of the oxide scale was mostly small amounts of Cr_2O_3, $NiAl_2O_4$, $TiTaO_4$ and Al_2O_3.

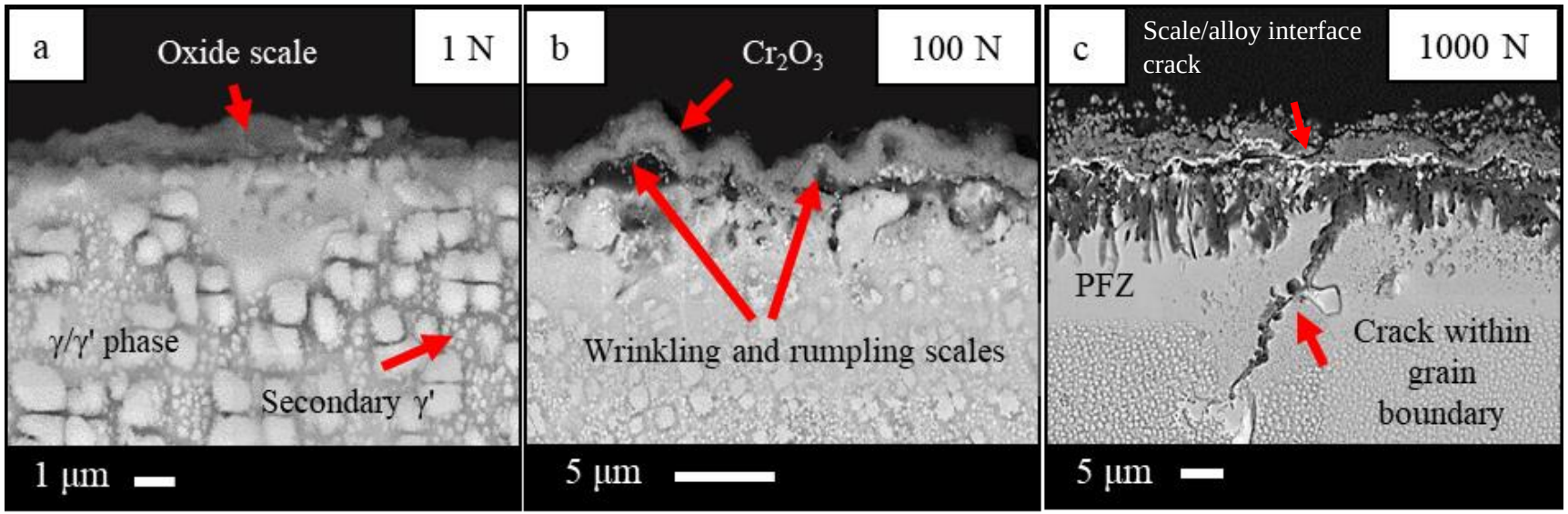

Figure 4-13. SEM-BSE cross-sectional microstructures of IN738LC, a) one cycle b) 100 cycles and c) 1000 cycles.

The morphology and the phases present in the scale varied significantly with increase in cycles due to intergranular oxidation and severe scale spallation; further increase in oxidation cycles resulted in extensive grain boundary oxidation, which led to initiation and propagation of cracks into the substrate. This is evident in Figure 4-13c. From Figure 4-13, the subsurface microstructure also revealed the formation of a precipitate free zone (PFZ), which resulted from selective oxidation of Al from the γ'-precipitates that act as an Al reservoir. A similar mechanism has also been reported in other alumina-forming and chromia-forming alloys by a number of researchers [22], [27]. An increase in cycles increased the dissolution rate of these precipitates making the PFZ much thicker. The thickness of the PFZ was measured to be one micron at the initial oxidation cycle, reaching a maximum of 10 microns after 1000 cycles.

The composition of the oxides at the intergranular region depended on depth in the alloy. From Figure 4-14, EDS elemental mapping of the deep regions of the intergranular oxides was always found to be Ti-rich and as the analysis progressed towards the external Cr_2O_3 scale/alloy interface, the oxides transitioned from Ti-rich to Al-rich.

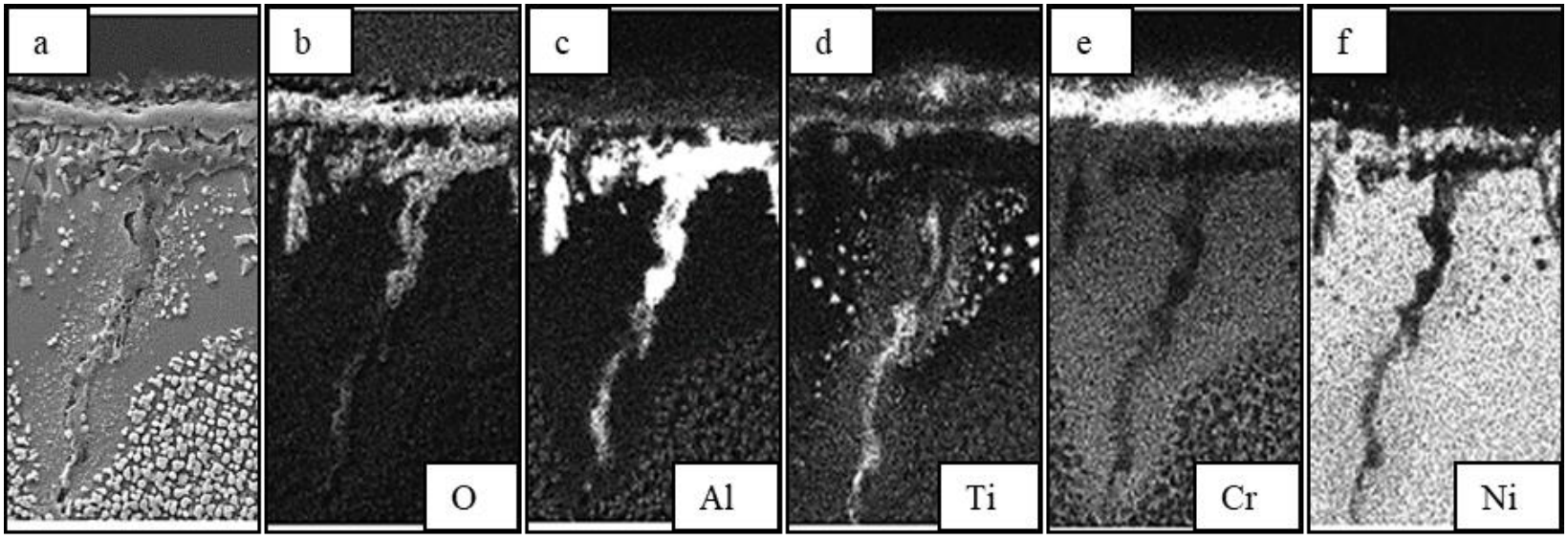

Figure 4-14. The EDS elemental mapping of the grain boundary oxidation region in IN738LC after 50 cycles, where a) is the SEM image and b), c), d), e) and f) are O, Al, Ti, Cr and Ni respectively.

4.6.2. Cross-sectional analysis of Rene 80

The cross-sectional microstructures of Rene 80 after 1000 cycles are shown in Figure 4-15. By comparing Figure 4-8 and Figure 4-15a, it can be concluded that grain boundary oxidation occurred before surface oxidation. An increase in oxidation cycles led to the formation of multiple oxide layers as displayed in Figure 4-15b. From EDS analysis, the layer beneath the external Mo-rich oxide was determined to be rich in Cr and Ti, associated with oxygen, indicating the formation of TiO_2 and Cr_2O_3. The morphology of the Mo-rich scale revealed a significant amount of porosity and therefore it was less compact than Cr_2O_3. As the cycles increased, this scale did not exhibit good adherence, unlike the Cr_2O_3 and Al_2O_3 oxide scales and after 600 cycles, Rene 80 underwent severe spallation. Most of the scale delamination and spallation occurred at the scale/alloy interface, further exposing the substrate to the oxidizing atmosphere, as shown in Figure 4-15c.

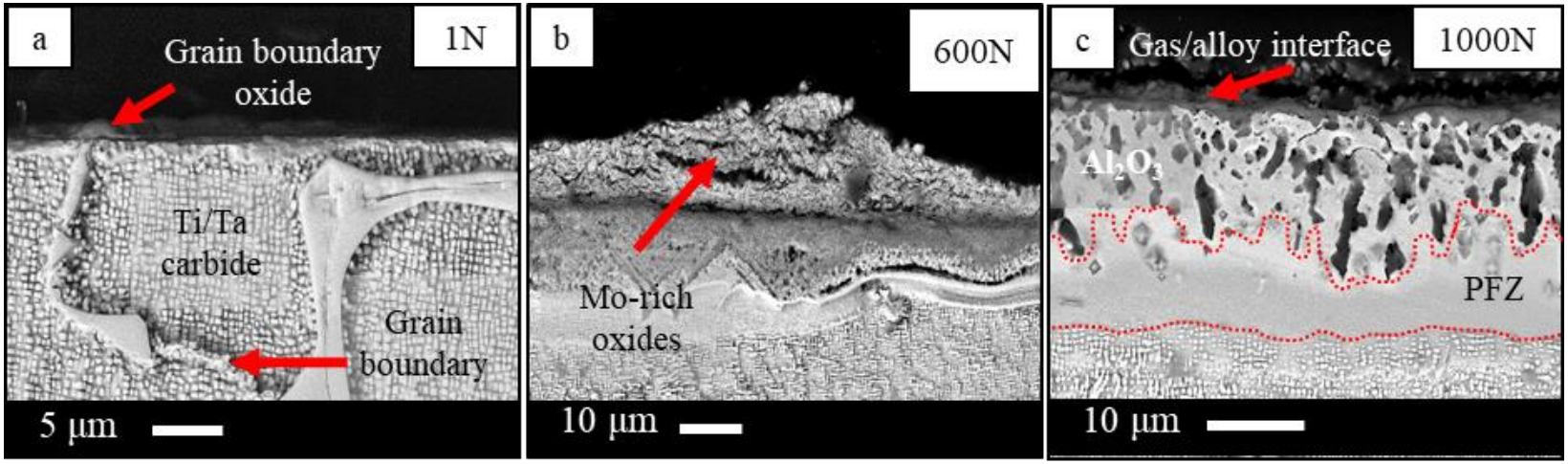

Figure 4-15. SEM-BSE cross-sectional microstructures of Rene 80, a) one cycle b) 600 cycles and c) 1000 cycles.

Since Rene 80 consists of columnar grain boundaries, intergranular oxidation was observed as shown in Figure 4-16. The depth of the grain boundary oxidation was approximately 40-50 μm, which was similar to that observed in IN738LC. The grain boundary surface consisted of Cr-rich oxides; the subsurface region of the grain boundary showed Al-rich oxides followed by Ti-rich oxides deep into alloy matrix. The subsequent cracking of these grain boundaries is also shown in Figure 4-16b; these cracks were severe compared to those found in IN738LC after the same number of cycles.

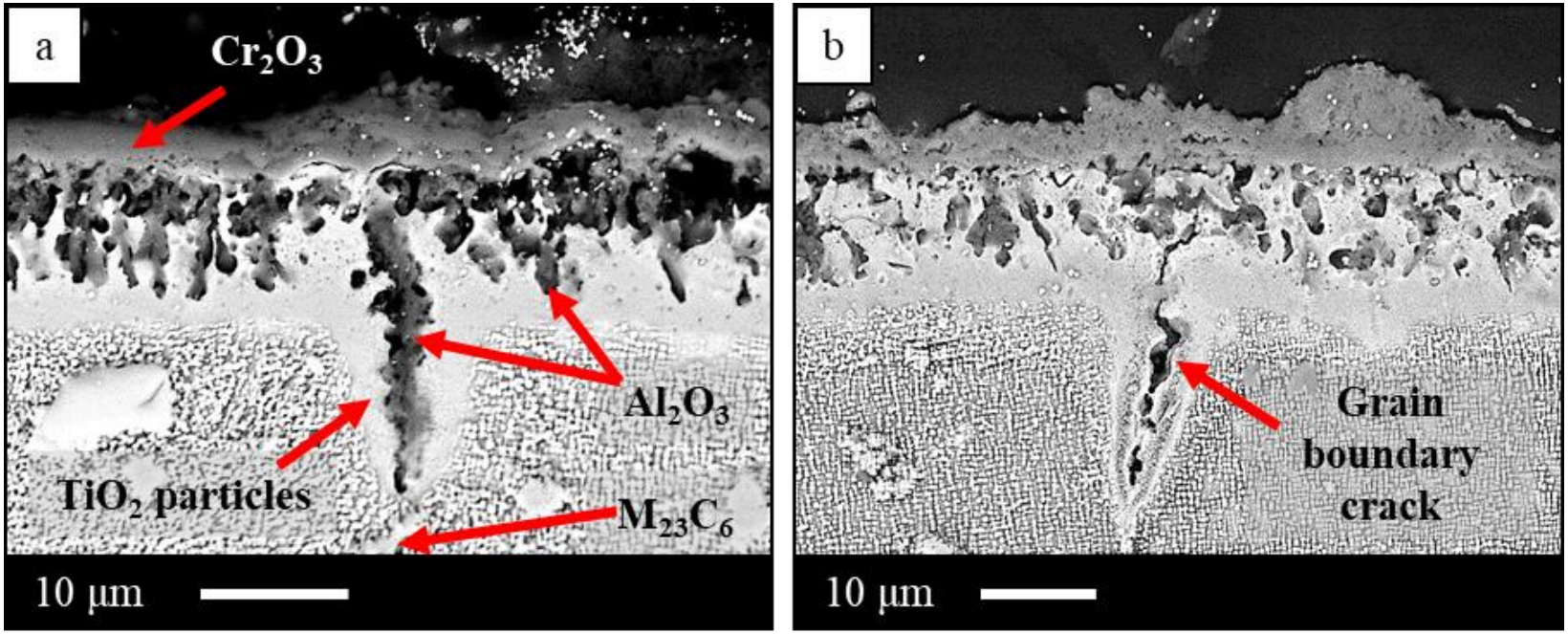

Figure 4-16. SEM-BSE microstructures of Rene 80 showing a) grain boundary crack initiation (100 cycles) and b) crack propagation (300 cycles) resulting from grain boundary oxidation.

4.6.3. Cross-sectional analysis of N5

Cross-sectional microstructures of N5 up to 1000 cycles are shown in Figure 4-17. The cross-sectional microstructures for one to three cycles did not display a distinct oxide scale; however, surface SEM-EDS analysis showed a thin transparent NiO layer and some spinel $NiAl_2O_4$ formation (Figure 4-11). The alloy exhibited excellent oxidation resistance due to the formation of a thin, continuous Al_2O_3 oxide scale; there was no evidence of internal oxidation. The oxide scale thickness was maintained for the entire 1000 cycles and was measured to be two microns thick.

The SEM analysis of the oxide scale revealed a characteristic three-layered structure as shown in Figure 4-17b. Here, Ni- and Al-rich oxides characterized region A; region B was rich in Al with a small quantity of Cr oxides and region C was Al-rich oxides. Further increase in oxidation cycles resulted in complete NiO scale spallation, retaining Al_2O_3 alone. From Figure 4-17b and Figure 4-17c, the cross-sectional microstructures revealed buckling and voids at the scale/alloy interface. This can be related to the sudden drop in specific mass change values followed by scale rejuvenation, which was shown in Figure 4-4c. The EDS analysis of the bright region on the external oxide scale in Figure 4-17c displayed the presence of Ta-rich layer associated with oxygen, which was found to be Ta_2O_5 form XRD analyses. The specimens also exhibited void formation below the thin Al_2O_3 scale.

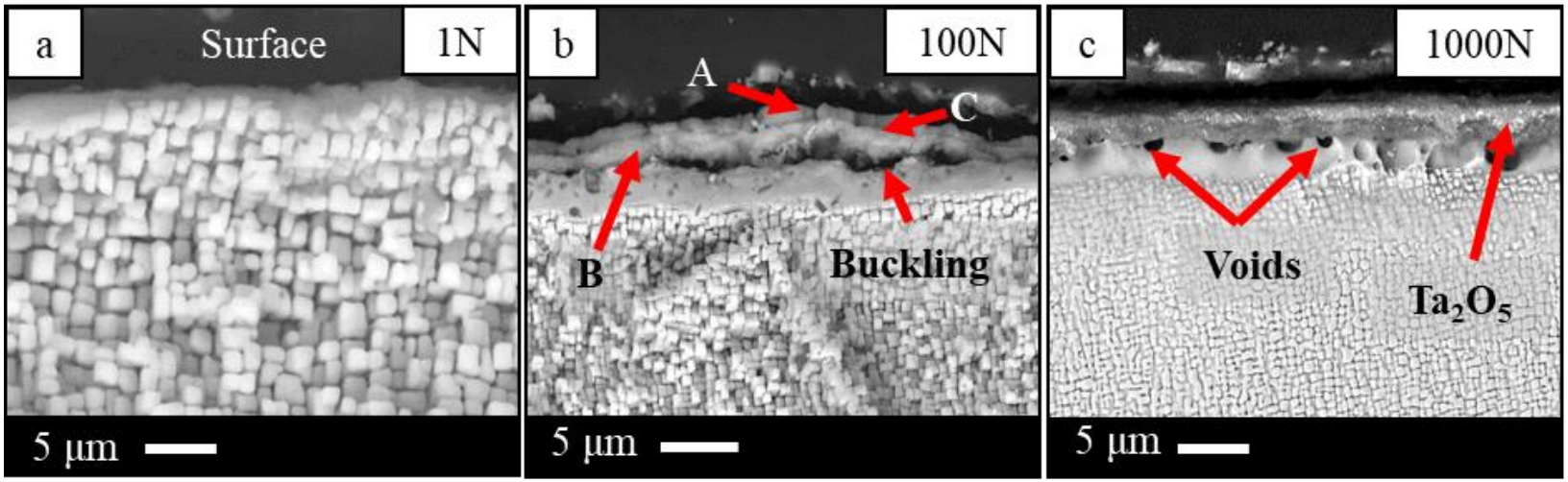

Figure 4-17. SEM-BSE cross-sectional microstructures of single crystal N5 a) one cycle b) 100 cycles and c) 1000 cycles.

As mentioned in the surface morphology section for N5, the alloy contains a significant amount of MC carbides in the interdendritic areas, which were identified as being Ta-rich eutectic regions. The selective oxidation of these regions occurred all over the surface to form Ta-Hf-rich oxy-carbide phases. The cross-sectional microstructure and corresponding elemental mapping of these regions are shown in Figure 4-18, where the Ta and Hf carbides are completely oxidized and an Al-rich oxide scale is formed beneath. Further increase in oxidation cycles led to the formation of micro-cracks and splitting of the oxy-carbides followed by delaminating from the Al_2O_3 scale at the scale/alloy interface as shown in Figure 4-19.

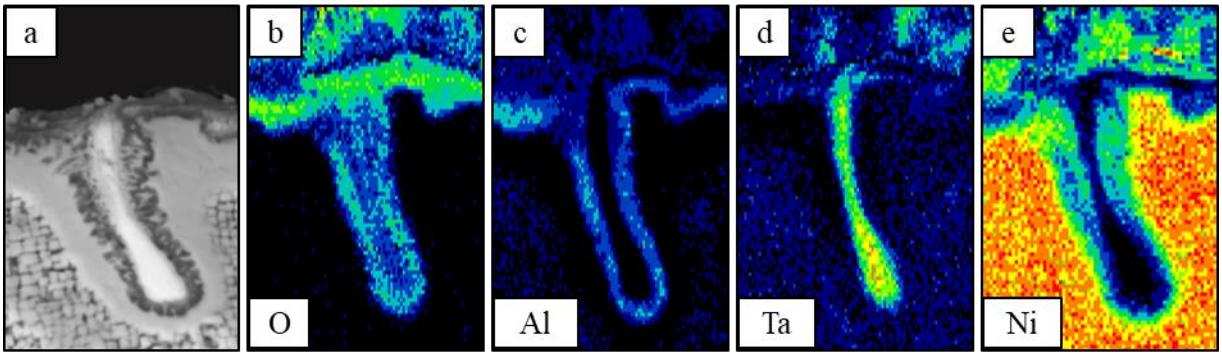

Figure 4-18. a) SEM-BSE cross-sectional microstructure of MC carbide region in N5 after 100 cycles and b), c), d), e) elemental maps of O, Al, Ta and Ni respectively.

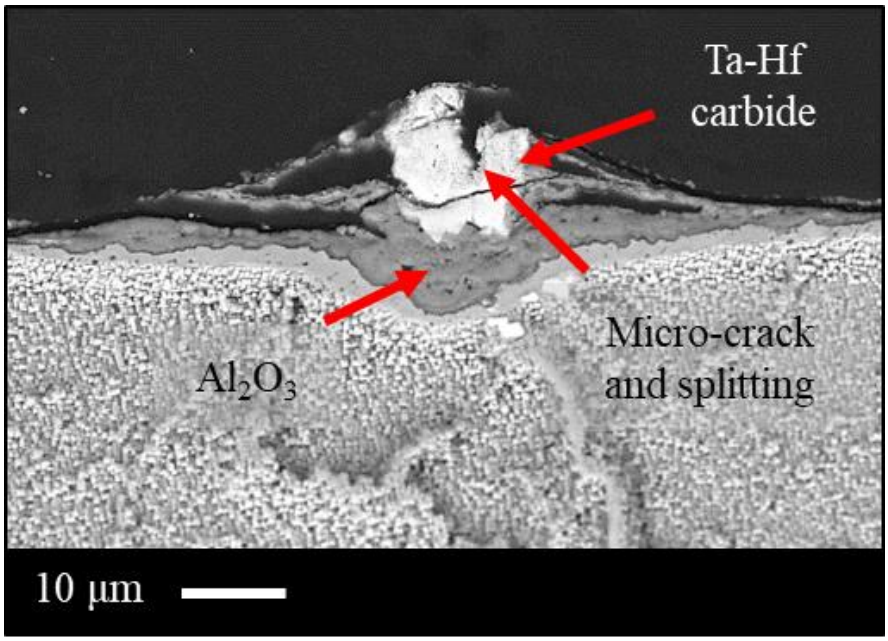

Figure 4-19. SEM-BSE cross-sectional microstructure of MC carbide in N5 showing micro-crack and carbide splitting.

4.7. Effect of cooling rate

To understand the effect of microstructural factors such as precipitate size, morphology, volume fraction as well as composition on oxidation and corrosion behaviour, alloy IN738LC was subjected to different cooling rates from solutionizing temperature such that a monomodal precipitate distribution was obtained. The results of the different cooling rate experiments are as follows:

4.7.1. Precipitate size distribution for as-received material

The microstructure and the precipitate size distribution (PSD) of the solution treated (as-received) IN738LC material are shown in Figure 4-20. The material consisted of a bimodal precipitate distribution with large cuboidal shaped primary γ' and small spherical shaped secondary γ'. The ImageJ software was used to determine the volume fraction and the average γ' size of the as-received material; these were found to be approximately 58 ± 1% and 274 nm respectively. The PSD revealed that the majority of the precipitates was less than 350 ± 15 nm. However, the equilibrium volume fraction of γ' at 20°C obtained from JMatPro was about 50%.

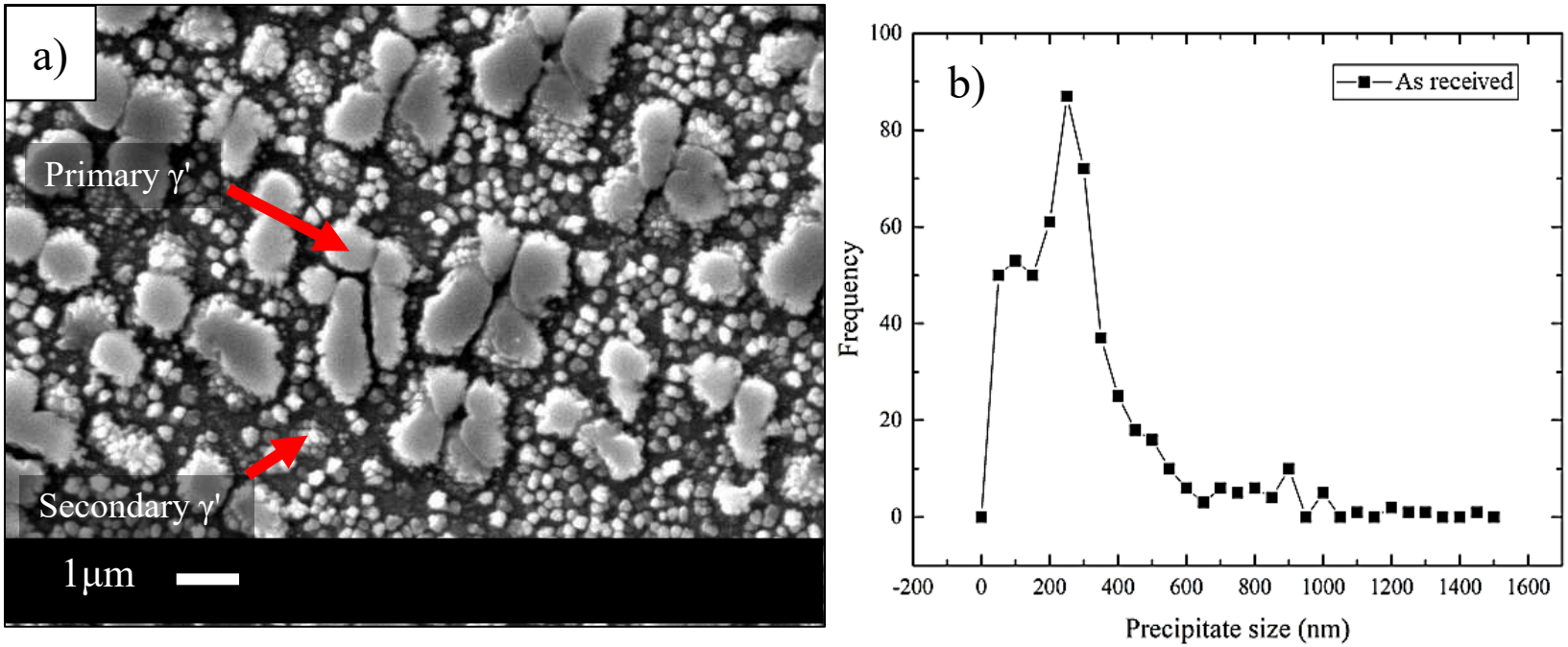

Figure 4-20. a) SEM microstructure and b) The precipitate size distribution of as-received IN738LC.

4.7.2. Continuous cooling precipitation

Figure 4-21 shows the precipitate size distribution for the samples cooled from 1200-800ºC at four different cooling rates. All four cooling rates revealed monomodal precipitate size distribution with the precipitate sizes varying from 50nm to 800nm. The water quenched (WQ) specimens exhibited the smallest precipitate size (50 ± 5 nm) with a spherical morphology as shown in Figure 4-21, which is the same order of tertiary gamma prime size in RR1000 [230]. However, there were no tertiary precipitates found in any of the present cooling rate samples. Since the number of γ' precipitates per unit area was higher in WQ (3000 ˚C/min) specimens, necking was observed between them. Figure 4-21b is an image of the 150 ± 10 nm precipitates formed from the 50˚C/min cooling rate. These are similar to the secondary precipitate size in the bi-modal PSD specimen shown in Figure 4-20. The 150 ± 10 nm sized γ' precipitate morphology was found to be spherical similar to those of precipitates found in the WQ specimens. The 5˚C/min and 2.5˚C/min specimens shown in Figure 4-21c and Figure 4-21d exhibited large cuboidal precipitate morphology with sizes of 400 ± 10 nm and 800 ± 10 nm respectively. The ImageJ analyses of the different cooling rate specimens suggested that the volume fraction of γ' precipitates increased with an increase in cooling rate as shown in Figure 4-22.

Despite the presence of secondary precipitates, the standard aged alloy displayed lower volume fraction γ' precipitates compared to other cooling rate specimens. The corresponding results are tabulated in Table 4-4 and the quantitative image analysis results are shown in Figure 4-23, which presents histograms of the probability distribution of the γ' precipitate sizes for each cooling rate assessed, where N on Figure 4-23 indicates the number of precipitates used for the measurement. The precipitates in all the samples appeared to conform to a monomodal size distribution.

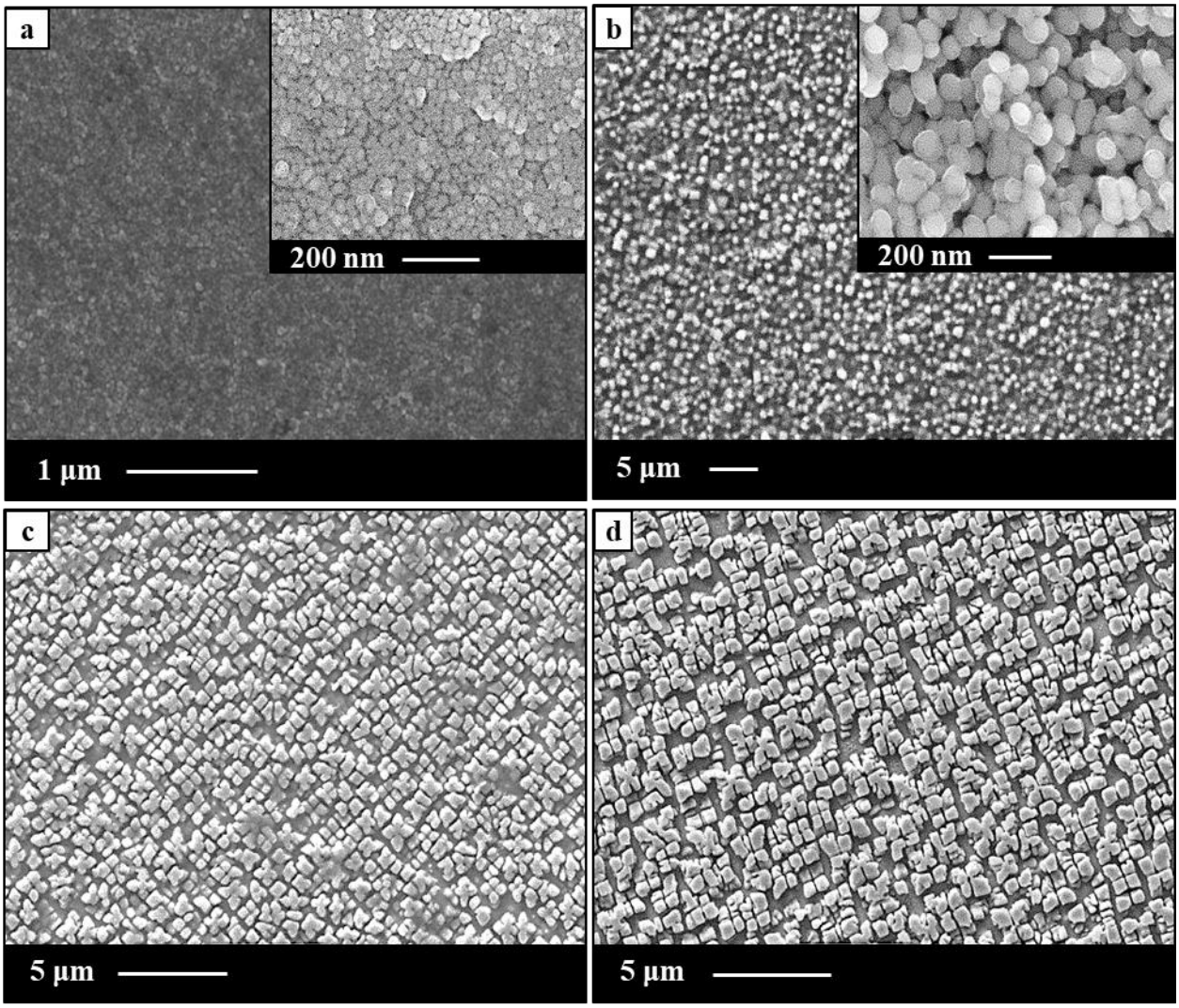

Figure 4-21. SEM microstructures of IN738LC cooled at a) 3000°C/min, b) 50°C/min, c) 5°C/min and d) 2.5°C/min.

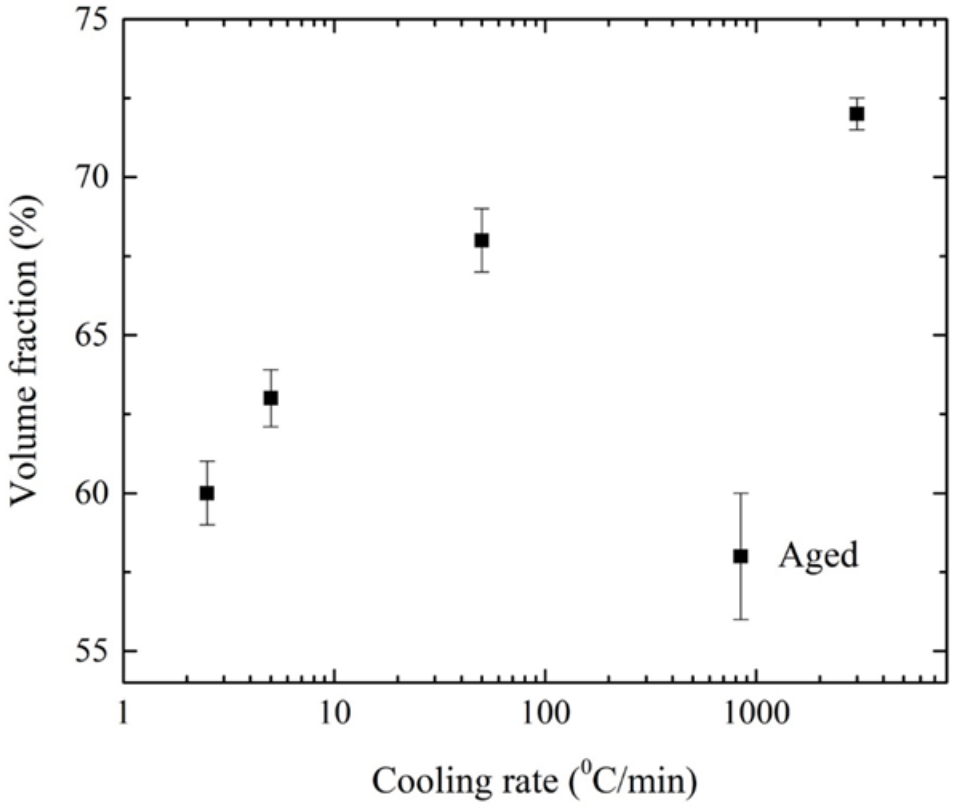

Figure 4-22. The volume fraction of γ' as a function of cooling rate for IN738LC.

Table 4-4. Summary of γ' precipitate size (nm) and volume fraction (%) as a function of cooling rate.

Specimen	Cooling rate (°C/min)	Precipitate size (nm)	Volume fraction (%)
A	Aged	100-500	58
B	3000	50 ± 5	73 ± 2
C	50	150 ± 10	68 ± 10
D	5	450 ± 10	63 ± 10
E	2.5	800 ± 10	60 ± 10

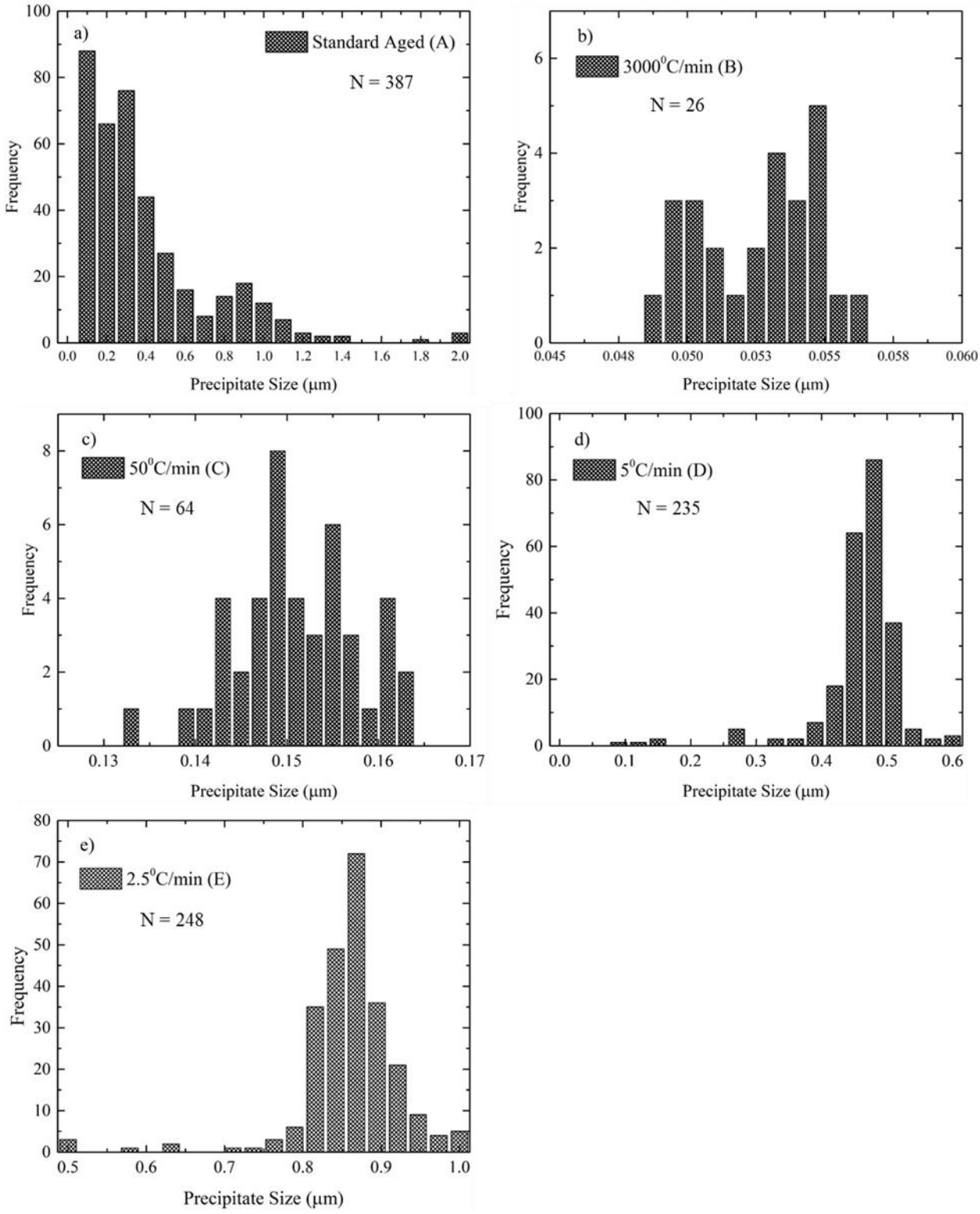

Figure 4-23. Histograms of the γ' precipitate sizes for the a) standard aged b) 3000ºC/min c) 50ºC/min d) 5ºC/min and e) 2.5ºC/min specimens.

The respective TEM dark field microstructures are shown in Figure 4-24. From Figure 4-24, the inter-precipitate distance was found to decrease and precipitate number density increase with an increase in cooling rate (i.e., decrease in γ' precipitate size). These results are summarized in Table 4-5. The corresponding size-dependent compositions of the γ' precipitates analysed using STEM-EDS are shown in Figure 4-25.

The reported compositional data are the average of 15-20 precipitates and the +/- is the standard deviation with a 95 % confidence level. The compositional analyses revealed a higher Al content in smaller γ' precipitates that obtained from specimen B and the concentration decreased with increasing precipitate sizes, whereas the γ stabilizing elements such as Co and Cr were found to increase with increasing precipitate size. The highest Al was measured to be 6.2±0.6 wt.% in the spherical precipitates formed by specimen B, compared to 4.5 ± 0.3 wt.% Al in the larger cuboidal precipitates formed by specimen E. In contrast, the compositional data for specimens B and E showed minimal compositional variations in Ti, i.e., 6.2 ± 0.8 wt. % and 7.1 ± 0.9 wt. % respectively.

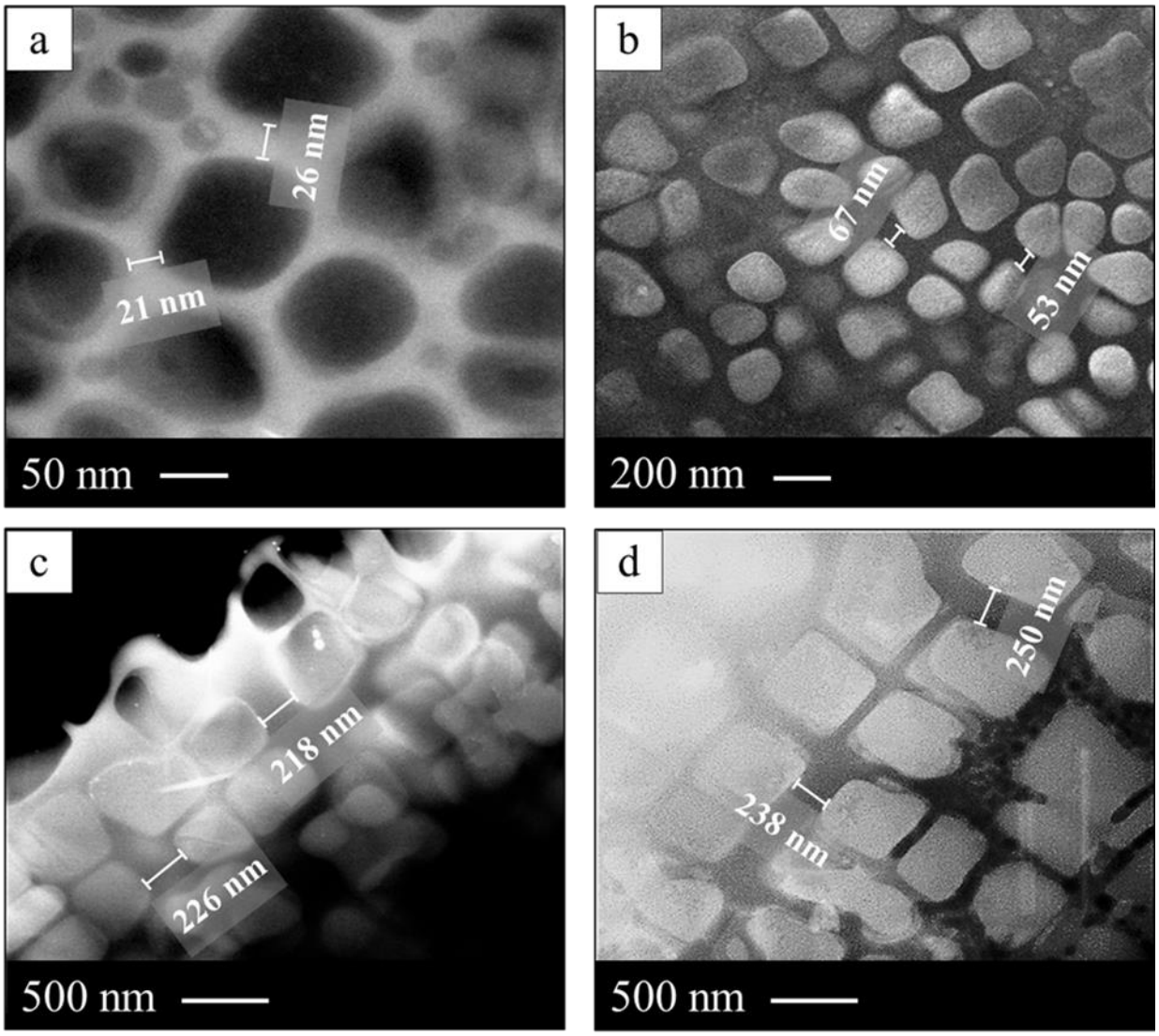

Figure 4-24. TEM dark field images for the different cooling rates a) 3000°C/min, b) 50°C/min, c) 5°C/min and d) 2.5°C/min.

Table 4-5. Inter-precipitate distance and precipitate density as a function of cooling rate.

Specimen	Cooling rate (°C/min)	Inter-precipitate distance (nm)	Precipitate number density (number of ppts./μm^2)
B	3000	25	12800 ± 500
C	50	65	1850 ± 54
D	5	220	100 ± 5
E	2.5	250	84 ± 3.27

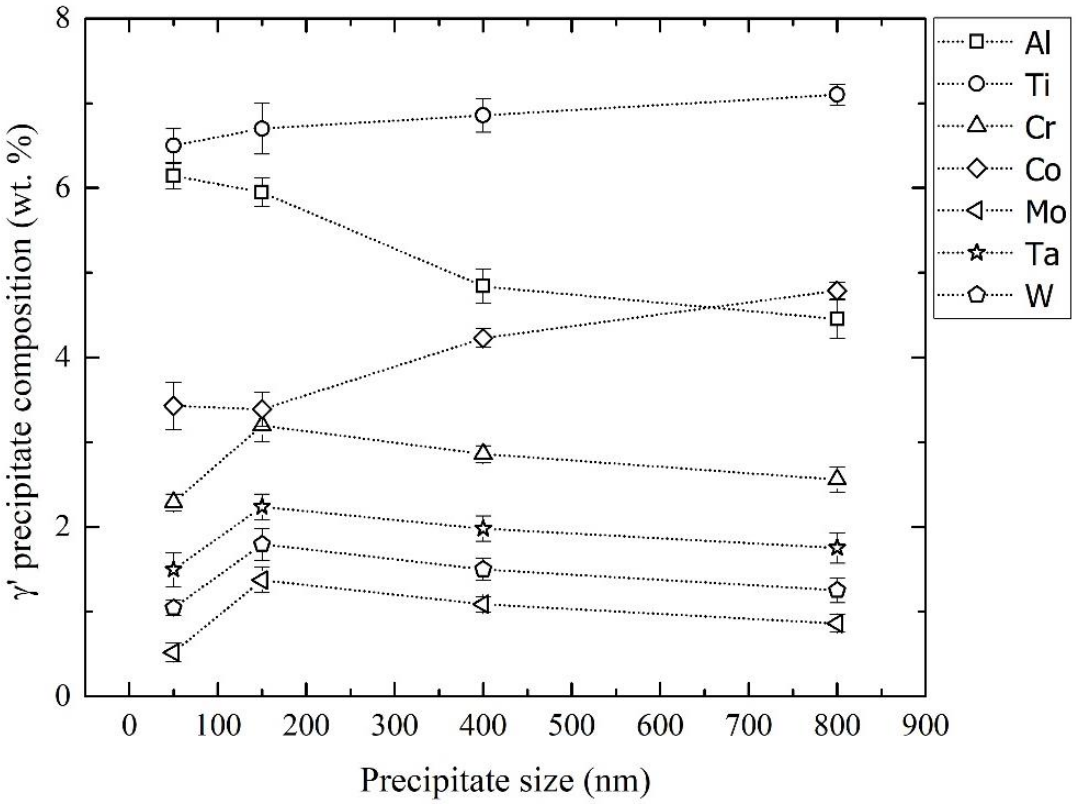

Figure 4-25. Compositions of γ' precipitates as a function of precipitate size as determined using STEM-super X-EDS spectroscopy.

4.7.3. Effect of γ' size on oxidation behaviour

To understand the influence of precipitate size on the oxidation behaviour and the PFZ thickness of IN738LC, the specimens were exposed to isothermal and cyclic oxidation at four different temperatures.

4.7.3.1. Kinetics of isothermal oxidation of IN738LC

Figure 4-26 illustrates the specific mass change of specimen A with bi-modal γ' PSD as well as monomodal γ' PSD specimens B, C, D and E with sizes of 50 ± 5, 150 ± 10, 450 ± 10, and 800 ± 10 nm, respectively, as a function of isothermal oxidation at 750, 850, 900, and 950°C in static air. A close observation of the specimens and the weight change plots revealed no spallation during the entire 150 h. It was apparent that the oxide growth rate of specimen B was more rapid relative to that of specimen E at 750°C. However, these differences reduced as the temperature was increased to 950°C. Also, the calculated specific mass gain of all specimens tested at 750°C was approximately 25% of those obtained at 950°C.

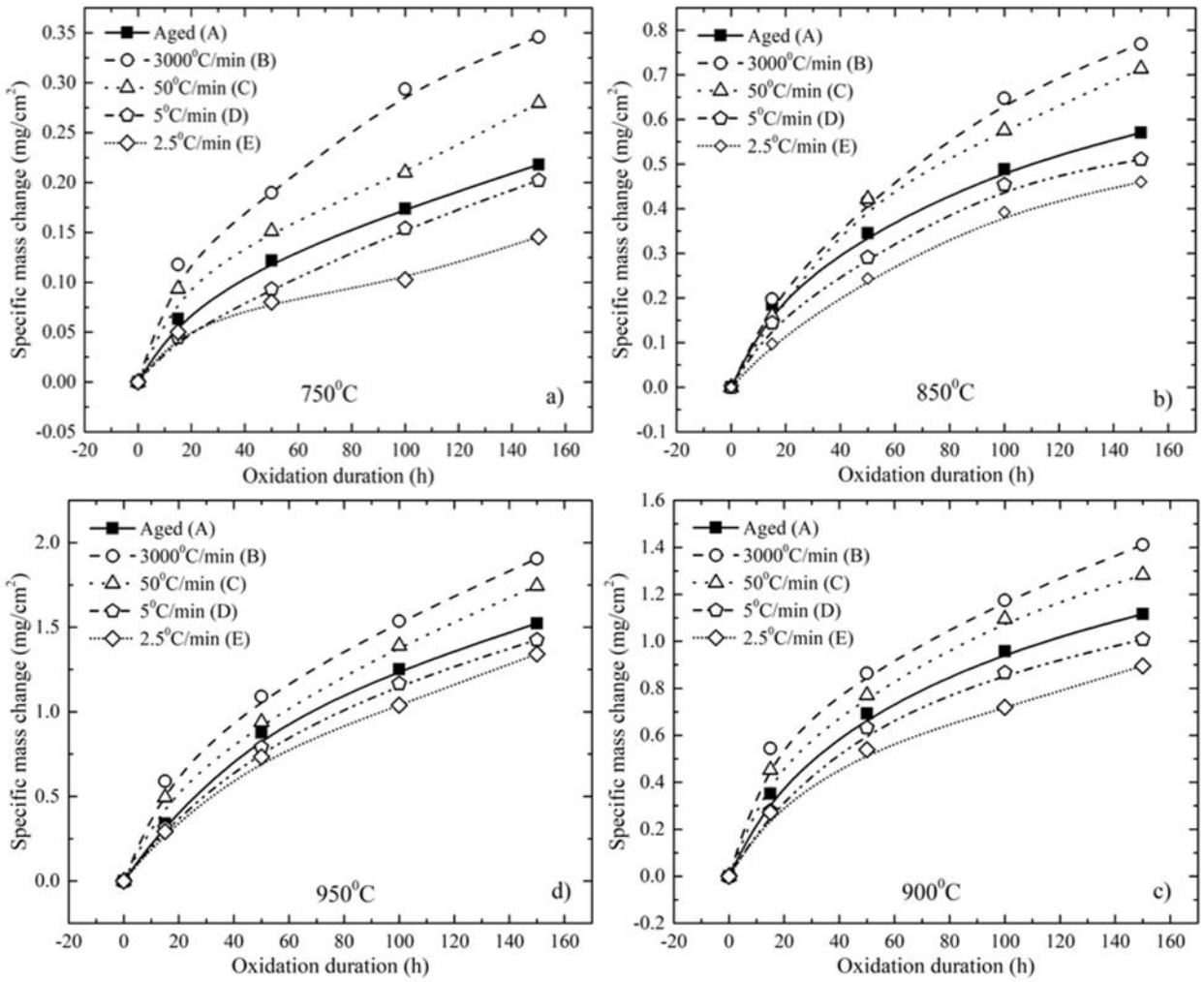

Figure 4-26. Plots of specific mass change as a function of isothermal oxidation duration for five heat-treated conditions for IN738LC at a) 750ºC, b) 850ºC, c) 900ºC and d) 950ºC.

The relationship between specific mass change and oxidation duration of all specimens followed a parabolic rate law. The parabolic rate constants, k_p for the different cooling rates were calculated from the linear relationship between mass change and square root of oxidation duration; these are listed in Table 4-6. The higher parabolic rate constant for specimen B suggested the least oxidation resistance relative to specimen E. The growth rate for specimen A was found to fall between specimens C and D (150 nm and 450 nm γ', respectively).

Table 4-6. A summary of isothermal oxidation rate constants, k_P, for the different heat treatment conditions as a function of temperature.

Temp. (°C)	Rate constants, k_P ($mg^2cm^{-4}s^{-1}$)				
	A	B	C	D	E
750	3.16E-04	8.11E-04	5.02E-04	2.75E-04	1.32E-04
850	2.21E-03	4.09E-03	3.45E-03	1.84E-03	1.49E-03
900	8.47E-03	1.30E-02	1.11E-02	6.98E-03	5.30E-03
950	1.59E-02	2.41E-02	2.04E-02	1.39E-02	1.21E-02

4.7.3.2. Isothermal oxide characterisation of IN738LC

Typical surface morphology and elemental line scan analysis of specimen A after 150 h of oxidation at 950°C in static air are shown in Figure 4-27. The oxide morphologies that developed on the surface of specimen A consist of multiple layers of oxides with a continuous external scale, internal oxidation in the subsurface zone, followed by a γ' PFZ. An Energy Dispersive X-ray

Spectroscopy (EDS) signal intensity for Ti in the outermost surface matches well with that of oxygen, indicating that the top layer is composed of a Ti-rich oxide. Beneath this layer, a Cr-rich oxide layer was observed. The thin layer beneath the chromium oxide layer was found to be a mixture of Ni, Cr, Al and O confirming a spinel, $Ni(Cr, Al)_2O_4$ and Ti- and Ta-rich oxide layer. The EDS signal intensity of discontinuous finger-like structures was rich in alumina. From Figure 4-27, Al depletion in the subsurface region was also observed. The EDS point analysis of the Al-depleted region showed a significant reduction in Al concentration from 3.4wt. % to 0.2wt. %.

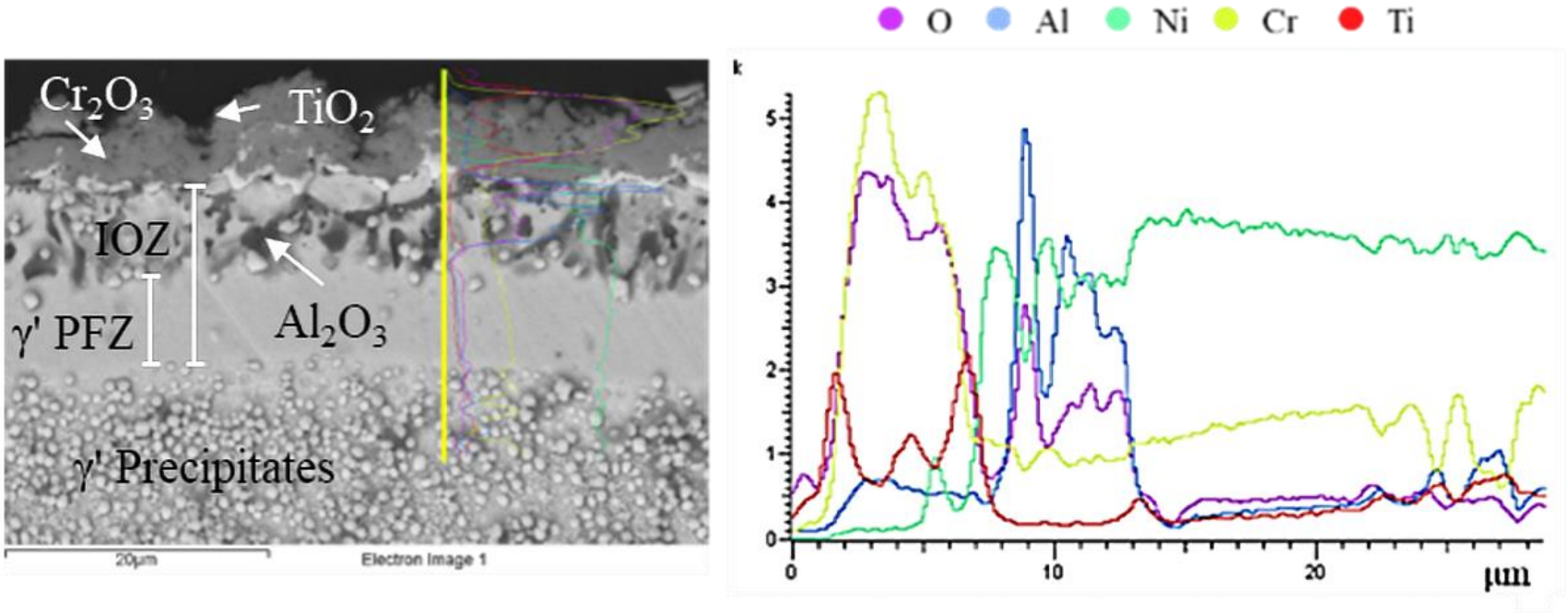

Figure 4-27. Elemental mapping showing the distribution of alloying elements for the standard aged IN738LC specimen (A) after 15 h of isothermal oxidation at 950°C in static air.

In order to understand the effect of γ' precipitate size, composition and volume fraction on oxidation kinetics as well as on depth of the γ' PFZ, specimens A, B and E were subjected to SEM microstructural analyses and the results are shown in the cross-sectional images in Figure 4-28. From the figure, it can be seen that specimen E (i - l) has similar oxide morphologies to those of specimen A (a - d) at all temperatures under isothermal conditions. However, the depth of the γ' PFZ is much larger in specimen A compared to specimen E. Additionally, the internal oxidation zone (IOZ) was more pronounced in specimen A, whereas specimen E showed a smaller depth of IOZ and a denser external Cr_2O_3 layer.

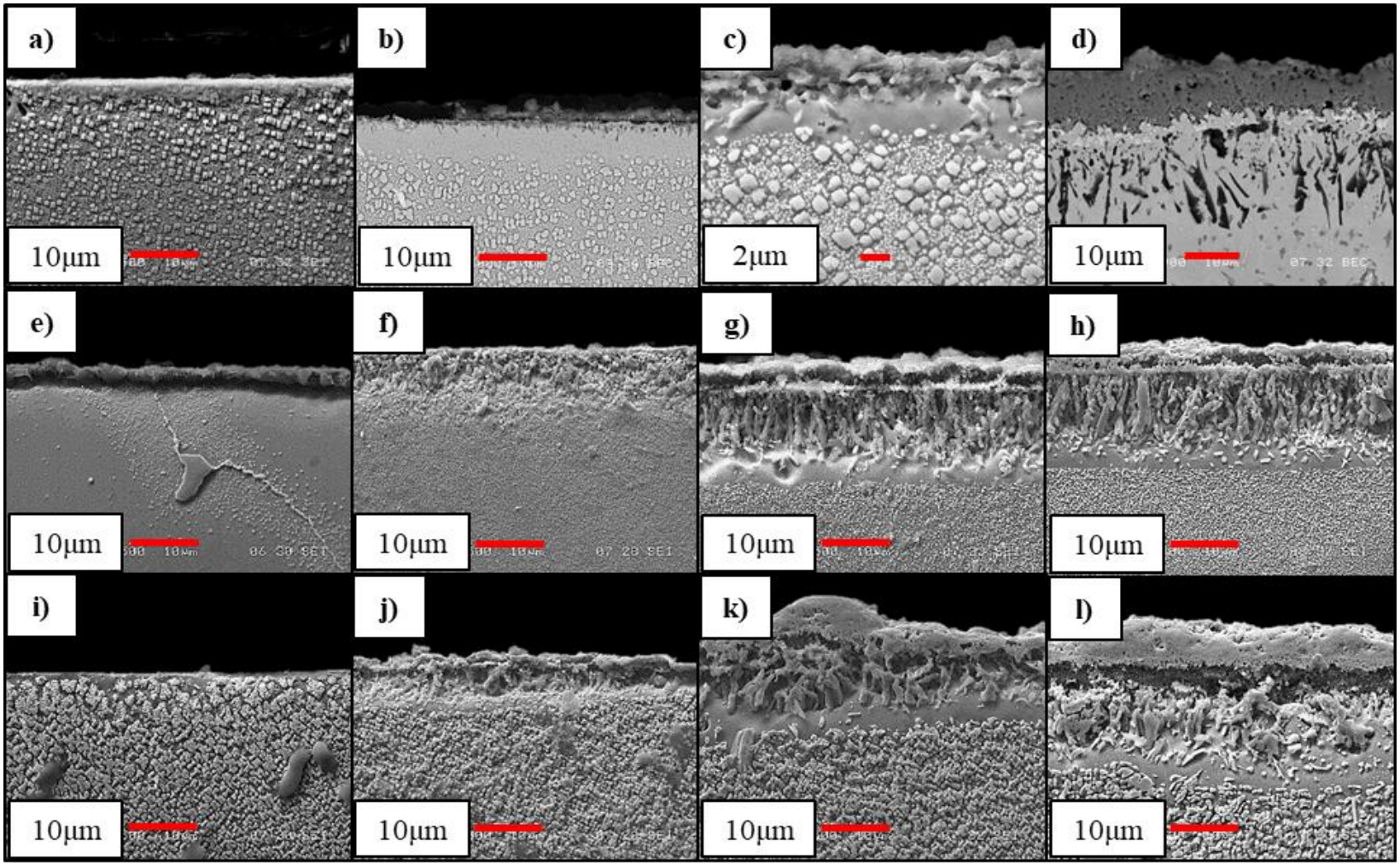

Figure 4-28. SEM-BSE cross-sectional microstructures of specimen A after 150 h isothermal oxidation at a) 750°C, b) 850°C, c) 900°C and d) 950°C; specimen B after 150 h at, e) 750°C, f) 850°C, g) 900°C and h) 950°C; specimen E after 150 h at i) 750°C, j) 850°C, k) 900°C and l) 950°C.

On the other hand, specimen B showed the formation of a cluster of oxide particles at the air/alloy interface (without the outer oxide scale) at 750°C after 150 h. As the temperature increased, specimen B revealed the formation of discontinuous and denser finger-like structures of oxides at the subsurface zone. The IOZ was found to be significantly thicker in specimen B compared to specimen A and E at all temperatures. Therefore, it is assumed that increasing the cooling rate increases the volume fraction of IOZ.

Since all specimens were prepared from IN738LC, which is a chromia former, it was expected that specimen B would have a thicker external scale similar to specimen A and E; however, it showed a thinner outer scale. Figure 4-29 illustrates the elemental distribution using EDS mapping. The EDS mapping of specimen B after 150 h at 950°C in air revealed that the external thin scale consists of Cr_2O_3 and TiO_2 with an Al_2O_3 layer at the subsurface zone. Overall, specimen B showed relatively low oxidation resistance, while the depth of γ' PFZ was twice that of specimen E and 0.86 times specimen A.

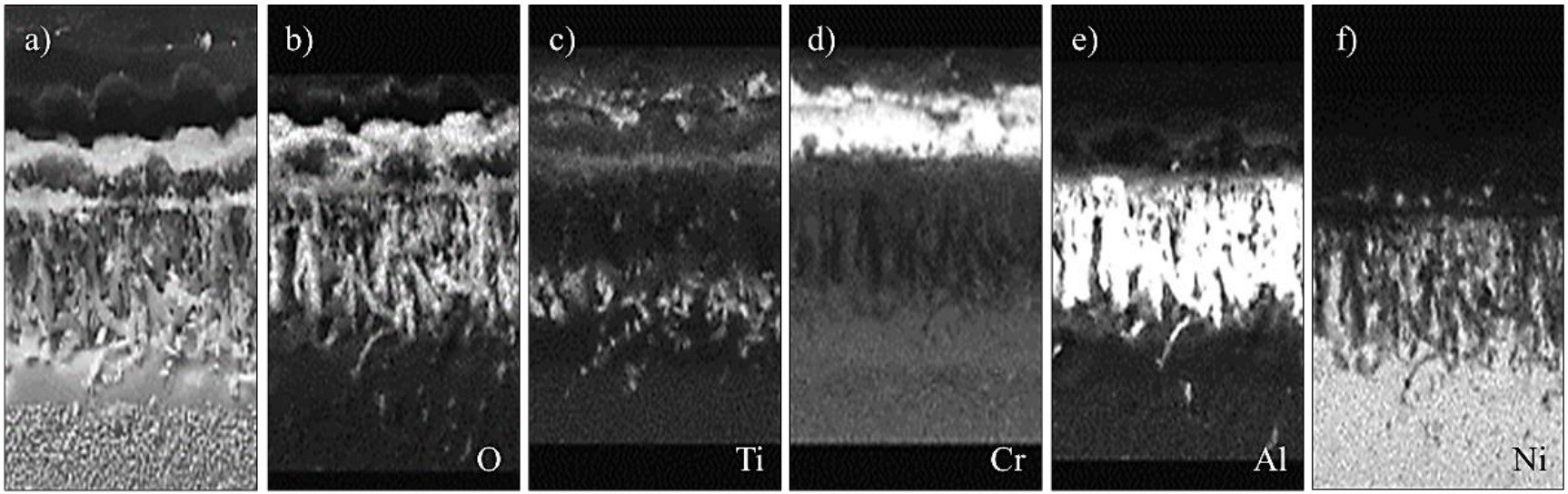

Figure 4-29. EDS mapping for the distribution of elements in the oxide region in specimen B after 150 h at 950ºC a) SEM microstructure, b) oxygen, c) titanium, d) chromium, e) aluminum and f) nickel.

4.7.3.3. Kinetics of cyclic oxidation of IN738LC

The cyclic oxidation results for specimens A, B, C, D and E (Table 4-4) are shown in Figure 4-30, where specific mass change is plotted as a function of oxidation cycles at 750, 850, 900 and 950ºC. The mass change behaviour during cyclic oxidation was similar to the isothermal tests at all temperatures. Specimen B showed a higher mass gain at all temperatures compared to other specimens. No scale spallation was observed during the entire oxidation tests for specimens A, C, D and E. However, specimen B displayed a small drop in mass after 100 cycles at 950°C, which can be attributed to scale spallation. The relationship between the square of mass change (mg^2/cm^4) and oxidation duration (number of cycles) revealed that all specimens followed a parabolic rate law. The parabolic rate constants, k_p, for all specimens at different temperatures in static air were calculated on the basis of 150 cycles and are tabulated in Table 4-7.

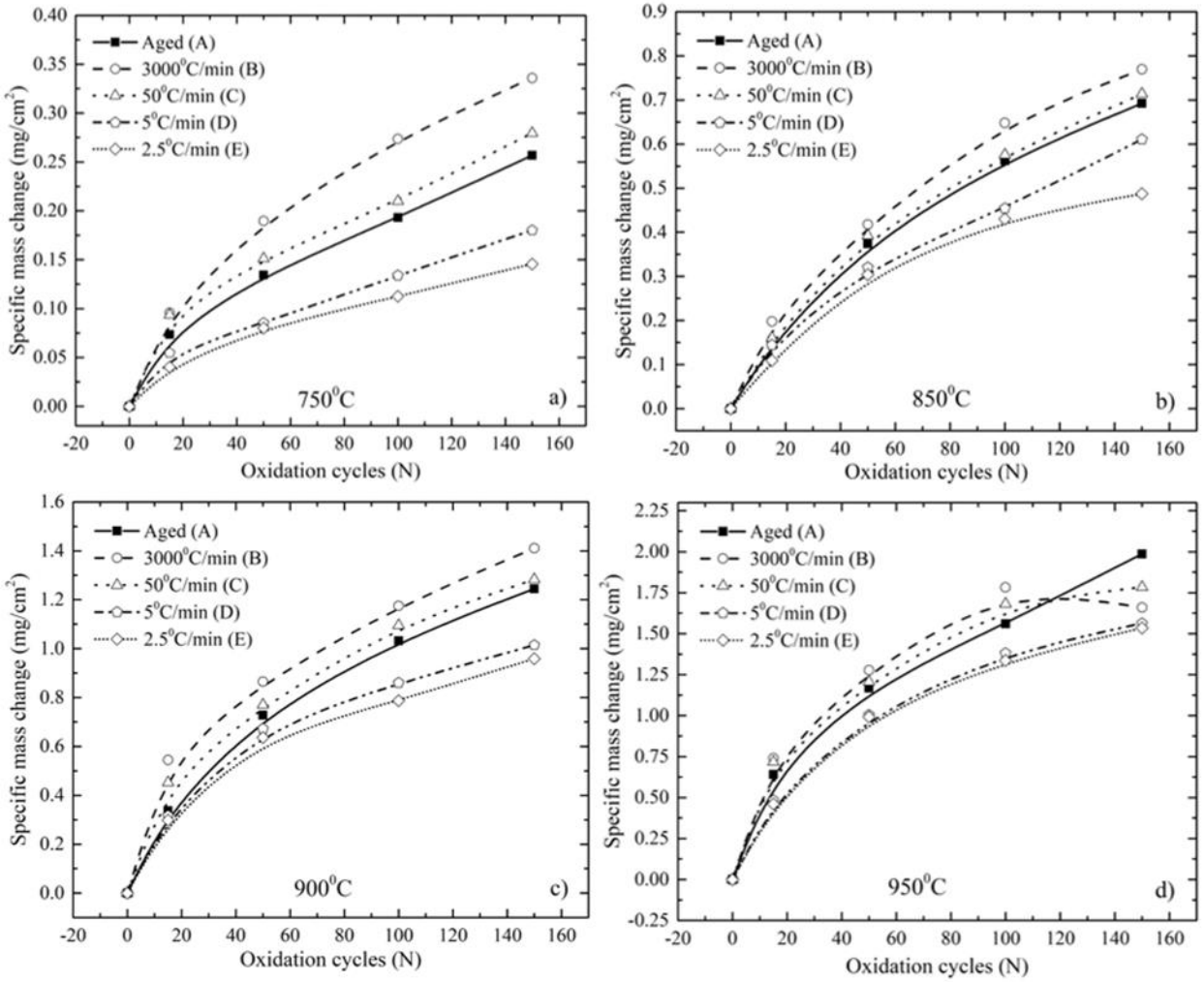

Figure 4-30. Plots of specific mass change as a function of oxidation cycles for five different heat-treated conditions for IN738LC at a) 750ºC, b) 850ºC, c) 900ºC and d) 950ºC.

Table 4-7. Summary of cyclic oxidation rate constants, k_P, for the different heat treatment conditions as a function of temperature.

Temp. (°C)	Rate constants, k_P ($mg^2cm^{-4}s^{-1}$)				
	A	B	C	D	E
750	4.30E-04	7.59E-04	5.02E-04	2.75E-04	1.37E-04
850	3.28E-03	4.09E-03	3.47E-03	2.45E-03	1.67E-03
900	1.05E-02	1.30E-02	1.11E-02	6.68E-03	5.93E-03
950	2.58E-02	3.05E-02	2.76E-02	1.68E-02	1.61E-02

4.7.3.4. Cyclic oxide characterisation of IN738LC

Cross-sectional SEM-Backcattered Electron (BSE) microstructures of the oxide scales developed on specimens A, B and E are shown in Figure 4-31. The oxide morphologies were similar to those found in the isothermal tests; an external Cr_2O_3 and TiO_2, spinel, thin Ta- and Ti-rich oxide scale beneath the outer scale and an internal oxide scale of Al_2O_3. The internal oxidation during cyclic oxidation had occurred to a greater depth than for the isothermal tests. Specimens A and E revealed no distinct oxide scale formation at 750°C after 150 cycles, whereas specimen B showed a measurable amount of oxide scale on the surface under the same conditions. Specimen A developed the thickest outer Cr_2O_3 scale followed by specimen E at 850, 900 and 950°C.

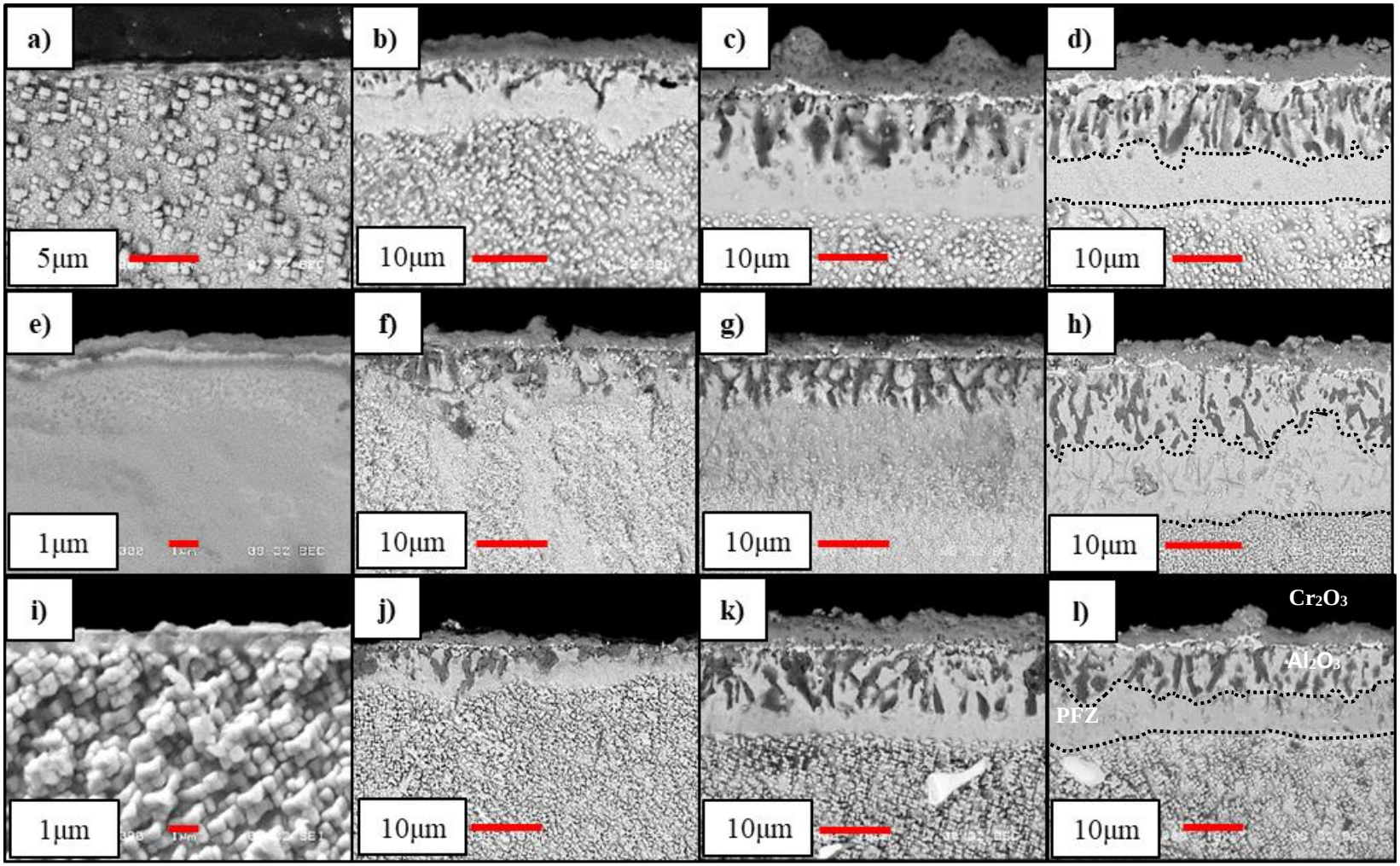

Figure 4-31. SEM-BSE cross-sectional microstructures of specimen A after 150 cycles of cyclic oxidation at a) 750°C, b) 850°C, c) 900°C and d) 950°C; specimen B after 150 cycles at, e) 750°C, f) 850°C, g) 900°C and h) 950°C; specimen E after 150 cycles at i) 750°C, j) 850°C, k) 900°C and l) 950°C.

4.7.4. Effect of γ' size on corrosion behaviour of IN738LC

To assess the relationship between the corrosion resistance and precipitate size, aqueous corrosion experiments were conducted at room temperature. The potentiodynamic polarization measurements for the corrosion of 3000˚C/min (specimen B) and 2.5˚C/min (specimen E) samples were carried out in three different aqueous solutions: 0.5M NaCl, 0.5M HCl and 0.1M H_2SO_4 at room temperature; these are shown in Figure 4-32a-c respectively. From Figure 4-32a, it is clear that neither specimen exhibited a passive layer in 0.5M NaCl solution. However, they showed small passivation regions in 0.5M HCl, as shown in Figure 4-32b. Even though specimen B had lower critical current density, i_{crit} and passivation current density, i_{pass} than specimen E in 0.5M HCl, it did not display any passivation region for up to 0.03 A/cm^2. However, specimen B later showed a small passivation range of 0.265 V against 0.7 V for specimen E. On the other hand, both specimens displayed good passivation range of 0.71 V and 0.8 V for specimens B and E respectively in 0.1M H_2SO_4 (Figure 4-32c). Overall, the chloride environment was much more aggressive compared to the sulphate environment for both specimens. As well, it is clear that the polarization curves for specimen B are shifted to the higher current density region compared to the slow furnace cooled specimen E in all three solutions. A summary of the corrosion data is tabulated in Table 4-8.

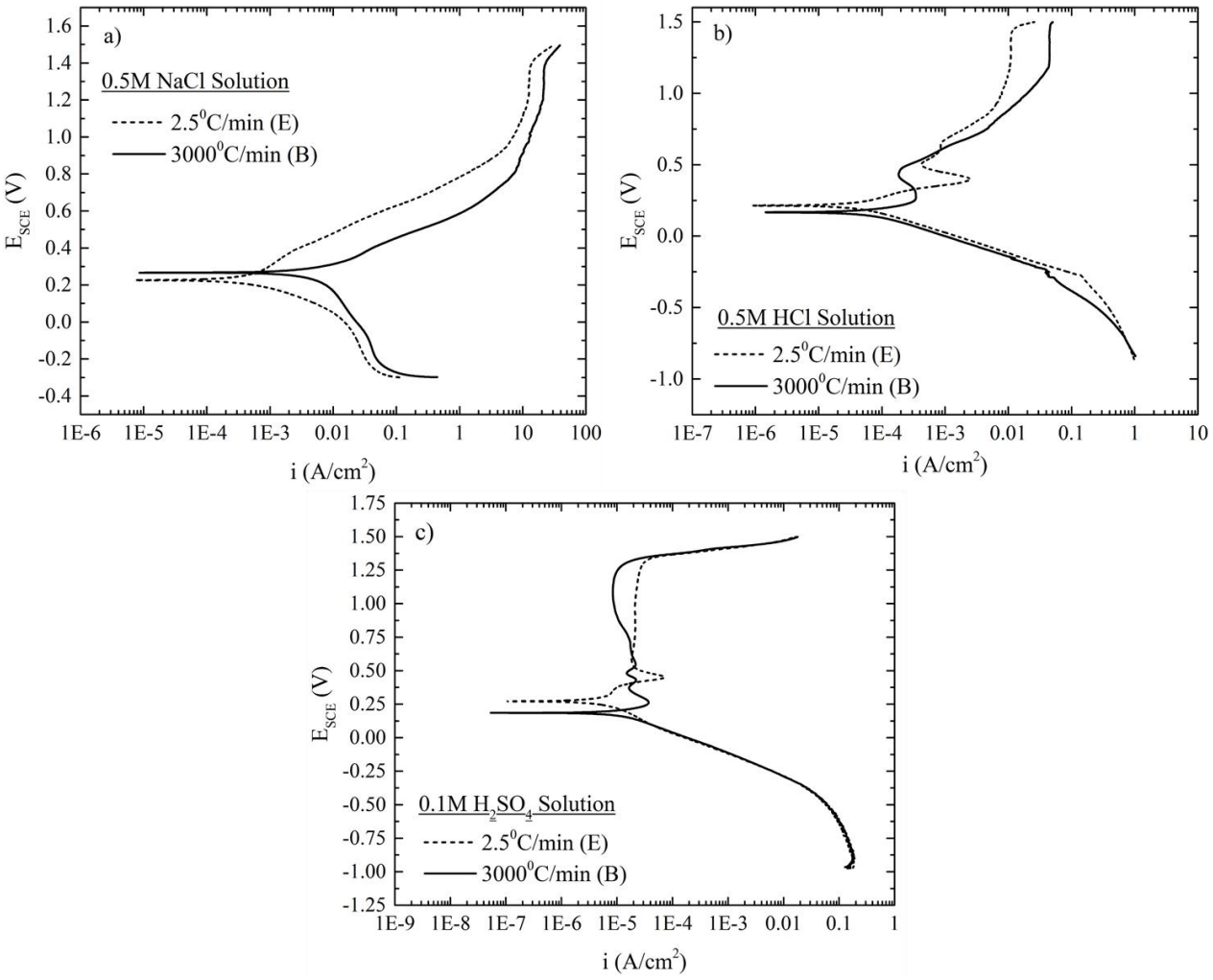

Figure 4-32. Potentiodynamic polarization curves for the corrosion of 3000 (B) and 2.5°C/min (E) specimens at room temperature in: a) 0.5M NaCl, b) 0.5M HCl and c) 0.1M H_2SO_4.

Table 4-8. A summary of potentiodynamic polarization results for specimens B and E.

Specimen	0.5M NaCl				
	E_{corr} (V)	i_{corr} (A/cm^2)	i_{crit} (A/cm^2)	i_{pass} (A/cm^2)	ΔE_{pass} (V)
B	0.33	4.10E-06	-	-	-
E	0.22	3.00E-07	-	-	-
	0.5M HCl				
B	0.19	6.50E-05	2.60E-03	0.8E-04	0.265
E	0.22	3.00E-05	2.80E-03	2.00E-04	0.7
	0.1M H2SO4				
B	0.19	1.30E-05	6.50E-05	8.00E-06	0.71
E	0.26	3.00E-06	2.80E-05	1.30E-05	0.8

Chapter 5 Discussion

5.1. Cyclic oxidation kinetics of the three candidate alloys

The oxidation kinetics of N5 obeyed the parabolic law for the entire 1000 cycles; this behaviour showed that diffusion of reactive species controlled the oxidation kinetics, i.e., cations and anions through the oxide scale and/or in the alloy. Onal et al. [231] reported similar behaviour during cyclic oxidation of N5 at 900˚C for up to 3500 cycles. The IN738LC and Rene 80 alloys initially exhibited positive weight change and then transitioned to negative after 300 and 600 oxidation cycles respectively; the mass gain is mainly due to scale growth on the alloy and the mass loss corresponds to oxide scale spallation.

From the XRD and EDS results, both IN738LC and Rene 80 alloys formed a thick Cr_2O_3 layer, whereas N5 showed thin and continuous Al_2O_3 scale on the surface. The microstructures observed in the present study are analogous to the findings of Geng et al. [232], Bensch et al.[20] and Cade et al. [223] for the same alloys. However, in contrast to the present study, Nowak et al. [233] reported no MoO_3 scale formation on the surface of Rene 80 during oxidation at 1050˚C in air for up to 100 h. This might be due to volatilization behaviour of MoO_3 at that temperature; Tei et al. [160] reported that the MoO_3 is volatile above 795˚C and sublimates at 1155˚C.

The parabolic rate constant for chromia-forming IN738LC and Rene 80 alloys (for up to 300 cycles) was calculated to be approximately 30 times higher than for N5, an Al_2O_3 former for the same number of cycles. Generally, below 1000ºC Al_2O_3 will exist in all its allotropes (γ, δ and θ phases), which are unstable and therefore considered to be non-protective [234], [235]. Hence, Cr_2O_3 is preferable at these temperatures. However, in the present work, N5 exhibited a continuous

oxide layer throughout the 1000 cycles, which served as an effective cation diffusion barrier. This is likely due to the transformation of the allotropic phase to stable α- Al_2O_3, which exhibits low diffusivity for both cations and anions resulting in a reduced oxide growth [179].

Sato et al. [236] also recorded formation of an α- Al_2O_3 scale during oxidation of single crystal alumina-forming alloys at 900˚C in air and Swadzba et al. [237] studied the effect of temperature ranging from 1050 to 1150˚C for 100 h on the alumina phase and composition in a second generation single crystal superalloy. The latter authors concluded that an increase in temperature increased the θ-Al_2O_3 transformation to α-Al_2O_3.

The cyclic oxidation rate values for all three alloys after 300 cycles were two orders of magnitude higher than that of isothermal oxidation values at same temperature after 1000 h and has been reported [26], [223]. This is in agreement with the results reported by Bensch et al. [20] for IN738LC and N5 alloys. Finally, Taylor et al. [238] have reported a k_p value of 3.13×10^{-6} mg^2 cm^{-4} s^{-1} for oxidation of chromia-forming alloy RR1100 in air at 900ºC, whereas Nowak et al. [233] recorded an instantaneous k_p value of 4.7×10^{-5} mg^2 cm^{-4} s^{-1} for Rene 80 during isothermal oxidation at 1050˚C in air after 50 h.

The cyclic oxidation of N5 experienced a transient oxidation behaviour at the initial stages (50 cycles) followed by steady-state oxidation. A similar behaviour in alumina-forming alloys has also been reported by a number researchers [179], [198], [239]. In the present work, the slope of the transient stage was greater than that of the steady-state stage, explaining the higher initial oxidation rate; this decreased once the steady state was reached. The transient growth rate was found to be 1.8×10^{-3} mg^2 cm^{-4} s^{-1} up to 29,400 s and further increase in exposure duration decreased to 1.53×10^{-4} mg^2 cm^{-4} s^{-1}. The decrease in the rate constant was found to be due to the formation of Al_2O_3 along with spinel ($Ni(Cr,Al)_2O_4$). Smialek [228] has also reported that the

transient oxides always take a spinel form. The author also suggested that a decrease in the amount of transient oxidation and an increase in stable continuous Al_2O_3 results in an increase in oxidation resistance. This transient oxidation proceeded until a thermodynamically stable continuous single oxide scale formed on the surface; this lowers the dissociation pressure of oxygen, P_{O_2} at the scale/alloy interface. Further increase in the number of cycles led to other rapidly diffusing cations such as Ta to move from the substrate and subsequently oxidize forming Ta_2O_5, as evident by the bright layer in Figure 4-17c. Pint et al. [240] reported a similar type of Ta and Hf rich oxide particle segregation at the scale/alloy interface. Finally, a dense, compact Al_2O_3 layer will form beneath all scales. This layer offers the best high-temperature oxidation resistance, with an equilibrium P_{O_2} of 5×10^{-25} atm. [3].

There was no evidence of a transient oxidation stage for either IN738LC or Rene 80 under the same conditions. The oxides formed at the transient stage on the surface of IN738LC and Rene 80 might have continued from the steady state; however, there was no change in slope to distinguish the transient state and steady state.

According to the scale spallation results, the alloys are ranked from best to worst: N5 > IN738LC > Rene 80. The initial scale spallation in IN738LC and Rene 80 was observed at the scale/alloy interface and later within the scales as shown in Figure 4-6 and Figure 4-8. Barrett and Lowell [241] studied oxidation kinetics and spallation behaviour of 25 chromia-forming alloys and concluded that the majority of scale spallation occurs due to the formation of spinels as a result of increased brittleness of the oxide scale. However, in the present work, the majority of scale spallation in IN738LC and Rene 80 was observed at the TiO_2/Cr_2O_3 and MoO_3+TiO_2/Cr_2O_3 interfaces respectively. The Rene 80 and IN738LC alloys showed the most significant amount of scale spallation by undergoing breakdown mass loss kinetics after 600 and 300 cycles respectively.

On the other hand, the small amount of spallation in N5 was observed at the scale/alloy interface. The alloy continuously displayed iterative spallation and rejuvenation behaviour for up to 1000 cycles. Unlike IN738LC and Rene 80, N5 did not undergo breakdown mass loss for the entire 1000 cycles. A similar analysis by Pint et al. [240] on N5 also reported no severe scale spallation. However, in the same work, the authors reported abrupt mass change due to the spallation of the NiO layer from the surface. McVay et al. [242] reported that the alumina scale must exhibit good adherence in order to confer protection from further oxidation. Pint et al. [243] reported an increase in scale adhesion property in alumina-forming alloys by co-doping more than one reactive element such as Hf, Y and La. However, in the present work, the presence of Hf in eutectic carbides resulted in scale spallation (Section 5.3.3. Tantalum and Hafnium). The microstructural observation of all three oxidized alloys agrees with measured weight change data. For example, the severe scale spallation microstructure of Rene 80 (Figure 4-10) can be correlated with the negative slope of specific weight change as a function of oxidation cycles curve (Figure 4-4b). The spallation rates (Table 5-1) after breakdown oxidation indicated that IN738LC and Rene 80 formed less protective scales after breakdown.

Table 5-1. Spallation rates after breakdown oxidation in IN738LC and Rene 80.

Alloy	Rate ($mg^2\ cm^{-4}\ h^{-1}$)
IN738LC	-3.69×10^{-3}
Rene 80	-2.3×10^{-2}
N5	-

5.2. Cyclic oxidation modelling

The experimental data from the cyclic oxidation experiments for IN738LC were fitted to the COSP-Monte Carlo model to calculate rate kinetics and the fraction of scale spalled in each cycle. The computer-simulated results were presented in Figure 4-4a. From the figure, the best fit for IN738LC was a parabolic relationship with $k_p = 1.6x10^{-2}$ ($mg^2.cm^{-4}.hr$) and $C_o/C_m = 3.85$ (C_o is the cycles required to for specific weight gain reaches zero and C_m are the cycles to reach maximum weight gain). A spallation constant, Q_0, of 0.0001 cm^2 mg^{-1} was determined for IN738LC. The fraction of scale spalled was also calculated from the model and found to be 0.07% of total scale weight; the final mass of scale retained was calculated to be 8.83 mg cm^{-2} after 1000 oxidation cycles. The alloy showed a maximum weight gain of about 1.5 mg cm^{-2} at 200 cycles followed by zero crossover at 854 cycles. The number of cycles for zero crossover can be considered as a life expectancy for the alloys at those conditions. Therefore, the results for IN738LC showed that the alloy could withstand a maximum of 854 cycles before material loss exceeds rejuvenation under the experimental conditions employed.

For Rene 80 the test results showed severe scale spallation after 600 cycles. Here parabolic oxide growth rate using the COSP-Monte Carlo model did not provide a good fit. However, the power-law using an average stoichiometry constant of 3.4162 ($NiMoO_4$ and MoO_3), where MoO_3 and NiMoO4 were the major oxides spalled gave the best fit for up to 700 cycles and thereafter deviated from the experimental data. Thus, the COSP-Monte Carlo model could not take into account sudden increase in weight loss due to severe $MoO_3/NiMoO_4$ spallation. The oxidation rate constant from this model was determined to be $k = 1.12x10^{-2}$ ($mg^2.cm^{-4}.hr$) and using the power law with m =1.5, gave $C_o/C_m = 3.22$. A reasonable fit to the experimental data was found when

the value of α was unity in equation 31 (section 2.24.2), where α is an exponent of the dependence of fraction of oxide spalled, F and specific mass of oxide before cooling on each cycle, W'_{ri}.

In the present work, the best curve fit for the Rene 80 cyclic oxidation experimental data was found when α was increased from unity to 2. The rate constant, *k* was then determined to be 7.75×10^{-3} ($mg^2.cm^{-4}.hr$) at m=1 and the ratio C_o/C_m was determined to be 2.28 for the best fit as displayed in Figure 5-1. The model calculated the scale spallation constant, Q_0 to be 0.000112 cm^2 mg^{-1} and the fraction of oxide spalled to be 0.21%. The fraction of oxide-spalled value is significantly higher than that found for the other chromia-forming alloy IN738LC, suggesting severe scale spallation in Rene 80 as was found experimentally.

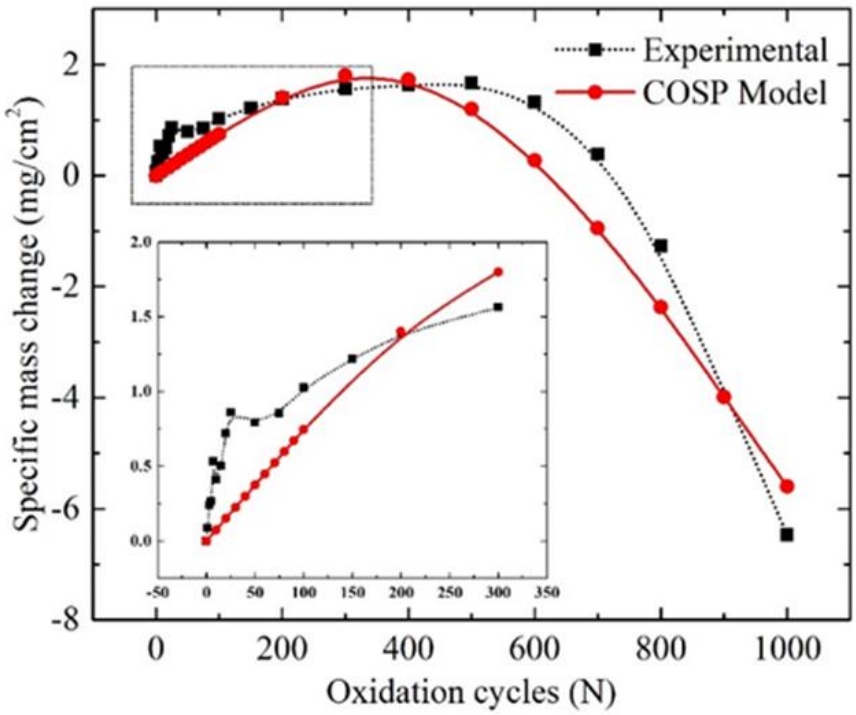

Figure 5-1. Fitting of cyclic oxidation kinetics for Rene 80 after 1000 cycles using the COSP-Monte Carlo model when α = 2.

Since N5 exhibited parabolic weight change behaviour with minimal scale spallation, the parabolic growth rate was used to determine the rate constant and spallation constant (Figure 4-4c). The rate constant was determined to be, $k_p = 2.8 \times 10^{-4}$ ($mg^2.cm^{-4}.hr$) with spallation constant, Q_0 of 0.0003 $cm^2\ mg^{-1}$. The alloy took 498 cycles to reach a maximum weight gain of 0.33 mg cm^{-2} and exhibited 11 times slower scale growth rate compared to that of IN738LC and Rene 80 under the same conditions. The measured and calculated maximum weight gain values are in good agreement with the findings of Onal et al. [244] for the same alloy. Since N5 is an alumina-former and the Al_2O_3 scale had good adherence behaviour, the fraction of oxide spalled was found to be very low, i.e., 0.03% compared to the two chromia-forming alloys IN738LC and Rene 80 with 0.07% and 0.21% respectively. The accuracy of the model is addressed by calculating the standard error of the estimate between the experimental and modelled data and was calculated to be 0.104 for IN738LC revealing a good fit compared with reasonable fits for N5 and Rene 80 (error values of 0.4 and 0.7 respectively).

5.3. Effect of alloying elements on cyclic oxidation

5.3.1. Titanium

Earlier research on the effect of Ti concentration on chromium activity using JMatPro modelling suggested that an increase in Ti resulted in an increase in chromium activity and subsequent increase in oxidation rate [13]. The present work also agrees with the JMatPro results. The addition of more than critical Ti wt. % would result in metal-deficient, i.e., p-type Cr_2O_3 by Ti^{4+} ions [245]. An alloy containing 1 wt. % Ti would have a lower chemical activity of Cr than an alloy with higher Ti. Higher Cr activity results in a higher oxidation rate by increasing the gradient of

chromium and oxygen activity across the external scale. Additionally, TiO_2 has a higher coefficient of thermal expansion, 8.4-11.8E-6 C^{-1} [246] compared to that of Cr_2O_3, 5.86 - 8.12E- 6 C^{-1} [247]; this difference is expected to result in the severe scale spallation found.

5.3.2. Molybdenum

The extent of scale spallation was most severe in Rene 80, which had the highest Mo content. Significant Mo-rich oxide scales were visible, both on the surface and on cross-sectional microstructures. These were shown in Figure 4-9 and Figure 4-15b. From XRD and EDS analysis, these Mo-rich layers contained high volume fractions of Mo-oxides, such as MoO_3 and $NiMoO_4$. Since Mo requires a lower partial pressure of oxygen to form its oxide compared to the other elements present, Mo will selectively oxidize to form MoO_3/$NiMoO_4$ [228]. The formation of these Mo-oxides adversely affected the oxide scale density, which eventually decreased the oxidation resistance. Additionally, the melting temperature of MoO_3 is ~795˚C [248] and the maximum temperature for each cycle in the present study was 900˚C. Therefore, the MoO_3 will start vapourizing and eventually create porosity on the Mo-rich oxides as shown in Figure 4-9b. This porosity acts as a rapid diffusion path for cationic and anionic migration across the oxide scale to the alloy, which further enhances the oxidation. Further increase in oxidation cycles led to a continuous layer of Cr_2O_3 and TiO_2, covering the MoO_3 as shown in Figure 4-10.

The catastrophic spallation after 600 cycles in Rene 80 may be attributed to increasing stress within the oxide scale due to volume change. The growth stresses generated by the formation of MoO_3 can be estimated knowing their Pilling-Bedworth ratio (PBR), which is the ratio of the volume of oxide to the volume of metal consumed to form an oxide [3], [7]. The PBR for MoO_3/Mo was calculated to be high, 3.29, and therefore significant internal compressive stresses would be

expected to develop, leading to cracking and a reduction in the adhesion between the oxide scale and substrate, resulting in the severe scale spallation noted.

5.3.3. Tantalum and Hafnium

Alloy N5 contained significant amounts of Ta and Hf carbides in the eutectic regions. These carbide phases increase the strength of the alloy but are also prone to oxidation [249]. If the carbides are located at the metal surface, they undergo selective oxidation. The carbide oxidation mechanism is different from that of matrix oxidation. The oxide formed during matrix oxidation forms a protective scale, whereas the oxides formed on the carbides are non-protective [250]. The interface between the oxide and carbide is more vulnerable to scale spallation. The oxidation of Ta causes a substantial volume change, i.e., TaC_{PBR} = 2.23. The combined effect of different oxidation rates and a large volume change generates a high shear strain at the matrix oxide and oxy-carbide interface as shown in Figure 4-18. The increase in thermal cycles aggravates this process, resulting in cracks and de-cohesion of the oxide scale. In agreement with the present work, Pint et al. [178] reported that the presence of Ta does not enhance the life of the oxide scale.

Another cause of scale spallation was the presence of micro-cracks in the oxy-carbides. These micro-cracks propagate at the scale/alloy interface with an increase in thermal cycles resulting in complete delamination of the oxide scale around it. On the other hand, they also lead to internal oxidation around the carbide particles as shown in Figure 4-19. A similar oxidation mechanism has been reported in other works [251].

5.4. Effect of microstructure on cyclic oxidation

5.4.1. Grain boundaries

Grain boundaries are three-dimensional defects, which allow rapid migration of cations and anions; therefore, they are prone to oxidize more rapidly than the matrix. Since the activation energy required for diffusion through a grain boundary is always less than that of lattice diffusion, the diffusion rate through a grain boundary is always higher [124]. Clemens [122] has determined the diffusion coefficient for lattice and grain boundary diffusion in alumina-forming alloys. For a grain size of 0.3μm, the lattice diffusion coefficient was found to be of the order of 10^{-17} cm^{-2} s^{-1} and for a 1 nm grain boundary, the diffusion coefficient was 10^{-12} cm^{-2} s^{-1}. In the current work, the thicker Cr_2O_3 oxide scales above the grain boundaries in Figure 4-14 and Figure 4-16 indicated that diffusion along the grain boundary not only enhanced the outward diffusion of chromia but also provided rapid migration of ions through it. This increase in Cr^{3+} diffusion outward through the grain boundary also increased the interfacial void formation. These voids rapidly grow and become grain boundary cracks during thermal cycling at high temperatures as displayed by both chromia-forming alloys.

5.5. Effect of cooling rate on γ' size

Both thermodynamic and kinetic phenomena can be used to explain the precipitation mechanism that occurs during different cooling rates. The effect of cooling rates on the precipitation mechanism was shown in Figure 4-21. Since all four specimens were cooled to below solutionizing temperature, the volume free energy, ΔG_v of the system increases. The magnitude of ΔG_v depends on the rate of undercooling and a higher undercooling results in a higher ΔG_v. This continues to

increase until the critical nucleation energy barrier, ΔG^*, is sufficiently low, allowing the nucleation to take place. The free energy equation is given below [57],

$$\Delta G^* = \frac{A16\pi\gamma^3}{3(\Delta G_v - \Delta G_s)^2} \quad (40)$$

Where, γ is the interfacial energy, ΔG_s is strain energy and A is the surface area.

The γ' precipitate size distribution in specimen B was monomodal, with size measured to be approximately 50 ± 5nm. For such a small precipitate size to occur, the specimen must undergo maximum undercooling so that the amount of time required for the growth of γ' precipitates is reduced, but at the same time the thermodynamic driving force for the nucleation will be high. As a precipitate nucleates at maximum undercooling, one would expect a high nucleation rate. It is well known that an increase in undercooling will increase the rate of nucleation exponentially [252]. Therefore, the nucleation density of the γ' precipitates in specimen B is very high and was shown in Figure 4-21a. Since these precipitates are also very small and their inter-precipitate distance is approximately equal to the size of the precipitates (Table 4-5), their diffusion fields overlapped causing inter-necking between them as shown in Figure 4-21a and Figure 4-21b.

Langer-Schwartz [253] explained this mechanism using phase-field modelling. The model incorporated the strain, diffusion fields around the precipitates and overlapping diffusion field parameters to predict a microstructure, which was similar to that found experimentally. Both low diffusivity and high nucleation density impedes the γ' growth and maintains the spherical morphology. The high undercooling prevents further nucleation and growth even though a non-equilibrium condition exists in the system. Hence, the monomodal distribution of the γ' precipitates was observed.

In contrast, the results for the slowest cooled condition (specimen E) suggest a different mechanism. These precipitates nucleate at high temperatures and have higher diffusion rates and lower undercooling compared those of specimen B, where diffusion rates are slow. This allows equilibrium to be established at the γ/γ' interface resulting in near equilibrium precipitate composition. The nucleation rate decreases at high temperature resulting in a lower volume fraction of precipitates and thus an increase in inter-precipitate distance as was shown in Figure 4-24c and Figure 4-24d.

From Figure 4-25, the composition of the γ' precipitates in specimen B was found to be similar to the thermodynamic equilibrium composition predicted from JMatPro, which is shown in Figure 5-2. From Figure 5-2, it is clear that the Al concentration does not vary much (5.98 wt.% to 6.1wt.%) as a function of temperature (700 – 1135°C), whereas the gamma forming elements such as Co and Cr decrease with decreasing temperature (from 6 and 3.25 wt. % to 4.2 and 2.25 wt. % respectively).

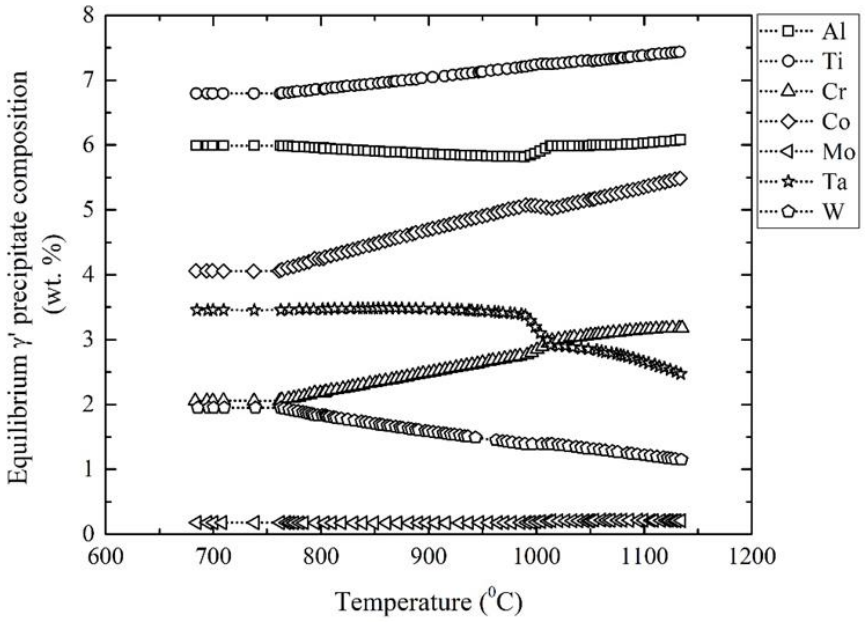

Figure 5-2. JMatPro thermodynamic predicted phase composition for IN738LC showing weight fraction of elements in γ' as a function of temperature.

The composition of the γ' precipitates for specimen B contradicts those found by Chen [254], where the composition of the γ' precipitates in fast cooled specimens (100K/min and 360 K/min) with monomodal precipitate size distribution was reported to have minimal if any compositional variation. This discrepancy is probably due to the slower cooling rates used in the work by Chen [254]. However, in the same work, the tertiary γ' precipitates in a slowly cooled specimen with bimodal precipitate size distribution were reported to have a higher Al content compared to the primary γ' precipitates. This higher Al content was found to be due to the presence of Al-rich antisites in an ordered phase, which occurred by an antisite bridge diffusion mechanism [254].

During slow cooling, the γ' precipitates will grow due to vacancy-mediated diffusion of γ'-forming alloying elements such as Al and Ti. Local equilibrium between the γ and γ' is maintained at the γ'/ γ interface due to a decrease in time at each temperature; this decreases the diffusion distance. Under this condition, the composition distant from the precipitate will not reach equilibrium. Since the time at each temperature is limited during cooling, it becomes difficult to achieve the equilibrium volume fraction of precipitates; the precipitate can maintain equilibrium with the matrix not more than a few tens of nanometers from the interface [255], [256]. At high temperature, the diffusivities of the elements are high, which results in diffusion fields overlapping between the adjacent γ' precipitates. Additionally, there will not be sufficient driving force for new nucleation to occur between these precipitates.

The slow-cooled γ' precipitates displayed deviation from the equilibrium concentration, i.e., 4.5 ± 0.3 wt.% of Al (Figure 4-25) vs 6.1 ± 0.9 wt.% of Al at equilibrium (JMatPro-Figure 5-2). From Figure 4-25, it is clear that a decrease in cooling rate decreased the Al concentration in the γ' precipitates. In contrast, the decrease in cooling rate (i.e. larger γ' precipitates) increased the

concentration of γ-forming elements such as Co and Cr in larger γ' precipitates. The non-equilibrium compositions can be attributed to the low Al concentration in the slow cooled specimen. However, with increased Al diffusion into a precipitate with further decrease in cooling rate, equilibrium composition could be attained. According to equilibrium defect concentration studies in ordered phases [257], the deviation in precipitate composition is due to the presence of antisite defects, which are accommodated by $Ni_{3+x}Al_{1-x}$, i.e., Ni atoms on Al sites for Ni-rich compositions. Similarly, the formation of larger precipitates during slow cooling was assumed to be due to vacancy-mediated antisite-bridge diffusion of elements such as Co and Cr into the γ' precipitate, resulting in non-equilibrium across the interface [258].

5.5.1. γ' size dependent oxidation kinetics and activation energy

Figure 4-26 and Figure 4-30 illustrated specific mass change as a function of oxidation duration and cycles for specimens A, B, C, D and E after isothermal and cyclic oxidation in air at 750, 850, 900 and 950°C for 150 h. Under both conditions, the specific mass change plots followed parabolic oxidation behaviour throughout the exposure times at all temperatures. This type of oxidation behaviour shows that the migration of reactive elements across the oxide scale is controlled by solid-state diffusion, which follows the parabolic rate law. The rate constant, k_p, is the slope of the specific mass change as a function of square root of oxidation duration curve (equation 15). Table 4-6 and Table 4-7 show that that the slowest cooling rate specimens (D and E) have lower rate constants under both isothermal and cyclic oxidation respectively at all investigated temperatures when compared to the other specimens. The lower rate constants suggest that the oxide scale growth rates for these specimens are relatively slower; this may be attributed to the formation of a dense and continuous protective layer on the surface.

Understanding the effect of activation energy on diffusion characteristics of an alloy will help in designing better oxidation resistant materials and predicting their degradation behaviour. The migration of anions and cations through an oxide scale is a diffusion-controlled process and is affected by temperature. The effect of temperature on diffusion can be expressed using the Arrhenius equation where the activation energy associated with the oxidation behaviour may be determined by considering that the temperature dependence of the parabolic rate constant, k_p, follows an Arrhenius-type expression [259]:

$$k_{\mathrm{P}} = k_o \cdot exp^{(-Q/R \cdot T)} \tag{41}$$

where k_P is the parabolic rate constant ($mg^2\ cm^{-4}\ s^{-1}$), k_o is exponential constant, Q is the activation energy ($kJ\ mol^{-1}$), R is gas constant and T is temperature (K). The activation energy can then be calculated by plotting the different rate constants as a function of inverse temperature as shown in Figure 5-3; a summary of the calculations is given in Table 5-2. Activation energies, Q for different heat treatment conditions as a function of temperature.

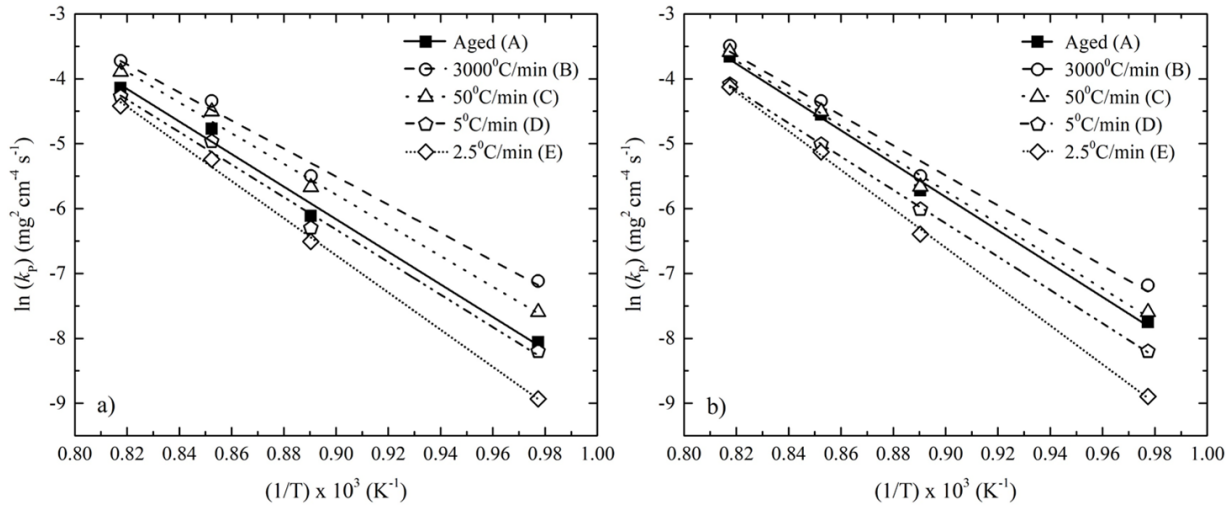

Figure 5-3. Arrhenius temperature dependence of the parabolic rate constants a) isothermal oxidation and b) cyclic oxidation.

Table 5-2. Activation energies, Q for different heat treatment conditions as a function of temperature.

Heat treatment condition	Activation energy (kJ/mol.) for scale growth	
	Isothermal oxidation	Cyclic oxidation
Aged (A)	209	214
3000°C/min (B)	180	192
50°C/min (C)	197	209
5°C/min (D)	208	214
2.5°C/min (E)	238	249

The activation energy required for specimen B during isothermal oxidation at 750-950°C was 180 kJ/mol., whereas specimen E exhibited a higher activation energy of 238 kJ/mol. for the same temperature range. A similar trend was followed during cyclic oxidation; 192 and 249 kJ/mol., respectively. The higher activation energy for the slowest cooled specimen E can be attributed to a slower growth rate due to the presence of a dense and thicker Cr_2O_3 oxide scale on the surface.

Since the volume fraction of γ' precipitates in specimen E was lower than in specimen B (Table 4-4), more matrix is exposed to the oxidising environment. Therefore, the possibility of formation of a continuous external Cr_2O_3 scale is greater in specimen E and hence the higher activation energy obtained for specimen E. Although specimen B contained higher volume fraction of γ' precipitates (70%) compared to specimen B (60%), it did not show a continuous Al_2O_3 scale, either externally or in the subsurface zone.

Hagel and Seybolt [170] reported that the activation energy required for Cr_2O_3 growth as 256 kJ/mol over a temperature range of 1100-1500°C. In the present study, specimen E shows the same range of activation energies under isothermal and cyclic oxidation conditions (238 and 249 kJ/mol., respectively) although the tests were carried out at lower temperatures. Similarly, Al - hatab et al. [174] determined the activation energy for the ternary alloy system, Superni-718 (19Cr-18.5Fe-bal. Ni) at 750, 850 and 950°C for up to 168 h under cyclic conditions in air. The activation energies were found to be 117.516 kJ/mol. at 750-850°C, 249.3 kJ/mol at 850-950°C and 177.543 kJ/mol. at 750-950°C. Chen et al. [260] reported that there was no difference in activation energies for both isothermal and cyclic exposures in air. They reported activation energies of 250, 270 and 300 kJ/mol. for a Ni-based disc of Udimet 720, Astroloy and Waspaloy at 750-1000°C. In the present study, specimen E with a larger γ'/γ interfacial area and lower volume fraction of γ' precipitates was found to have activation energy (Table 5-2) similar to those by Al - hatab [174]and Chen [260]; this suggests that Cr_2O_3 formed on the surface of specimen E is more protective compared to those of specimens A and B.

5.5.2. Effect of γ' intermetallic size on γ' precipitate free zone

Approximately 50-60 γ' PFZ thickness measurements were taken at 5-6 different locations on the same sample using the SEM distance measurement feature. The γ' PFZ thickness of both isothermal and cyclic oxidation specimens are summarised in Table 5-3. The subsurface degradation during isothermal oxidation was minimum compared to that of cyclic oxidation conditions, therefore, only cyclically oxidized specimens were considered to understand the effect of γ' precipitate size at the subsurface level. The γ' PFZ thickness profiles for samples after cyclic oxidation at different temperatures are shown in Figure 5-4. Under all conditions, near-parabolic

behaviour was followed. The relationship between the depth of γ' PFZ and the parabolic rate constant is given by [7]:

$$D_{PFZ}{}^2 = k_p \cdot t \tag{42}$$

where, D_{PFZ} is the depth of γ' PFZ (μm), k_p is the parabolic rate constant ($\mu m^2 s^{-1}$) and t is the oxidation duration (s). The parabolic rate constants for γ' PFZ were determined using the above relationship and are summarised in Table 5-4. This revealed that specimen B with the smallest precipitate size exhibited a higher rate of precipitate dissolution creating thicker γ' PFZ at all temperatures than that of specimen E.

Table 5-3. The depth of γ' PFZ (95% confidence level) measured from the scale/alloy interface to matrix under different heat treatment conditions at different temperatures for isothermal and cyclic oxidation.

Oxidation type	Temperature (°C)	γ' PFZ thickness (μm)				
		A	B	C	D	E
Isothermal	850	1.24 ± 0.04	2.64 ± 0.06	1.9 ± 0.08	1.09 ± 0.03	1.03 ± 0.05
	900	3.11 ± 0.26	3.88 ± 0.03	3.28 ± 0.04	2.68 ± 0.08	2.1 ± 0. 05
	950	3.63 ± 0.39	4.62 ± 0.03	4.1 ± 0.05	3.26 ± 0.03	3.03 ± 0.06
Cyclic	750	1.12 ± 0.05	2.15 ± 0.06	1.56 ± 0.09	0.54 ± 0.04	0.25 ± 0.02
	850	5.1 ± 0.05	7.27 ± 0.17	6.27 ± 0.12	4.31 ± 0.1	4.03 ± 0.15
	900	16 ± 0.03	18.4 ± 0.08	16.2 ± 0.05	10.8 ± 0.1	9.89 ± 0.13
	950	17.4 ± 0.26	22.1 ± 0.24	21.6 ± 0.26	15.3 ± 0.27	14 ± 27

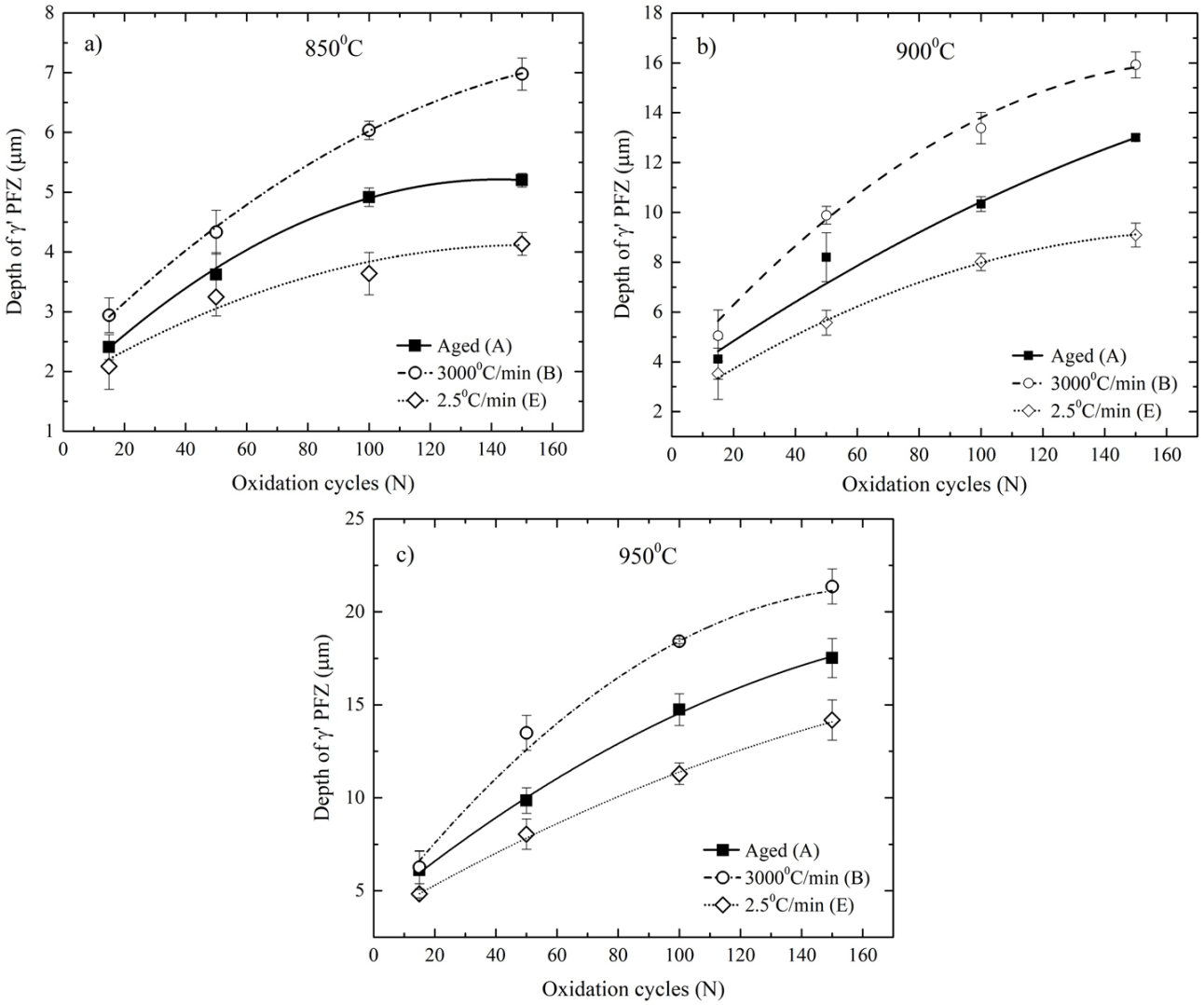

Figure 5-4. Plots of γ' PFZ depth as a function of oxidation cycles for specimens A, B and E at a) 850°C, b) 900°C and c) 950°C.

Table 5-4. Parabolic rate constants for depth of γ' PFZ for specimens A, B and E after 150 cycles of oxidation.

Temperature (°C)	Parabolic rate constants, k_p ($\mu m^2 s^{-1}$)		
	A	B	E
850	1.92E-25	3.03E-25	8.82E-26
900	1.08E-24	1.67E-24	5.34E-25
950	1.93E-24	3.07E-24	1.31E-24

Internal oxidation results when an alloying element is selectively oxidized but cannot reach the surface quickly enough to develop an external scale. In the present study, both the external scale and IOZ growth kinetics obeyed the parabolic rate law and the rate constants decreased with an increasing exposure duration due to increase in the depth of the IOZ and an increase in the external scale thickness. The external scale exhibits continuity in an extremely short time, therefore the oxygen potential at the scale-alloy interface is controlled by the metal-metal oxide equilibrium [114]. Many researchers including Wagner [114] and Maak [261] have studied the internal oxidation mechanism and its kinetics [262]–[264]. In particular, Rhines et al. [262] reported that the extent of internal oxidation in the presence of an external scale depends on the partial pressure of oxygen. The authors also noted that the internal oxidation kinetics in a dilute alloy system was a function of time and followed a parabolic relationship [262]. The results of the current study agree with the results of other chromia-forming alloys as reported by a number of researchers [24], [85], [265].

From Figure 4-28 and Figure 4-31, it is also clear that precipitate dissolution occurs much faster than the internal oxidation, which is evidenced by the presence of a γ' PFZ. The precipitate dissolution in the subsurface zone is attributed to the selective oxidation of Al from the precipitates; this led to a much thicker γ' PFZ in specimen B compared to those of specimens A and E. This may be due to the relatively lower volume fraction of γ' precipitates found in specimens A (58%) and E (60%) resulting in more exposure of the γ-matrix to the oxidizing environment, which subsequently causes more Cr_2O_3 to form on the surface of the substrate. In contrast, in specimen B, approximately 70% of the area was covered with γ' precipitates and therefore, the oxidation of this specimen depleted more Al from the γ' precipitates as well as the matrix to form discontinuous finger-like Al_2O_3 to a greater depth. This can be seen in Figure 4-31e), f), g) and h).

The degree of internal oxidation is dependent on diffusion of oxygen ions into the bulk material. Activation energies calculated from external oxidation parabolic rate constants for specimens A, B and E can be used to assess the depth of internal oxidation. To understand the relationship between the outer oxide scale and the depth of γ' PFZ, the activation energy for the γ' dissolution zone must be measured. The temperature dependency of internal oxidation (depth of γ' PFZ) is shown in Figure 5-5, which is an Arrhenius plot. The activation energies were obtained from the slope of the ln (k_p) vs (1/T) curve and tabulated in Table 5-5. From Figure 5-5, the activation energies for specimens A and B were found to be similar at 279 and 278 kJ/mol., whereas specimen E revealed a higher activation energy. Although specimen A has a wide range of precipitate sizes, more than 60% of the γ' precipitates (secondary γ') are less than 300 nm. Hence, the activation energy for the formation of γ' PFZ in the standard aged condition is similar to that of specimen B. These results (relatively higher activation energy values for specimens with larger γ' precipitate size) mirror those given in Table 4-7 for scale growth and interdependence of oxidation kinetics on precipitate size.

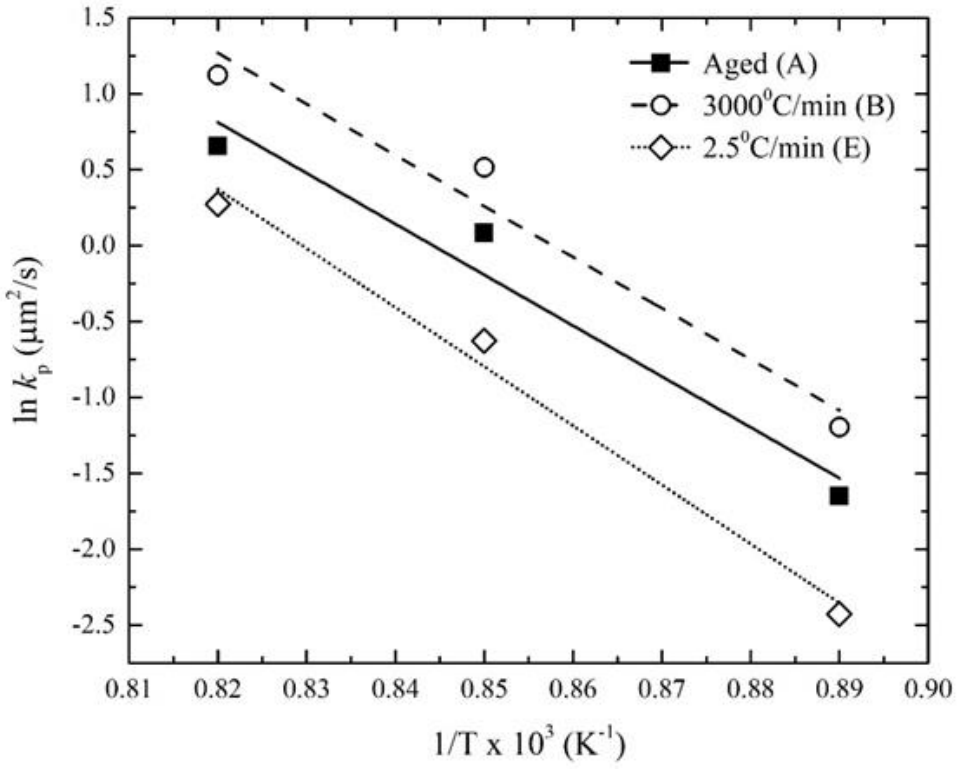

Figure 5-5. Arrhenius plot for standard aged, 3000°C/min and 2.5°C/min specimens.

Table 5-5. Summary of activation energies for specimens A, B and E from Figure 5-5.

Activation energy, Q (kJ/mol.) for PFZ		
A	B	E
279	278	324

5.5.3. Interdiffusion-coefficient of aluminum

The cyclically oxidised specimens were subjected to SEM-EDS analysis to obtain the Al depletion profiles in the subsurface zone, where the distance measured is from the PFZ into the bulk material. Figure 5-6 illustrates profiles for specimens B and E after 150 h of isothermal oxidation at 850, 900 and 950°C. This figure demonstrates that the concentration of Al drops from the bulk material to γ' PFZ (below the Al-rich finger-like oxide phase) at all three temperatures. Also, the Al depletion zone in specimen B was thicker with a flatter composition profile than for specimen E.

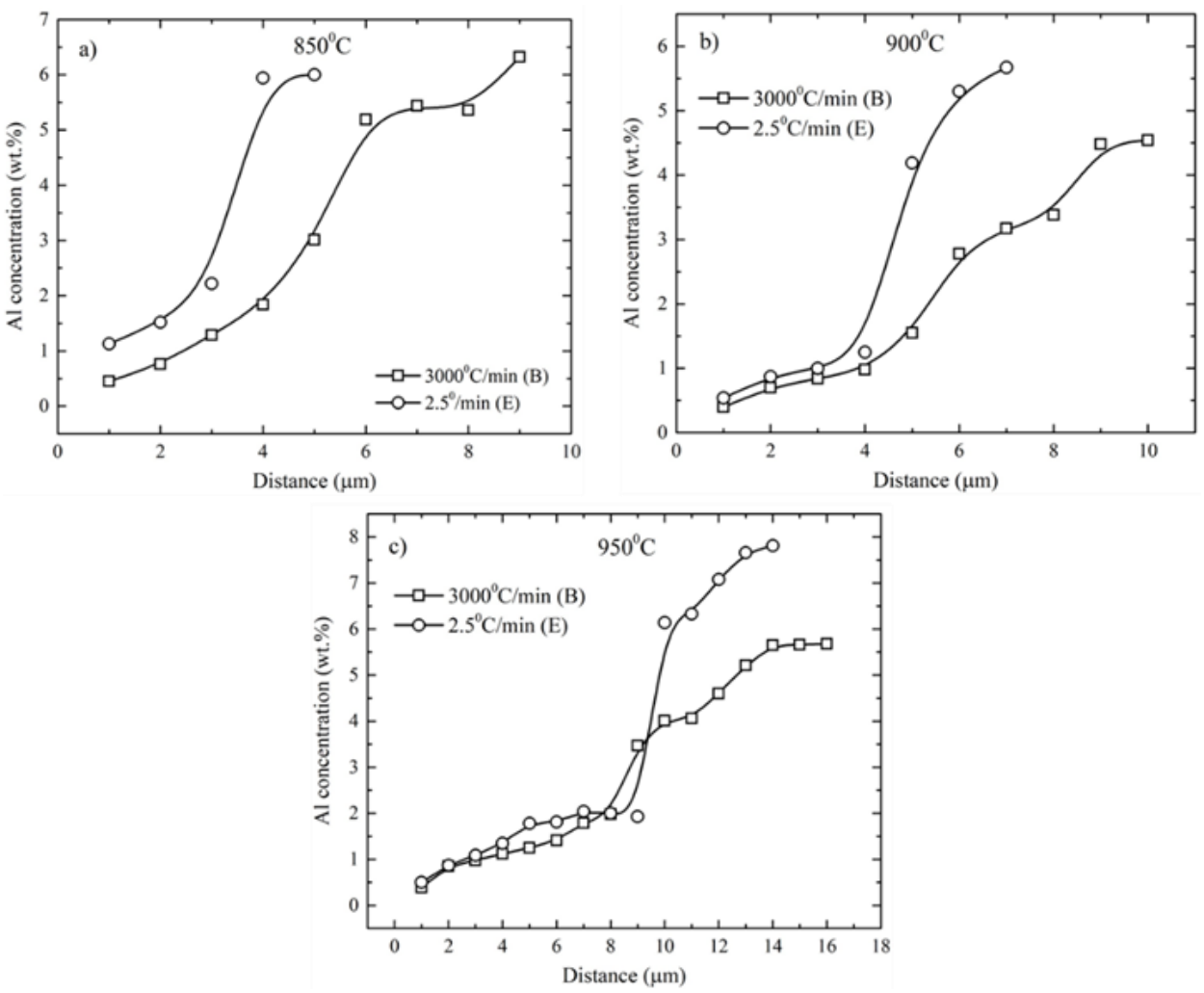

Figure 5-6. Subsurface Al profiles for specimens B and E at a) 850°C, b) 900°C and c) 950°C.

To obtain more information about the oxidation mechanism in the subsurface zone, the average interdiffusion coefficient of Al was determined using the Dayananda model [266]. The relationship is given by,

$$\widetilde{D} = -\frac{1}{2 \cdot t} \cdot \frac{dx}{dC}\Big|_C \int_{C_1}^{C_2} x \cdot dC \tag{43}$$

where C_2 is the measured Al concentration in the bulk material, C_1 is the Al concentration at the γ' PFZ (below the Al-rich finger-like oxide phase), x is the Matano plane and t is a time of oxidation duration. In this study, the average interdiffusion coefficient of Al, $\widetilde{D_{Al}}$, was determined for specimens B and E at 850, 900 and 950°C; these are reported in Table 5-6.

Table 5-6. The average interdiffusion coefficient, ($\widetilde{D_{Al}}$) of Al for specimens B and E as determined from subsurface depletion profiles after 150 h of cyclic oxidation at three different temperatures.

Specimen	Average interdiffusion coefficient ($\widetilde{D_{Al}}$) after 150 h of oxidation (m^2/s)		
	850°C	900°C	950°C
B	1.78E-18	4.06E-18	4.38E-17
E	3.09E-19	6.37E-19	3.54E-18

The calculated interdiffusion coefficients ($\widetilde{D_{Al}}$) for specimens B and E are compared with literature values as shown in Figure 5-7. Included are the results estimated by Watanabe et al.[267], Cserhati et al.[268] and Ikeda et al.[269]. The estimations made by Ikeda et al.[269] and Watanabe et al.[267] are significantly higher than the results of this study. It is considered that the difference is due to the Al concentration. In particular, Ikeda et al. [269] deduced the equation to calculate ($\widetilde{D_{Al}}$) on the basis of 24 at% Al. However, the estimation of ($\widetilde{D_{Al}}$) made by Cserhati et al.[268], using a Ni and Al diffusion couple sample is somewhat higher than the results of specimen E, but it is very close to the values of specimen B.

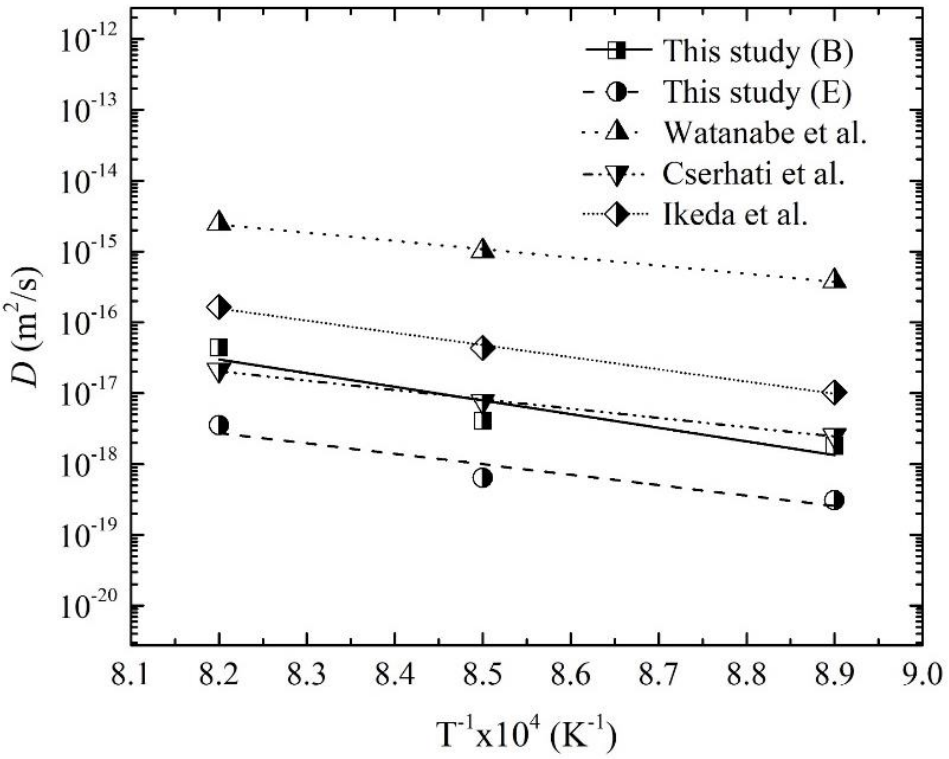

Figure 5-7. Plots of the $\widetilde{D_{Al}}$ estimated in this study compared to those of, $\widetilde{D_{Al}}$ in Ni/Ni₃Al diffusion couple by Watanabe et al.[267], *$\widetilde{D_{Al}}$ in Ni₃Al system by Cserhati et al.*[268] *and $\widetilde{D_{Al}}$ in Ni₃Al system by Ikeda et al.*[269].

From Table 5-6, the larger $\widetilde{D_{Al}}$ in specimen B can be attributed to the following factors. First, the smaller γ' precipitates (specimen B ~ 6.2 wt. % Al) exhibit a higher concentration gradient from γ' precipitate/matrix interface into the matrix resulting in an increase in the rate of Al diffusion from γ' to γ, whereas the larger γ' precipitates (specimen E ~4.1 wt.% Al) showed a lower diffusion rate due to lower concentration gradient. Secondly, the time for complete dissolution of the γ' precipitates increases with increase in size, as the number of Al atoms required to diffuse from the precipitate increases. Furthermore, the γ/γ' interfacial area available for diffusion of alloying elements has been shown to significantly increase the rate of diffusion [153], [270]. In this study, the higher $\widetilde{D_{Al}}$ in specimen B compared to specimen E may be attributable to both smaller precipitate sizes and larger γ/γ' interfacial area in the former. As a result, the presence of smaller precipitates will negatively influence the overall oxidation kinetics.

5.5.4. Influence of γ' size on corrosion performance

Ni-based superalloys exhibit excellent corrosion resistance due to the formation of passive layers such as Cr_2O_3 and Al_2O_3. However, the corrosion resistance can vary depending on the corrosive environment or corrosive medium. For instance, the alloy can perform well in a chloride-free electrolyte but show severe corrosion in a chloride-containing solution. Therefore, knowledge of the chemical composition of the alloy is critical to understand the formation of passive films and subsequent corrosion behaviour. In chromium-containing alloys, it is often observed that the external layer is mainly Ni-hydroxides over an inner chromium-rich oxide layer [271]. The amount of chromium present in the alloy plays a significant role in corrosion performance. Craig et al. [133] suggested that an alloy should contain a minimum of 10.5 wt. % Cr to exhibit corrosion resistance and a further increase in chromium will enhance the corrosion resistance. The alloy used

for the present study, IN738LC consisted of 16 wt. % chromium, which is high enough to provide a good corrosion resistance. Previous studies revealed that IN738LC is a chromia former with multiple oxide layer formation [26].

The electrochemical behaviour of a Ni-based superalloy is complex and is highly dependent on composition, size, area/volume fraction and the morphology of the γ' precipitates. To understand the influence of these factors, potentiodynamic tests were conducted on IN738LC and the results were shown in Figure 4-32. The specimens described earlier as derived from different cooling rates of 3000 (specimen B) and 2.5°C/min (specimen E) displayed a high corrosion resistance in sulphate medium (H_2SO_4) compared to chloride media (NaCl and HCl). In the present study, the corrosion current density was strongly influenced by the size and area/volume fraction of the γ' precipitates indicating a decrease in the precipitate size increased the corrosion rate. It was also noted that the composition of γ' precipitates had influenced the corrosion performance.

Since the γ-matrix contains more chromium than the γ' precipitates, the matrix exhibits more corrosion resistance than the γ' precipitates. Some studies have shown that an increase in Al content can have a negative influence on the corrosion resistance. For example, Castadena et al. [272] and Osorio et al. [200] showed that an increase in Al content decreases the corrosion resistance in Ni-Fe-Al and Fe-Al alloys respectively by forming localised corrosion such as pitting. In the present work, both Al content (6.1 ± 0.9 wt. %) and precipitate number density (84 ± 3.27 precipitates/μm^2) in a specimen cooled at 3000°C/min was higher than that found in a slow cooled specimen (2.5°C/min) with Al of 4.5 ± 0.3 wt. % and precipitate number density of 12800 ± 500 precipitates/μm^2. Hence, specimen B with the smaller γ' precipitates would be more susceptible to corrosion than specimen E with larger γ' precipitates.

Chapter 6 Summary and Conclusions

6.1. Effect of alloying elements and microstructure

- Based on cyclic oxidation experiments of all three alloys, N5, an alumina former, exhibited excellent oxidation resistance under cyclic conditions compared to chromia-forming IN738LC and Rene 80. The calculated rate constants as determined from the data revealed that the N5 oxidation resistance for the entire 1000 cycles was two orders of magnitude higher than for the chromia-forming alloys. The COSP-Monte Carlo model developed by NASA was found to be useful to predict the rate constants and scale spallation constants of IN738LC by showing a good fit for the experimental data. However, the model was less applicable for Rene 80 and N5 due to severe scale spallation after 700 cycles in Rene 80 and spall/rejuvenation cycles of N5.
- The IN738LC and Rene 80 alloys exhibited a significant increase in the rate of surface oxide growth compared to N5, due to the presence of Ti. The oxide scale thickness before scale spallation was found to be ~6 μm and ~8 μm corresponding to the Ti concentration in the alloys IN738C and Rene 80 respectively, whereas N5, with no Ti, exhibited a slow growth rate with ~2 μm of oxide scale.
- Rene 80 exhibited poor scale adherence. The presence of high levels of Mo (4 wt. %) in Rene 80 relative to the other alloys significantly affected the scale spallation rate. Severe scale spallation during cyclic oxidation of IN738LC and Rene 80 resulted in grain boundary oxidation followed by initiation of grain boundary cracking. Most of the scale spallation in N5 was due to the oxidation of large eutectic regions that contained Ta-Hf

carbides on the surface. The shear strain generated at the matrix scale/oxy-carbide interface resulted in the scale spallation.

6.2. Effect of cooling rate

- The microstructural and compositional analyses suggest that cooling rate influences the γ′ precipitate size, morphology and composition. The γ′ precipitate size was found to decrease with an increase in cooling rate due to limited diffusion time and reduction in transportation of γ′ forming alloying elements.
- Compositionally, the smaller precipitates were found to be richer in Al than the larger precipitates, which can be attributed to the presence of Cr and Co-rich antisite defects.
- The WQ specimen (3000°C/min) with small spherical γ′ precipitates (50 nm) was found to have a higher corrosion current density compared to the slow cooled specimen (2.5°C/min) with larger cuboidal precipitate (800 nm).

6.3. Effect of γ' precipitate size

- Both isothermal and cyclic oxidation studies conducted on IN738LC samples (four sizes γ'; monomodal distribution) over a temperature range of 750-950°C in ambient air for up to 150 h showed that oxidation is precipitate-size dependent. All test specimens followed typical parabolic oxidation behaviour under both conditions. The specimen consisting 50±5 nm γ' precipitate size was found to be the least oxidation resistant at all temperatures followed by 150±10 nm, standard aged (~274 nm), 450±5 nm and 800 nm. The low oxidation resistance in the 50±5 nm γ' precipitate size specimen was attributed to the formation of a thin external oxide layer and severe internal oxidation.

- The γ' PFZ depth at all temperatures was dependent on the precipitate size; smaller precipitates gave an extensive PFZ. The activation energy for γ' PFZ formation was found to be highest in the specimen consisting 800±10 nm γ' precipitate size, 324 kJ/mol. and values for the 50±5 nm and standard aged specimens were 278 and 279 kJ/mol. respectively. The lower concentration gradient due to lower Al content in larger γ' and lower γ/γ' interfacial area decreased the γ' dissolution rate in 800±10 nm γ' precipitate size specimens, thereby increasing the activation energy. This suggests that the larger precipitates will decrease the oxidation rate by decreasing the internal oxidation rate.
- It was found that the interdiffusion coefficient of Al, ($\widetilde{D_{Al}}$), across the γ' PFZ depends on the γ' precipitate size and composition. High Al contents and small γ' size will increase the value of ($\widetilde{D_{Al}}$) suggesting a higher γ' dissolution rate. An increase in Al concentration in the precipitates will increase the concentration gradient, which results in a relatively higher diffusion coefficient of Al and subsequent increase in oxidation rate.
- The WQ specimen (3000°C/min) with small spherical γ′ precipitates (50 nm) was found to have a higher corrosion current density compared to the slow cooled specimen (2.5°C/min) with larger cuboidal precipitate (800 nm). The improvement in corrosion resistance for the 2.5°C/min specimen was attributed to an increase in inter-precipitate distance that exposed more matrix to the corrosive environment and a decrease in volume fraction of γ′ precipitates.
- The improvement in corrosion resistance for specimens cooled at the rate of 2.5°C/min (800 nm size) compared to 3000°C/min (50 nm size) was attributed to an increase in inter-precipitate distance that exposed more matrix to the corrosive environment and a decrease in area fraction of γ′ precipitates.

Chapter 7 Suggestions for Future work

1. Residual stress measurements in the oxide scales in all three alloys using X-ray diffraction (XRD) and incorporation of these stresses in COSP modelling to predict the oxidation rate and scale spallation should be investigated.
2. The effect of scale/oxy-carbide interfacial stress on scale spallation should be studied using FEM.
3. An investigation of the effect of different precipitate sizes produced by continuous cooling at different rates on the isothermal and cyclic oxidation behaviour of other materials should be examined.
4. A thorough investigation of dissolution rate of different γ' sizes should be examined.

Chapter 8 References

[1] R. C. Reed, *The superalloys - Fundamentals and applications*. London: Cambridge University Press, 2006.

[2] J. L. Smialek and G. H. Meier, *Superalloys II*. New York: Wiley-Interscience, 1987.

[3] N. Birks, G. H. Meier, and F. S. Pettit, *Introduction to the high-temperature oxidation of metals*, Second Edi. Cambridge: Cambridge University Press, 2006.

[4] G. M. Ecer and G. H. Meier, "Oxidation of high-chromium Ni-Cr alloys," *Oxid. Met.*, vol. 13, no. 2, pp. 119–158, 1979.

[5] R. Eriksson, "Thermal barrier coatings: Durability assessment and life prediction," Linkoping University, 2013.

[6] J. D. Osorio, A. Toro, and J. P. Hernández-ortiz, "Thermal barrier coatings for gas turbine applications: Failure mechanisms and key microstructural features," *Dyna*, vol. 176, pp. 149–158, 2012.

[7] D. J. Young, *High temperature oxidation and corrosion of metals*, Second Edi. Elsevier Science S.A., 2008.

[8] W. Betteridge and S. W. K. Shaw, "Development of superalloys," *Mater. Sci. Technol.*, vol. 3, no. 9, pp. 682–694, 1987.

[9] C. T. Sims, N. S. Stoloff, and W. C. Hagel, *Superalloys II: High-temperature materials for aerospace and industrial power*. New York: John Wiley and Sons, 1987.

[10] D. D. Krueger, K. Robert D, R. G. Menzies, and C. S. Wukusick, "Fatigue crack growth resistant nickel-base article and alloy and method for making," United States Patent, Patent no. 4,957,567, 1990.

[11] B. Gleeson, "The long-term, cyclic-oxidation behavior of selected chromia-forming alloys," *Oxid. Met.*, vol. 49, pp. 373–399, 1998.

[12] R. C. Reed, *The superalloys fundamentals and applications*. New York: Cambridge, 2006.

[13] H. T. Mallikarjuna, W. F. Caley, and N. L. Richards, "High temperature oxidation kinetics and oxide scale characterization of nickel-based superalloy IN738LC," *J. Mater. Eng. Perform.*, vol. 26, no. 10, pp. 4838–4846, 2017.

[14] R. J. Christensen, D. M. Lipkin, and D. R. Clarke, "The stress and spalling behavior of the oxide scale formed on polycrystalline Ni3Al," *Acta Materialia*, vol. 44, no. 9. pp. 3813–3821, 1996.

[15] M. Schiitze, "Mechanical properties of oxide scales," *Oxid. Met.*, vol. 44, no. 1/2, pp. 29–61, 1995.

[16] G. S. Chen, M. Gao, and R. P. Wei, "Microconstituent-induced pitting corrosion in aluminum alloy 2024-T3," *Corrosion*, vol. 52, no. 1, pp. 8–15, 1996.

[17] N. Birbilis and R. G. Buchheit, "Electrochemical characteristics of intermetallic phases in aluminum alloys," *J. Electrochem. Soc.*, vol. 152, no. 4, p. B140, 2005.

[18] Z. Szklarska-Smialowska, "Pitting corrosion of aluminum," *Corros. Sci.*, vol. 41, no. 9, pp. 1743–1767, 1999.

[19] M. Wenderoth, L. A. Cornish, R. Süss, S. Vorberg, B. Fischer, U. Glatzel, and R. Völkl, "On the development and investigation of quaternary Pt-based superalloys with Ni additions," *Metall. Mater. Trans. A Phys. Metall. Mater. Sci.*, vol. 36, no. 3, pp. 567–575, 2005.

[20] M. Bensch, A. Sato, N. Warnken, E. Affeldt, R. C. Reed, and U. Glatzel, "Modelling of high-temperature oxidation of alumina-forming single-crystal nickel-base superalloys," *Acta Mater.*, vol. 60, no. 15, pp. 5468–5480, 2012.

[21] H. L. Bernstein, “A model for the oxide growth stress and its effect on the creep of metals,” *Metall. Trans. A*, vol. 18, no. 6, pp. 975–986, 1991.

[22] D. J. Young and B. Gleeson, “Alloy phase transformations driven by high-temperature corrosion processes,” *Corros. Sci.*, vol. 44, no. 2, pp. 345–357, 2002.

[23] M. Wenderoth, S. Vorberg, B. Fischer, R. Völkl, and U. Glatzel, “Isothermal oxidation behavior of a precipitation-hardened Pt-based alloys with additions of Al, Cr and Ni,” *Int. J. Mater. Res.*, vol. 98, no. 6, pp. 463–467, 2007.

[24] L. García Fresnillo, A. Chyrkin, T. Hüttel, C. Böhme, J. Barnikel, D. Grüner, F. Schmitz, and W. J. Quadakkers, “Oxide scale formation and subsurface phase transformations during long-term steam exposure of the cobalt base alloy 25,” *Mater. Corros.*, vol. 63, no. 10, pp. 878–888, 2012.

[25] S. L. Semiatin, N. C. Levkulich, A. E. Saurber, D. W. Mahaffey, E. J. Payton, and O. N. Senkov, “The kinetics of precipitate dissolution in a nickel-base superalloy,” *Metall. Mater. Trans. A Phys. Metall. Mater. Sci.*, vol. 48, no. 11, pp. 5567–5578, 2017.

[26] H. T. Mallikarjuna, N. L. Richards, and W. F. Caley, “Isothermal oxidation comparison of three Ni-based superalloys,” *J. Mater. Eng. Perform.*, vol. 26, no. 5, pp. 2014–2023, 2017.

[27] A. Chyrkin, P. Huczkowski, V. Shemet, L. Singheiser, and W. J. Quadakkers, “Sub-scale depletion and enrichment processes during high-temperature oxidation of the nickel base alloy 625 in the temperature range 900-1000°C,” *Oxid. Met.*, vol. 75, no. 3–4, pp. 143–166, 2011.

[28] C. A. Klepser, “Effect of continuous cooling rate on the precipitation of gamma prime in nickel-based superalloys,” *Scr. Metall. Mater.*, vol. 33, no. 4, pp. 589–596, 1995.

[29] M. Li, J. Coakley, D. Isheim, G. Tian, and B. Shollock, “Influence of the initial cooling rate from γ′ supersolvus temperatures on microstructure and phase compositions in a nickel superalloy,” *J. Alloys Compd.*, vol. 732, pp. 765–776, 2018.

[30] R. Rosenthal and D. R. F. West, “Continuous γ' precipitation in directionally solidified IN738 LC alloy,” *Mater. Sci. Technol.*, vol. 15, no. 12, pp. 1387–1394, 1999.

[31] Y. H. Wen, J. P. Simmons, C. Shen, C. Woodward, and Y. Wang, “Phase-field modeling of bimodal particle size distributions during continuous cooling,” *Acta Mater.*, vol. 51, no. 4, pp. 1123–1132, 2003.

[32] Y. Q. Chen, E. Francis, J. Robson, M. Preuss, and S. J. Haigh, “Compositional variations for small-scale gamma prime (γ′) precipitates formed at different cooling rates in an advanced Ni-based superalloy,” *Acta Mater.*, vol. 85, pp. 199–206, 2015.

[33] A. J. Ardell, “Trans-interface-diffusion-controlled coarsening of γ′ precipitates in ternary Ni-Al-Cr alloys,” *Acta Mater.*, vol. 61, no. 20, pp. 7828–7840, 2013.

[34] A. J. Ardell, “The effect of volume fraction on particle coarsening: Theoretical considerations,” *Acta Metall.*, vol. 20, no. 1, pp. 61–71, 1972.

[35] I. M. Edmonds, H. E. Evans, and C. N. Jones, “The role of the γ′ precipitate dispersion in forming a protective scale on Ni-based superalloys at 750°C,” *Oxid. Met.*, vol. 73, no. 1–2, pp. 193–206, 2010.

[36] I. M. Edmonds, H. E. Evans, C. N. Jones, and R. W. Broomfield, “Intermediate temperature internal oxidation in fourth generation Ru-bearing single-crystal nickel-base superalloys,” *Oxid. Met.*, vol. 69, no. 1–2, pp. 95–108, 2008.

[37] Q. Ding, Z. Shen, S. Xiang, H. Tian, J. Li, and Z. Zhang, “In-situ environmental TEM study of γ′-γ Phase transformation induced by oxidation in a nickel-based single crystal superalloy,” *J. Alloys Compd.*, vol. 651, pp. 255–258, 2015.

[38] H. S. Kitaguchi, H. Y. Li, H. E. Evans, R. G. Ding, I. P. Jones, G. Baxter, and P. Bowen, “Oxidation ahead of a crack tip in an advanced Ni-based superalloy,” *Acta Mater.*, vol. 61, no. 6, pp. 1968–1981, 2013.

[39] Y. Chen, R. Prasath Babu, T. J. A. Slater, M. Bai, R. Mitchell, O. Ciuca, M. Preuss, and S. J. Haigh, "An investigation of diffusion-mediated cyclic coarsening and reversal coarsening in an advanced Ni-based superalloy," *Acta Mater.*, vol. 110, pp. 295–305, 2016.

[40] S. C. Choi, H. J. Cho, and D. B. Lee, "Effect of Cr , Co , and Ti additions on the high-temperature oxidation behavior of Ni_3Al," vol. 46, pp. 109–127, 1996.

[41] W. M. V. and N. M. V., "Compatibility of dispersion-strengthened platinum with resistojet propellants," NASA technical paper 2765, Cleveland, OH, 1987.

[42] T. M. Pollock and S. Tin, "Nickel-based superalloys for advanced turbine engines: chemistry, microstructure and properties," *J. Propuls. Power*, vol. 22, no. 2, pp. 361–374, 2006.

[43] I. Gurrappa, "Influence of alloying elements on hot corrosion of superalloys and coatings: necessity of smart coatings for gas turbine engines," *Mater. Sci. Technol.*, vol. 19, no. 2, pp. 178–183, 2003.

[44] F. R. L., "Substitutional solution hardening," *Acta Metall.*, vol. 1, pp. 203–209, 1963.

[45] Y. Oya, U. Mishima, and T. Suzuki, "$L1_2 \leftrightarrow DO_C$ Martensitic transformation in Pt_3Al and Pt_3Ga," *J. Metall.*, vol. 78, no. 7, pp. 485–490, 1987.

[46] A. J. McAlister and D. J. Kahan, "The Al-Pt (Aluminum-platinum) system," *Bull. Alloy Phase Diagrams*, vol. 7, p. 45, 1986.

[47] G. J. Tatlock and T. J. Hurd, "Platinum and the oxidation behavior of a nickel based superalloy," *Oxid. Met.*, vol. 22, no. 5–6, pp. 201–226, 1984.

[48] R. A. Ricks, A. J. Porter, and R. C. Ecob, "The growth of γ′ precipitates in nickel-base superalloys," *Acta Metall.*, vol. 31, no. 1, pp. 43–53, 1983.

[49] A. Chiba, S. Hanada, and S. Watanable, "Effect of γ and γ′ former doping on ductility of Ni_3Al," *Scr. Metall. Mater.*, vol. 25, pp. 303–307, 1991.

[50] S. Ochial, Y. Oya, and T. Suzuki, "Alloying behaviour of Ni_3Al, Ni_3Ga, Ni_3Si and Ni_3Ge," *Acta Metall.*, vol. 32, no. 2, pp. 289–298, 1984.

[51] B. C. Wilson and G. E. Fuchs, "The effect of composition, misfit, and heat treatment on the primary creep behavior of single crystal nickel base superalloys PWA 1480 and PWA 1484," in *Superalloys 2008*, 2008, pp. 149–158.

[52] K. S. Chan and R. A. Page, "Inelastic deformation and dislocation structure of a nickel alloy: Effects of deformation and thermal histories," *Metall. Trans. A, Phys. Metall. Mater. Sci.*, vol. 19 A, no. 10, pp. 2477–2486, 1988.

[53] M. V. Nathal, R. A. MacKay, and R. V. Miner, "Influence of precipitate morphology on intermediate temperature creep properties of a nickel-base superalloy single crystal," *Metall. Trans. A*, vol. 20, no. 1, pp. 133–141, 1989.

[54] M. J. Kaufman, P. W. Voorhees, W. C. Johnson, and F. S. Biancaniello, "An elastically induced morphological instability of a misfitting precipitate," *Metall. Trans. A*, vol. 20, no. 10, pp. 2171–2175, 1989.

[55] A. E. Nielsen, "Kinetics of precipitation.," *Angew. Chemie*, vol. 77, no. 16, p. 745, 1965.

[56] D. A. Porter and K. E. Easterling, *Phase transformations in metals and alloys*, Second. London: Chapman and Hall, 1992.

[57] A. K. Jena and M. C. Chathurvedi, *Phase transformations in materials*. Englewood Cliffs, N.J: Prentice Hall, 1992.

[58] J. W. Cahn and J. E. Hilliard, "Free energy of a nonuniform system. III. Nucleation in a two-component incompressible fluid," *J. Chem. Phys.*, vol. 31, no. 3, pp. 688–699, 1959.

[59] K. E. Yoon, R. D. Noebe, and D. N. Seidman, “Effects of rhenium addition on the temporal evolution of the nanostructure and chemistry of a model Ni-Cr-Al superalloy. I: Analysis of the coarsening behavior,” *Acta Mater.*, vol. 55, no. 4, pp. 1159–1169, 2007.

[60] K. E. Yoon, R. D. Noebe, and D. N. Seidman, “Effects of rhenium addition on the temporal evolution of the nanostructure and chemistry of a model Ni-Cr-Al superalloy. II: Analysis of the coarsening behavior,” *Acta Mater.*, vol. 55, no. 4, pp. 1159–1169, 2007.

[61] S. S. Babu, M. K. Miller, J. M. Vitek, and S. A. David, “Characterization of the microstructure evolution in a nickel-base superalloy during continuous cooling conditions,” *Acta Mater.*, vol. 49, no. 20, pp. 4149–4160, 2001.

[62] R. Srinivasan, R. Banerjee, G. B. Viswanathan, S. Nag, J. Y. Hwang, J. Tiley, and H. L. Fraser, “The use of advanced characterization to study transitions across solid state interfaces,” *Jom*, vol. 62, no. 12, pp. 64–69, 2010.

[63] E. Balikci and D. Erdeniz, “Multimodal precipitation in the superalloy IN738LC,” *Metall. Mater. Trans. A Phys. Metall. Mater. Sci.*, vol. 41, no. 6, pp. 1391–1398, 2010.

[64] D. Blavette, A. Bostel, and J. M. Sarrau, “Atom-Probe Microanalysis of a Nickel-Base Superalloy,” vol. 16, pp. 1703–1711, 1985.

[65] D. Blavette, E. Cadel, and B. Deconihout, “Role of the atom probe in the study of nickel-based superalloys,” *Mater. Charact.*, vol. 44, no. 1–2, pp. 133–157, 2000.

[66] E. Balikci, A. Raman, and R. a. Mirshams, “Influence of various heat treatments on the microstructure of polycrystalline IN738LC,” *Metall. Mater. Trans. A*, vol. 28A, pp. 1993–2003, 1997.

[67] E. Balikci, R. Ferrell, and A. Raman, “Preferred orientations in the superalloy IN738LC after different aging heat treatments,” *Zeitschrift für Met.*, vol. 90, no. 2, pp. 141–146, 1999.

[68] S. A. Sajjadi, H. R. Elahifar, and H. Farhangi, “Effects of cooling rate on the microstructure and mechanical properties of the Ni-base superalloy UDIMET 500,” *J. Alloys Compd.*, vol. 455, no. 1–2, pp. 215–220, 2008.

[69] J. Mao, K. M. Chang, W. Yang, D. U. Furrer, K. Ray, and S. P. Vaze, “Cooling precipitation and strengthening study in powder metallurgy superalloy Rene88DT,” *Mater. Sci. Eng. A*, vol. 332, no. 1–2, pp. 318–329, 2002.

[70] G. Tian, C. Jia, Y. Wen, G. Liu, and B. Hu, “Cooling γ′ precipitation behavior and strengthening in powder metallurgy superalloy FGH4096,” *Rare Met.*, vol. 27, no. 4, pp. 410–417, 2008.

[71] P. Le Baillif, P. Lamesle, D. Delagnes, V. Velay, C. Dumont, F. Rézaï-Aria, J. Y. Guédou, and J. Choné, “Influence of the quenching rate and step-wise cooling temperatures on microstructural and tensile properties of PER72 (R) Ni-based superalloy,” in *MATEC Web of Conferences*, 2014, vol. 14, p. 21002.

[72] R. J. Mitchell, M. C. Hardy, M. Preuss, and S. Tin, “Development of γ′ morphology in p/m rotor disc alloys during heat treatment,” in *Superalloys 2004 (Tenth International Symposium)*, 2004, pp. 361–370.

[73] T. Grosdidier, A. Hazotte, and A. Simon, “On the dissolution mechanisms of γ′ precipitates in nickel-based superalloys,” *Scr. Metall. Mater.*, vol. 30, no. 10, pp. 1257–1262, 1994.

[74] R. Srinivasan, R. Banerjee, G. B. Viswanathan, S. Nag, J. Y. Hwang, J. Tilley, and H. L. Fraser, “The use of advanced characterization to study transitions across solid state interfaces,” *J. Miner. Met. Mater. Soc.*, vol. 62, no. 12, pp. 64–69, 2010.

[75] P. M. Sarosi, B. Wang, J. P. Simmons, Y. Wang, and M. J. Mills, “Formation of multimodal size distributions of γ′ in a nickel-base superalloy during interrupted continuous cooling,” *Scr. Mater.*, vol. 57, no. 8, pp. 767–770, 2007.

[76] N. El-Bagoury, M. Waly, and A. Nofal, “Effect of various heat treatment conditions on microstructure of cast polycrystalline IN738LC alloy,” *Mater. Sci. Eng. A*, vol. 487, no. 1–2, pp. 152–161, 2008.

[77] N. El-Bagoury and A. Nofal, "Microstructure of an experimental Ni-base superalloy under various casting conditions," *Mater. Sci. Eng. A*, vol. 527, no. 29–30, pp. 7793–7800, 2010.

[78] G. Boussinot, A. Finel, and Y. Le Bouar, "Phase-field modeling of bimodal microstructures in nickel-based superalloys," *Acta Mater.*, vol. 57, no. 3, pp. 921–931, 2009.

[79] P. J. Bocchini, E. A. Lass, K. W. Moon, M. E. Williams, C. E. Campbell, U. R. Kattner, D. C. Dunand, and D. N. Seidman, "Atom-probe tomographic study of γ/γ′ interfaces and compositions in an aged Co-Al-W superalloy," *Scr. Mater.*, vol. 68, no. 8, pp. 563–566, 2013.

[80] J. S. Langer and A. J. Schwartz, "Kinetics of nucleation in near-critical fluids," *Phys. Rev. A*, vol. 21, no. 3, pp. 948–958, 1980.

[81] D. U. Furrer and H. J. Fecht, "γ′ Formation in superalloy U720LI," *Scr. Mater.*, vol. 40, no. 11, pp. 1215–1220, 1999.

[82] H. A. Calderon, P. W. Voorhees, J. L. Murray, and G. Kostorz, "Ostwald ripening in concentrated alloys," *Acta Metall. Mater.*, vol. 42, no. 3, pp. 991–1000, 1994.

[83] I. M. Lifshitz and V. V. Slyozov, "The kinetics of precipitation from supersaturated solid solutions," *J. Phys. Chem. Solids*, vol. 19, no. 1, pp. 35–50, 1961.

[84] C. Z. Wagner, "Theory of precipitate change by redissolution," *Electrochemistry*, vol. 65, pp. 581–591, 2003.

[85] J. H. Chen, P. M. Rogers, and J. A. Little, "Oxidation behavior of several chromia-forming commercial nickel-base superalloys," *Oxid. Met.*, vol. 47, pp. 381–410, 1997.

[86] M. J. Pomeroy, "Coatings for gas turbine materials and long term stability issues," *Mater. Des.*, vol. 26, no. 3, pp. 223–231, 2005.

[87] M. Durand-Charre, *The microstructure of superalloys*. London: CRC Press, 1997.

[88] J. Stringer, "High temperature corrosion of superalloys," *Mater. Sci. Technol.*, vol. 3, no. 7, pp. 482–493, 1987.

[89] D. J. Young and B. A. Pint, "Chromium volatilization rates from Cr_2O_3 scales into flowing gases containing water vapor," *Oxid. Met.*, vol. 66, no. 3–4, pp. 137–153, 2006.

[90] I. Zaplatynsky, "Volatilization of oxides during oxidation of some superalloys at 1200°C," *Oxid. Met.*, vol. 11, no. 6, pp. 289–305, 1977.

[91] M. Pröbstle, S. Neumeier, P. Feldner, R. Rettig, H. E. Helmer, R. F. Singer, and M. Göken, "Improved creep strength of nickel-base superalloys by optimized γ/γ′ partitioning behavior of solid solution strengthening elements," *Mater. Sci. Eng. A*, vol. 676, pp. 411–420, 2016.

[92] B. Wang, J. Zhang, T. Huang, H. Su, Z. Li, L. Liu, and H. Fu, "Influence of W, Re, Cr, and Mo on microstructural stability of the third generation Ni-based single crystal superalloys," *J. Mater. Res.*, vol. 31, no. 21, pp. 3381–3389, 2016.

[93] O. Lavigne, C. Ramusat, S. Drawin, P. Caron, D. Boivin, and J. Pouchou, "Relationships between microstructural instabilities and mechanical behaviour in new generation nickel-based single crystal superalloys AM1 MC632," *Superalloys 2004*, pp. 667–675, 2004.

[94] L. Lirong, C. Maokai, T. Sugui, Z. Zhongyuan, and J. Tao, "Effect of Re content on precipitation behaviour of secondary phases in a single-crystal Ni-based superalloy during high-temperature thermal exposure," *Mater. High Temp.*, vol. 35, no. 4, pp. 355–362, 2018.

[95] E. F. Bradley, *Materials for elevated-temperature applications*. American Society for Metals, 1979.

[96] A. Wagner, B. A. Shollock, and M. McLean, "Grain structure development in directional solidification of nickel-base superalloys," *Mater. Sci. Eng. A*, vol. 374, no. 1–2, pp. 270–279, 2004.

[97] D. A. Ford and R. P. Arthey, “Development of single crystal alloys for specific engine applications,” in *Superalloys 1984 : Proceedings of the Fifth International Symposium on Superalloys*, 1984, vol. 1, pp. 115–124.

[98] E. A. Gulbransen, “Kinetic and structural factors involved in oxidation of metals,” *Ind. Eng. Chem.*, vol. 41, no. 7, pp. 1385–1391, 1949.

[99] F. Gesmundo and B. Gleeson, “Oxidation of multicomponent two-phase alloys,” *Oxid. Met.*, vol. 44, no. 1–2, pp. 211–237, 1995.

[100] P. Kofstad, “On high-temperature oxidation of chromium,” *J. Electrochem. Soc.*, vol. 127, no. 11, p. 2410, 1980.

[101] P. Kofstad, “Defects and transport properties of metal oxides,” *Oxid. Met.*, vol. 44, no. 1/2, pp. 3–27, 1995.

[102] K. R. Lawless, “The oxidation of metals,” *Reports Prog. Phys.*, vol. 37, no. 2, pp. 231–316, 1974.

[103] F. H. Stott, “The protective action of oxide scales in gaseous environments at high temperature,” *Reports Prog. Phys.*, vol. 50, no. 7, pp. 861–913, 1987.

[104] K. Hauffe, *Oxidation of metals*. New York, U.S.A.: Plenum Press, 1965.

[105] P. Kofstad, *High temperature oxidation of metals*. New York, U.S.A.: John Wiley & Son, 1966.

[106] V. O. Kubaschewski and B. E. Hopkins, *Oxidation of metals and alloys*. London: Butterworths Scientific Publications, 1953.

[107] Joseph R. Davis, *ASM specialty handbook: Heat-resistant materials*. Materials Park, OH: ASM International, 1997.

[108] N. Cabrera and N. F. Mott, “Theory of the oxidation of metals,” *Reports Prog. Phys.*, vol. 12, pp. 163–184, 1949.

[109] R. Winston Revie, *Uhlig’s corrosion handbook*, Third edit. NewJersey: John Wiley and Sons, Inc, 2011.

[110] H. Buscail, S. Perrier, and C. Josse, “Oxidation mechanism of the Inconel 601 alloy at high temperatures,” *Mater. Corros.*, vol. 62, no. 5, pp. 416–422, 2011.

[111] F. Gesmundo and F. Viani, “Application of Wagner’s theory to the parabolic growth of oxides containing different kinds of defects: I. Pure oxides,” *J. Electrochem. Soc. SOLID-STATE Sci. Technol.*, vol. 128, no. 2, pp. 460–469, 1981.

[112] Myer Kutz, *Handbook of environmental degradation of materials*. Oxford: Elsevier, 2012.

[113] A. S. Khanna, *Introduction to high temperature oxidation and corrosion*. Materials Park, OH: ASM International, 2002.

[114] C. Wagner, “Theoretical analysis of the diffusion processes determining the oxidation rate of alloys,” *J. Electrochem. Soc.*, vol. 99, no. 10, pp. 369–380, 1952.

[115] F.A.Kroger, “Defects and transport in SiO2, Al2O3 and Cr2O3, in: R. A. Rapp(Ed.), High temperature corrosion,” in *NACE 6, National Association of corroison engineers*, 1983, pp. 89–94.

[116] M. Lannoo and J. Bourgoin, *Point defects in semiconductors I*. New York: Springer, 1981.

[117] P. Andrew, *Introduction to material science*. Cambridge: Cambridge University Press, 1992.

[118] R. J. D. Tilley, *Defects in solids*. New Jersey: John Wiley and Sons, Inc, 2008.

[119] H. Mehrer, *Diffusion in solids*. Berlin, Heidelberg: Springer, 2007.

[120] Paul Shewmon, *Diffusion in solids*, 2nd ed. Gewebestrasse: Springer, 2016.

[121] A. S. Nowick and J. J. Burton, *Diffusion in solids: Recent developments*. New York, U.S.A.: Academic Press, 2012.

[122] D. Clemens, K. Bongartz, W. J. Quadakkers, H. Nickel, H. Holzbrecher, and J. S. Becker, "Determination of lattice and grain boundary diffusion coefficients in protective alumina scales on high temperature alloys using SEM, TEM and SIMS," *Fresenius. J. Anal. Chem.*, vol. 353, no. 3–4, pp. 267–270, 1995.

[123] R. Castillo, A. K. Koul, and J.-P. A. Immarigeon, "The effect of service exposure on the creep properties of cast IN738LC subjected to low stress high temperature creep conditions," *TMS Superalloys*, pp. 805–814, 1988.

[124] R. W. Balluffi, "Grain boundary diffusion mechanisms in metals," *Metall. Trans. B*, vol. 13, no. 4, pp. 527–553, 1982.

[125] F. H. Stott, I. G. Wright, T. Hodgkiess, and G. C. Wood, "Factors affecting the high-temperature oxidation behavior of some dilute nickel- and cobalt-base alloys," *Oxid. Met.*, vol. 11, no. 3, pp. 141–150, 1977.

[126] C. S. Giggins and F. S. Pettit, "Oxidation of Ni - Cr - Al Alloys Between 1000°C and 1200°C," *J. Electrochem. Soc.*, vol. 118, no. 1, pp. 1782–1790, 1971.

[127] M. Schütze and W. J. Quadakkers, "Future directions in the field of high-temperature corrosion research," *Oxid. Met.*, vol. 87, no. 5–6, pp. 681–704, 2017.

[128] A. M. Huntz, L. Marechal, B. Lesage, and R. Molins, "Oxidation of alumina forming materials," in *High Temperature Corrosion and Materials Chemistry IV*, 2003, vol. 2003, no. 16, pp. 18–32.

[129] S. Han and D. John, "Oxidation – Nitridation of Ni-Cr-Al Alloys," vol. 7, no. 1, pp. 11–16, 2004.

[130] P. Kofstad, *High tempearture oxidation of metals*. New York, U.S.A.: Wiley Interscience, 1966.

[131] F. H. Stott, F. I. Gabriel, F. I. Wei, and G. C. Wood, "Development of silicon-containing oxides during the oxidation of Fe-Cr-base alloys," *Werkstoffe und Korrosion*, vol. 38, no. 9, pp. 521–531, 1987.

[132] M. Guerain, J.-L. Grosseau-Poussard, G. Geandier, B. Panicaud, N. Tamura, M. Kunz, C. Dejoie, J.-S. Micha, D. Thiaudière, and P. Goudeau, "Residual stress determination in oxide layers at different length scales combining Raman spectroscopy and X-ray diffraction: Application to chromia-forming metallic alloys," *J. Appl. Phys.*, vol. 122, no. 19, p. 195105, 2017.

[133] B. D. Craig and David S. Anderson, *Handbook of corrosion data*. Materials Park, OH: ASM International, 1995.

[134] D. J. Young, A. Chyrkin, and W. J. Quadakkers, "A simple expression for predicting the oxidation limited life of thin components manufactured from FCC high temperature alloys," *Oxid. Met.*, vol. 77, no. 5–6, pp. 253–264, 2012.

[135] E. P. Busso, H. E. Evans, Z. Q. Qian, and M. P. Taylor, "Effects of breakaway oxidation on local stresses in thermal barrier coatings," *Acta Mater.*, vol. 58, no. 4, pp. 1242–1251, 2010.

[136] A. Chyrkin, N. Mortazavi, M. Halvarsson, D. Grüner, and W. J. Quadakkers, "Effect of thermal cycling on protective properties of alumina scale grown on thin Haynes 214 foil," *Corros. Sci.*, vol. 98, pp. 688–698, 2015.

[137] B. Gleeson, *High-temperature corrosion of metallic alloys and coatings*. New York, U.S.A.: Weinheim: Wiley-VCH, 2013.

[138] R. H. Bricknell and D. A. Woodford, "The mechanism of cavity formation during high temperature oxidation of nickel," *Acta Metall.*, vol. 30, no. 1, pp. 257–264, 1982.

[139] D. Caplan and M. Cohen, "Scaling of Fe - 26Cr alloys at 870°C-1200°C," *J. Electrochem. Soc.*, vol. 112, no. 5, pp. 471–477, 1965.

[140] C. A. C. Sequeira and L. Amaral, "Role of Kirkendall effect in diffusion processes in solids," *Trans.*

Nonferrous Met. Soc. China, vol. 24, no. 1, pp. 1–11, 2014.

[141] K. Fujiwara and Z. Horita, "Measurement of intrinsic diffusion coefficients of Al and Ni in Ni_3Al using Ni/NiAl diffusion couples," *Acta Mater.*, vol. 50, no. 6, pp. 1571–1579, 2002.

[142] S. W. Yang, "Effect of Ti and Ta on the oxidation of a complex superalloy," *Oxid. Met.*, vol. 15, no. 5–6, pp. 375–397, 1981.

[143] B. Li, "Long-term cyclic oxidation behavior of wrought commercial alloys at high temperatures," Ph.D. thesis, Iowa State University, 2003.

[144] F. S. Pettit and G. H. Meier, "Oxidation and hot corrosion of superalloys," in *Superlloys 1984: Proceedings of the Fifth International Symposium on Superalloys*, 1984, pp. 651–687.

[145] G. C. Wood, F. H. Stott, D. P. Whittle, Y. Shida, and B. D. Bastow, "The high-temperature internal oxidation and intergranular oxidation of nickel-chromium alloys," *Corros. Sci.*, vol. 23, no. 1, pp. 9–25, 1983.

[146] B. Gleeson and B. T. Li, "Cyclic oxidation of chromia-scale forming alloys: Lifetime prediction and accounting for the effects of major and minor alloying additions," *Mater. Sci. Forum*, vol. 461–464, pp. 427–438, 2004.

[147] D. J. Young and M. Cohen, "Oxidation behavior of chromium between 300°C and 600°C," *J. Electrochem. Soc.*, vol. 124, no. 5, pp. 769–774, 1977.

[148] F. H. Stott, G. C. Wood, and J. Stringer, "The influence of alloying elements on the development and maintenance of protective scales," *Oxid. Met.*, vol. 44, no. 1–2, pp. 113–145, 1995.

[149] S. Petroni and A. Milosavljević, "Heat treatment effect on multicomponent nickel alloys structure," *FME Trans.*, vol. 35, pp. 189–193, 2007.

[150] P. Carter, D. J. Young, and B. Gleeson, "Calculation of precipitate dissolution zone kinetics in oxidizing binary two-phase alloys," *Acta Mater.*, vol. 44, no. 10, pp. 4033–4038, 1996.

[151] C. Matano, "On the relation between diffusion-coefficients and concentrations of solid metals," *Japanese J. Phys.*, vol. 8, pp. 109–113, 1933.

[152] L. Boltzmann, "To integrate the diffusion equation with variable diffusion coefficients," *Ann. Phys. (N. Y).*, vol. 53, p. 959, 1894.

[153] S. C. Jha, T. H. Sanders, and M. A. Dayananda, "Grain boundary precipitate free zones in Al-Li alloys," *Acta Metall.*, vol. 35, no. 2, pp. 473–482, 1987.

[154] V. Shemet, A. K. Tyagi, J. S. Becker, P. Lersch, L. Singheiser, and W. J. Quadakkers, "The formation of protective alumina-based scales during high-temperature air oxidation of γ -TiAl alloys," *Oxid. Met.*, vol. 54, pp. 211–235, 2000.

[155] H. M. Tawancy and L. M. Al-Hadhrami, "Influence of titanium in nickel-base superalloys on the performance of thermal barrier coatings utilizing γ - γ' platinum bond coats," *J. Eng. Gas Turbines Power*, vol. 133, no. 4, p. 042101, 2011.

[156] A. Atkinson and R. I. Taylor, "Diffusion of 51Cr tracer in Cr_2O_3 and the growth of Cr_2O_3 films," in *Transport in Nonstoichiometric Compounds*, 1985, pp. 285–295.

[157] G. D. Smith and S. J. Patel, "The role of niobium in wrought precipitation-hardened nickel-base alloys," in *Superalloys 718, 625, 706 and Various Derivatives*, 2005, pp. 135–154.

[158] H. Hisazawa, Y. Terada, F. Adziman, D. J. Crudden, D. M. Collins, D. E. J. Armstrong, and R. C. Reed, "The effect of Nb / Ti ratio on hardness in high-strength Ni-based superalloys," *Metals (Basel).*, vol. 71, no. 7, pp. 1–11, 2017.

[159] D. Itzhak, M. Schieber, and F. R. Tuler, "Improved resistance to cyclic oxidation of a nickel-based superalloy by high temperature etching treatment (HTET)," *Corros. Sci.*, vol. 20, no. 3, pp. 413–420, 1980.

[160] S. Tei, M. Hirotoshi, and S. Tatsuya, “Oxygen plasma interactions with molybdenum: Formation of volatile molybdenum oxides,” *J. Plasma Fusion Res.*, vol. 78, no. 1, pp. 3–4, 2001.

[161] F. Zhong, F. Fan, S. Li, and J. Sha, “High-temperature oxidation behaviour of novel Co-Al-W-Ta-B-(Mo, Hf, Nb) alloys with a coherent γ/γ′–dominant microstructure,” *Prog. Nat. Sci. Mater. Int.*, vol. 26, no. 6, pp. 600–612, 2016.

[162] S. Taniguchi, T. Shibata, and H. Tsuruokat, “Isothermal oxidation behavior of Ni_3Al-0.1B base alloys containing Ti, Zr, or Hf additions,” *Oxid. Met.*, vol. 26, no. 3/4, pp. 201–216, 1986.

[163] K. P. Lillerud and P. Kofstad, “On high temperature oxidation of chromium,” *J. Electrochem. Soc.*, vol. 127, no. 11, pp. 2397–2410, 1980.

[164] M. Y. Su and G. Simkovich, “Point defect structure of Cr_2O_3,” Ph.D. thesis, Pennsylvania State University, 1987.

[165] C. Greskovich, “Deviation from stoichiometry in Cr_2O_3 at high oxygen partial pressures,” *J. Am. Ceram. Soc.*, vol. 67, no. 6, pp. 111–112, 1984.

[166] D. F. Mitchell, R. J. Hussey, and M. J. Graham, “Analysis of oxygen isotope interfaces using negative molecular ion SIMS,” *J. Vac. Sci. Technol. A*, vol. 1, no. 2, pp. 1006–1008, 1983.

[167] R. S. Barnes, “Diffusion of copper along the grain boundaries of nickel,” *Nature*, vol. 166, pp. 1032–1033, 1950.

[168] D. G. Lees and J. M. Calvert, “The use of ^{18}O as a tracer to study the growth mechanism of oxide scales,” *Corroison Sci.*, vol. 16, pp. 767–774, 1976.

[169] F. H. Stott, G. C. Wood, Y. Shida, D. P. Whittle, and B. D. Bastow, “The development of internal and intergranular oxides in nickel chromium aluminium alloys at high temperature,” *Corros. Sci.*, vol. 21, no. 8, pp. 599–624, 1981.

[170] W. C. Hagel and A. U. Seybolt, “Cation diffusion in Cr_2O_3,” *J. Electrochem. Soc.*, vol. 108, no. 12, pp. 1146–1152, 1961.

[171] D. P. Whittle, “Spalling of protective oxide scales,” *Oxid. Met.*, vol. 4, no. 3, pp. 171–179, 1972.

[172] B. A. Pint, “Progress in understanding the reactive element effect since the Whittle and Stringer literature review,” Oak Ridge, TN, 1980.

[173] B. Pieraggi and R. A. Rapp, “Chromia scale growth in alloy oxidation and the reactive element effect,” *J. Electrochem. Soc.*, vol. 140, no. 10, pp. 2844–2850, 1993.

[174] K. A. Al-Hatab, M. A. Al-Bukhaiti, U. Krupp, and M. Kantehm, “Cyclic oxidation behavior of IN718 superalloy in air at high temperatures,” *Oxid. Met.*, vol. 75, no. 3–4, pp. 209–228, 2011.

[175] F. H. Stott and G. C. Wood, “The mechanism of oxidation of dilute Ni-Al alloys at 800-1200˚C,” *Corros. Sci.*, vol. 17, pp. 647–670, 1977.

[176] W. E. Boggs, “The high-temperature oxidation resistance of Fe-Si-Al alloys,” *Oxid. Met.*, vol. 10, no. 4, pp. 277–289, 1976.

[177] G. N. Irving, J. Stringer, and D. P. Whittle, “The high-temperature oxidation resistance of Co-Al alloys,” *Oxid. Met.*, vol. 9, no. 5, pp. 427–440, 1975.

[178] B. A. Pint, J. R. Martin, and L. W. Hobbs, “The oxidation mechanism of θ-Al_2O_3 scales,” *Solid State Ionics*, vol. 78, pp. 99–107, 1995.

[179] G. C. Rybicki and J. L. Smialek, “Effect of the θ-α-Al_2O_3 transformation on the oxidation behavior of β-NiAl+Zr,” *Oxid. Met.*, vol. 31, no. 3–4, pp. 275–304, 1989.

[180] E. J. Feltent and F. S. Pettit, “Development, growth, and adhesion of Al_2O_3 platinum-aluminum alloys,” *Oxid.*

Met., vol. 10, no. 3, pp. 189–223, 1976.

[181] H. M. Hindam and W. W. Smeltzer, "Growth and microstructure of α-Al_2O_3 on Ni-Al alloys: Internal precipitation and transition to external scale.," *J. Electrochem. Soc.*, vol. 127, no. 7, pp. 1630–1635, 1980.

[182] J. L. Smialek, "Oxide morphology and spalling model for NiAl," *Metall. Trans. A*, vol. 9, pp. 309–320, 1978.

[183] A. E. Paladino and W. D. Kingery, "Aluminum ion diffusion in aluminum oxide," *J. Chem. Phys.*, vol. 37, no. 5, pp. 957–962, 1962.

[184] J. L. Smialek, "Cyclic oxidation modeling and life prediction," *Mater. Sci. Forum*, vol. 461, no. 1, pp. 663–670, 2004.

[185] H. Hindam and D. P. Whittle, "Microstructure, adhesion and growth kinetics of protective scales on metals and alloys," *Oxid. Met.*, vol. 18, no. 5–6, pp. 245–284, 1982.

[186] G. Beranger, F. Armanet, and M. Lambertin, "Active elements in oxidation and their properties," in *The role of active elments in the oxidation behaviour of high temperature metals and alloys*, 1989, pp. 33–51.

[187] M. Gobel, A. Rahmel, and M. Sehutze, "The isothermal-oxidation behavior of several nickel-base single-crystal superalloys with and without coatings," *Oxid. Met.*, vol. 39, no. 3/4, pp. 231–261, 1993.

[188] B. C. Collins, "Modified PWA 1483 nickel-based superalloy for industrial gas turbine applications," University of Florida, 2007.

[189] L. N. McCartney, "Modelling scale failure in tension (fracture and spallation)," *Mater. High Temp.*, vol. 22, no. 1–2, pp. 167–177, 2005.

[190] E. N'dah, M. P. Hierro, K. Borrero, and F. J. Pérez, "Study of the cyclic oxidation resistance of superalloy IN-625: Lifetime predicted by COSP-modelling program," *Oxid. Met.*, vol. 68, no. 1–2, pp. 9–21, 2007.

[191] C. O. Moon and S. B. Lee, "Analysis on failures of protective-oxide layers and cyclic oxidation," *Oxid. Met.*, vol. 39, no. 1–2, pp. 1–13, 1993.

[192] H. E. Evans and R. C. Lobb, "Conditions for the initiation of oxide-scale cracking and spallation," *Corros. Sci.*, vol. 24, no. 3, pp. 209–222, 1984.

[193] M. Schütze, "Stresses and decohesion of oxide scales," *J. Mater. Sci. Technol.*, vol. 4, no. 5, pp. 407–414, 1988.

[194] K. S. Chan, "A mechanics-based approach to cyclic oxidation," *Metall. Mater. Trans. A*, vol. 28A, pp. 411–422, 1997.

[195] J. L. Smialek and J. V. Auping, "COSP for windows - Strategies for rapid analyses of cyclic-oxidation behavior," *Oxid. Met.*, vol. 57, no. 5–6, pp. 559–581, 2002.

[196] C. E. Lowell, C. A. Barrett, R. W. Palmer, J. V. Auping, and H. B. Probst, "COSP: A computer model of cyclic oxidation," *Oxid. Met.*, vol. 36, no. 1–2, pp. 81–112, 1991.

[197] J. L. Smialek, "A deterministic interfacial cyclic oxidation spalling model," *Acta Mater.*, vol. 51, no. 2, pp. 469–483, 2003.

[198] A. Raffaitin, D. Monceau, E. Andrieu, and F. Crabos, "Cyclic oxidation of coated and uncoated single-crystal nickel-based superalloy MC2 analyzed by continuous thermogravimetry analysis," *Acta Mater.*, vol. 54, no. 17, pp. 4473–4487, 2006.

[199] D. Poquillon and D. Monceau, "Application of a simple statistical spalling model for the analysis of high-temperature, cyclic-oxidation kinetics data," *Oxid. Met.*, vol. 59, no. 3/4, pp. 409–431, 2003.

[200] W. R. Osório, L. C. Peixoto, P. R. Goulart, and A. Garcia, "Electrochemical corrosion parameters of as-cast Al-Fe alloys in a NaCl solution," *Corros. Sci.*, vol. 52, no. 9, pp. 2979–2993, 2010.

[201] L. L. Shreir, R. A. Jarman, and G. A. Burstein, *Corrosion*, 3rd ed. John Wiley & Sons Inc, 1994.

[202] R. M. Hassan and I. A. Zaafarany, "Kinetics of corrosion inhibition of aluminum in acidic media by water-soluble natural polymeric pectates as anionic polyelectrolyte inhibitors," *Materials (Basel).*, vol. 6, no. 6, pp. 2436–2451, 2013.

[203] M. J. N. Pourbaix and N. de Zoubov, *Atlas d'equilibres electrochimiques*. Paris : Gauthier-Villars, 1963.

[204] Z. Ahmad, *Principles of corrosion engineering and corrosion control*. Butterworth-Heinemann, 2006.

[205] M. G. Fontana, *Corrosion engineering*. New York, U.S.A.: McGraw-Hill, 1967.

[206] C. H. Hamann and W. Vielstich, *Elektrochemie / C. H. Hamann; Wolf Vielstich ; 2: Elektrodenprozesse, angewandte Elektrochemie*, 42nd ed. Verl. Chemie [u.a.], 1981.

[207] J. Garche, C. K. Dyer, P. T. Moseley, Z. Ogumi, D. A. J. Rand, and B. Scrosati, *Encyclopedia of electrochemical power sources*. Amsterdam: Elsevier B.V., 2009.

[208] M. Abdallah and A. Y. El-Etre, "Corrosion inhibition of nickel in sulfuric acid using tween surfactants," *Port. Electrochim. Acta*, vol. 21, pp. 315–326, 2003.

[209] J. R. Galvele, R. M. Torres, and R. M. Carranza, "Passivity breakdown, its relation to pitting and sress-corrosion-cracking process," *Corr*, vol. 31, pp. 563–571, 1990.

[210] K. J. Vetter, "The electric field within the passive layer of iron," *Reports Phys. Chem.*, vol. 58, no. 4, pp. 230–237, 1954.

[211] C. S. Giggins and F. S. Pettit, "Corrosion of metals and alloys in mixed gas environments at elevated temperatures," *Oxid. Met.*, vol. 14, no. 5, pp. 363–413, 1980.

[212] Joseph R. Davis, *Corrosion: Understanding the basics*. ASM International, 2000.

[213] G. S. Frankel, T. Li, and J. R. Scully, "Localized corrosion : Passive film breakdown vs pit growth stability," *J. Electrochem. Soc.*, vol. 164, no. 4, pp. 180–181, 2017.

[214] D. E. Williams, R. C. Newman, Q. Song, and R.G. Kelly, "Passivity breakdown and pitting corrosion of binary alloys," *Lett. to Nat.*, vol. 350, pp. 216–219, 1991.

[215] C. Dong, F. Mao, S. Gao, S. Sharifi-asl, and P. Lu, "Passivity breakdown on copper: Influence of temperature," *J. Electrochem. Soc.*, vol. 163, no. 13, pp. 707–717, 2016.

[216] B. MacDougall and M. J. Graham, "Formation and breakdown of passive oxide films on nickel in halide solutions," *J. Electrochem. Soc.*, vol. 132, no. 11, pp. 2553–2557, 1984.

[217] N. F. Jackson, A. Clark, T. Plessey, and C. Limited, "The tunnel etching of aluminium," *Electrocompon. Sci. Technol.*, vol. 2, pp. 33–44, 1975.

[218] P. M. Natishan and W. E. O'Grady, "Chloride ion interactions with oxide-covered aluminum leading to pitting corrosion: A review," *J. Electrochem. Soc.*, vol. 161, no. 9, pp. 421–432, 2014.

[219] D. P. Whittle and J. Stringer, "Improvements in high temperature oxidation resistance by additions of reactive elements or oxide dispersions," *Philos. Transcations R. Soc. London A*, vol. 295, pp. 309–329, 1980.

[220] D. K. Das, "Progress in Materials Science Microstructure and high temperature oxidation behavior of Pt - modified aluminide bond coats on Ni - base superalloys," *Prog. Mater. Sci.*, vol. 58, no. 2, pp. 151–182, 2013.

[221] H. J. Grabke and D. B. Meadowcroft, "European federation of corrosion publications a working party report on guidelines for methods of testing and research in high temperature corrosion," London, 1995.

[222] D. C. Murray, N. L. Richards, and W. F. Caley, "On improving the oxidation resistance of a Ni-based superalloy produced by powder metallurgy.," *Can. Metall. Q.*, vol. 52, pp. 439–448, 2013.

[223] B. G. Cade, W. F. Caley, and N. L. Richards, "Comparison of oxidation performance of two nickel base

superalloys for turbine applications," *Can. Metall. Q.*, vol. 53, no. 4, pp. 460–468, 2014.

[224] S. S. Ltd., "A collection of free downloadable papers on the development and application of JMatPro," *https://www.sentesoftware.co.uk/biblio.html.*, 2005.

[225] O. A. Ojo, N. L. Richards, and M. C. Chaturvedi, "On incipient melting during high temperature heat treatment of cast Inconel 738 superalloy," *J. Mater. Sci.*, vol. 39, no. 24, pp. 7401–7404, 2004.

[226] J. Safari and S. Nategh, "On the heat treatment of Rene-80 nickel-base superalloy," *J. Mater. Process. Technol.*, vol. 176, no. 1–3, pp. 240–250, 2006.

[227] J. Wang, M. Chen, S. Zhu, and F. Wang, "Ta effect on oxidation of a nickel-based single-crystal superalloy and its sputtered nanocrystalline coating at 900–1100°C," *Appl. Surf. Sci.*, vol. 345, pp. 194–203, 2015.

[228] J. Smialek, A. Garg, T. Gabb, and R. MacKay, "Cyclic oxidation of high Mo, reduced density superalloys," *Metals (Basel).*, vol. 5, no. 4, pp. 2165–2185, 2015.

[229] Z. Yang and P. Y. Hou, "Wrinkling behavior of alumina scales formed during isothermal oxidation of Fe – Al binary alloys," *Mater. Sci. Eng. A*, vol. 391, pp. 1–9, 2005.

[230] L. Yang, M. Chen, J. Wang, Z. Bao, S. Zhu, and F. Wang, "Diffusion of Ta and its influence on oxidation behavior of nanocrystalline coatings with different Ta, Y and Al contents," *Corros. Sci.*, vol. 126, pp. 344–355, 2017.

[231] K. Onal, G. H. Meier, and F. S. Pettit, "The effects of water vapor on the oxidation of nickel-base superalloys and coatings at temperatures from 700°C to 1100°C," in *Superalloys 2004: Proceedings of the Tenth International Symposium on Superalloys*, 2004, vol. 5, pp. 607–615.

[232] S. Geng, F. Wang, and S. Zhu, "High-temperature oxidation behavior of sputtered IN738 nanocrystalline coating," *Oxid. Met.*, vol. 57, no. 3/4, pp. 231–243, 2002.

[233] W. J. Nowak, D. Naumenko, A. Jałowicka, D. J. Young, V. Nischwitz, and W. J. Quadakkers, "Effect of alloy composition on the oxidation-induced boron depletion in cast Ni-base superalloy components," *Mater. Corros.*, vol. 68, no. 2, pp. 171–185, 2017.

[234] M. W. Brumm and H. J. Grabke, "The oxidation behaviour of NiAl: I. Phase transformations in the alumina scale during oxidation of NiAl and NiAl-Cr alloys," *Corros. Sci.*, vol. 33, no. 11, pp. 1677–1690, 1992.

[235] I. Levin and D. Brandon, "Metastable alumina polymorphs: Crystal structures and transition sequences," *J. Am. Ceram. Soc.*, vol. 81, no. 8, pp. 1995–2012, 2005.

[236] A. Sato, Y. L. Chiu, and R. C. Reed, "Oxidation of nickel-based single-crystal superalloys for industrial gas turbine applications," *Acta Mater.*, vol. 59, no. 1, pp. 225–240, 2011.

[237] R. Swadzba, L. Swadzba, J. Wiedermann, M. Hetmanczyk, and B. Witala, "Characterization of alumina scales grown on a 2nd generation single crystal Ni superalloy during isothermal oxidation at 1050, 1100 and 1150°C," *Oxid. Met.*, vol. 82, pp. 195–208, 2014.

[238] M. P. Taylor, H. E. Evans, S. Stekovic, and M. C. Hardy, "The oxidation characteristics of the nickel-based superalloy, RR1000, at temperatures of 700 - 900˚C," *Mater. High Temp.*, vol. 29, no. 2, pp. 145–150, 2012.

[239] W. Zhao, "Steam effects on oxidation behavior of alumina-scale forming nickel-based alloys and a kinetics analysis of complex scale evolution during isothermal oxidation," Ph.D. thesis, Tsinghua University, 2012.

[240] B. A. Pint, K. L. More, I. G. Wright, and P. F. Tortorelli, "Characterization of thermally cycled alumina scales," *Mater. High Temp.*, vol. 17, no. 1, pp. 165–171, 2000.

[241] C. A. Barrett and C. E. Lowell, "Comparison of isothermal and cyclic oxidation behavior of twenty-five commercial sheet alloys at 1150°C," *Oxid. Met.*, vol. 9, no. 4, pp. 307–355, 1975.

[242] R. V McVay, P. Williams, G. H. Meier, F. S. Pettit, and J. L. Smialek, "Oxidation of low sulfur single crystal nickel-base superalloys," in *Superalloys*, 1992, pp. 807–816.

[243] B. A. Pint, K. L. More, and I. G. Wright, "The use of two reactive elements to optimize oxidation performance of alumina-forming," *Mater. High Temp.*, vol. 20, no. 3, pp. 375–386, 2003.

[244] K. Onal, G. H. Meier, and F. S. Pettit, "The effects of water vapor on the oxidation of nickel-base superalloys and coatings at temperatures from 700°C to 1100°C," in *Superalloys 2004: Proceedings of the Tenth International Symposium on Superalloys*, 2004, vol. 5, pp. 607–615.

[245] S. Cruchley, H. E. Evans, M. P. Taylor, M. C. Hardy, and S. Stekovic, "Chromia layer growth on a Ni-based superalloy: Sub-parabolic kinetics and the role of titanium," *Corros. Sci.*, vol. 75, pp. 58–66, 2013.

[246] A. Mashreghi, "Determining the volume thermal expansion coefficient of TiO_2 nanoparticle by molecular dynamics simulation," *Comput. Mater. Sci.*, vol. 62, pp. 60–64, 2012.

[247] A. M. Dymshits, P. I. Dorogokupets, I. S. Sharygin, K. D. Litasov, A. Shatskiy, S. V. Rashchenko, E. Ohtani, A. Suzuki, and Y. Higo, "Thermoelastic properties of chromium oxide Cr_2O_3 (eskolaite) at high pressures and temperatures," *Phys. Chem. Miner.*, vol. 43, no. 6, pp. 447–458, 2016.

[248] K. R. Peters, D. P. Whittle, and J. Stringer, "Oxidation and hot corrosion of nickel-based alloys containing molybdenum," *Corros. Sci.*, vol. 16, no. 11, 1976.

[249] P. Berthod, C. Vébert, L. Aranda, R. Podor, and C. Rapin, "Study of carbide transformations during high-temperature oxidation of nickel-base superalloys," *Oxid. Met.*, vol. 63, no. 1–2, pp. 57–72, 2005.

[250] P. Kontis, D. M. Collins, A. J. Wilkinson, R. C. Reed, D. Raabe, and B. Gault, "Microstructural degradation of polycrystalline superalloys from oxidized carbides and implications on crack initiation," *Scr. Mater.*, vol. 147, pp. 59–63, 2018.

[251] B. J. Foss, M. C. Hardy, D. J. Child, D. S. McPhail, and B. A. Shollock, "Oxidation of a commercial nickel-based superalloy under static loading," *JOM.*, vol. 66, no. 12, pp. 2516–2524, 2014.

[252] V. Špillar and D. Dolejš, "Calculation of time-dependent nucleation and growth rates from quantitativetextural data: Inversion of crystal size distribution," *J. Petrol.*, vol. 54, no. 5, pp. 913–931, 2013.

[253] J. S. Langer, "Kinetics of phase separation in binary fluids : Nucleation near the critical point," *Physica A*, vol. 118, no. 1–3, p. 282, 1983.

[254] Y. Chen, E. M. Francis, M. Preuss, and S. J. Haigh, "On the diffusion mechanisms of fine-scale γ′ in an advanced Ni-based superalloy," *MATEC Web Conf.*, vol. 14, p. 09002, 2014.

[255] F. Masoumi, D. Shahriari, M. Jahazi, J. Cormier, and A. Devaux, "Kinetics and mechanisms of γ′ reprecipitation in a Ni-based superalloy," *Sci. Rep.*, vol. 6, pp. 1–16, 2016.

[256] M. Epler, "Structures by precipitation from solid solution," *ASM Handb.*, vol. 9, pp. 134–139, 2004.

[257] H. Numakura, T. Ikeda, M. Koiwa, and A. Almazouzi, "Self-diffusion mechanism in Ni-based $L1_2$ type intermetallic compounds," *Philos. Mag. A*, vol. 77, no. 4, pp. 887–909, 1998.

[258] Y. Q. Chen, T. J. A. Slater, E. A. Lewis, E. M. Francis, M. G. Burke, M. Preuss, and S. J. Haigh, "Measurement of size-dependent composition variations for gamma prime (γ′) precipitates in an advanced nickel-based superalloy," *Ultramicroscopy*, vol. 144, pp. 1–8, 2014.

[259] A. Encinas-Oropesa, G. L. Drew, M. C. Hardy, A. J. Leggett, J. R. Nicholls, and N. J. Simms, "Effects of oxidation and hot corrosion in a nickel disc alloy," in *Superalloys: 11th International Symposium on Superalloys*, 2008, pp. 609–618.

[260] J. H. Chen, P. M. Rogers, and J. A. Little, "Isothermal and cyclic oxidation of chromia forming nickel-based superalloys," *Mater. Sci. Forum*, vol. 251–254, pp. 57–64, 1997.

[261] F. Maak, "For the evaluation of measurements of the layer thicknesses of binary alloys with internal oxidation with simultaneous external oxidation," *Z. Met.*, vol. 52, p. 545, 1961.

[262] F. N. Rhines, W. A. Johnson, and W. A. Anderson, "Rates of high-temperature oxidation of dilute copper

alloys," *Trans. Metall. Soc. AIME*, vol. 147, p. 205, 1942.

[263] J. L. Meijering and M. J. Druyvesteyn, "Hardening of metals by internal oxidation," *Philips Res. Reports*, vol. 2, pp. 81–102, 1947.

[264] H. Hindam and D. P. Whittle, "High-temperature internal oxidation behavior of dilute nickel-aluminum alloys," *J. Mater. Sci.*, vol. 18, no. 5, pp. 1389–1404, 1983.

[265] J. Litz, A. Rahmel, M. Schorr, and J. Weiss, "Scale formation on the Ni-base superalloys IN 939 and IN 738 LC," *Oxid. Met.*, vol. 32, no. 3–4, pp. 167–184, 1989.

[266] M. A. Dayananda, "An analysis of concentration profiles for fluxes, diffusion depths, and zero-flux planes in multicomponent diffusion," *Metall. Trans. A*, vol. 14, no. 9, pp. 1851–1858, 1983.

[267] M. Watanabe, Z. Horita, T. Sano, and M. Nemoto, "Electron micrsoscopy study of Ni/Ni_3Al diffusion couple interface-II. Diffusivity measurement," *Acta Mater.*, vol. 42, no. 10, pp. 3389–3396, 1994.

[268] C. Cserhati, A. Paul, A. A. Kodentsov, M. J. H. van Dal, and F. J. J. van Loo, "Intrinsic diffusion in Ni_3Al system," *Intermetallics*, vol. 11, pp. 291–297, 2003.

[269] T. Ikeda, H. Numakura, M. Koiwa, W. Sprengel, and H. Nakajima, "Single-phase interdiffusion in Ni_3Al," *Acta Mater.*, vol. 46, no. 15, pp. 5369–5376, 1998.

[270] C. Sun, E. Martínez, J. A. Aguiar, A. Caro, J. A. Valdez, K. Baldwin, Y. Xu, B. P. Uberuaga, O. Anderoglu, and S. A. Maloy, "Thermally induced interdiffusion and precipitation in a Ni/Ni_3Al system," *Mater. Res. Lett.*, vol. 3, no. 3, pp. 169–175, 2015.

[271] D. Hamm, K. Ogle, C. O. Olsson, S. Weber, and D. Landolt, "Passivation of Fe-Cr alloys studied with ICP-AES and EQCM," *Corros. Sci.*, vol. 44, no. 7, pp. 1443–1456, 2002.

[272] I. E. Castañeda, J. G. Gonzalez-Rodriguez, J. Colin, and M. A. Neri-Flores, "Electrochemical behavior of Ni-Al-Fe alloys in simulated human body solution," *J. Solid State Electrochem.*, vol. 14, no. 7, pp. 1145–1152, 2010.

Journal Publications

1. Mallikarjuna, H. T., N. L., Richards, and W. F., Caley; Isothermal oxidation comparison of three nickel-base superalloys, *Journal of Materials Engineering and Performance, 26(5), 2014-2023, 2017.*
2. Mallikarjuna, H. T., W. F., Caley and N. L., Richards; High-temperature oxidation kinetics and oxide scale microstructure of nickel-base superalloy IN738LC at 900ºC, *Journal of Materials Engineering and Performance, 26(10), 4838-4846, 2017.*
3. Mallikarjuna, H. T., W. F., Caley and N. L., Richards; Effect of alloying elements and microstructure on cyclic oxidation performance of three Ni-based superalloys at 900˚C in static air, *Materialia, 4, 487-499, 2018.*
4. Mallikarjuna, H. T., N. L. Richards and W. F. Caley; The dependence of oxidation resistance on gamma prime intermetallic size for superalloy IN738LC, *Corrosion Science, 147, 394-405, 2019.*
5. Mallikarjuna, H. T., W. F. Caley and N. L. Richards; The effect of cooling rate on the γ' composition, morphology and corrosion behaviour of IN738LC, *Corrosion Science, 149, 37-44, 2019.*

Conference Presentations

1. Cyclic oxidation performance of three Ni-based superalloys at 900˚C, *Material Science and Technology, October-2018, Columbus, OH, USA.*
2. Cyclic oxidation of three Ni-based superalloys and life prediction using COSP-model, *Manitoba Institute of Materials Conference, May-2018, Winnipeg, MB.*

3. Comparison of isothermal and cyclic oxidation performance of IN738LC at 900°C, *Canadian Material Science Conference (CMSC), June-2017, Ottawa, ON.*
4. Isothermal oxidation of three-nickel based superalloys, *Canadian Material Science Conference (CMSC), June-2016, Hamilton, ON.*